TiO2-based photocatalytic coatings for improving indoor air quality

Giampiccolo, Andrea

Award date:
2017

Awarding institution:
University of Bath

TiO_2-based photocatalytic coatings for improving indoor air quality

Andrea Giampiccolo

A thesis submitted for the degree of Doctor of Philosophy

University of Bath

Department of Architecture and Civil Engineering

December 2017

TiO_2-based photocatalytic coatings for improving indoor air quality

Andrea Giampiccolo

A dissertation submitted to the University of Bath in accordance with the requirements of the award of the Degree of Doctor of Philosophy in the Department of Architecture and Civil Engineering

Authors' Declaration

I declare that the work in this dissertation was carried out in accordance with the requirements of the University's Regulations and Code of Practice for Research Degree Programmes and that it has not been submitted for any other academic award. Except where indicated by specific reference in the text, the work is the candidate's own work, work done in collaboration with, or with the assistance of, others, is indicated as such. Any views expressed in the dissertation are those for the author.

SIGNED:  DATE: 28/09/2017

Acknowledgements

I would like to thank my supervisors, Dr Richard J. Ball and Dr Martin P. Ansell for their support during these past years, I learned so much during our meetings and (many) meals together; thanks to their suggestions I improved my work (and poor written English) in every published work and of course, this thesis. I absorbed so much knowledge from them during this 3 (and 3/4) years.

I am also very delighted that I had the chance to collaborate with fantastic people from whom I learned and with whom I enjoyed working, Dr Manuel Nunõ, Dr[2] Gianluca Pesce, Dr David M. Tobaldi, Dr. Loredana Saccone and my favourite couple Dr. Carlita Silva and (Future Dr) Cristiano Figueiredo. Thank you very much for the help and friendship!

This thesis would not have been possible without the help of Dr John Mitchels, Dr Philip Fletcher and Ursula Potter from the Microscopy and Analysis Suite, where I learned so many things; and the amazing staff members of the Department of Architecture and Civil Engineering and Billy Murdoch, School of Mechanical and Systems Engineering, Newcastle University for the amazing He-beam images.

Thanks to my office colleagues/friends in 2 East 4.9 and 4ES 5.2, both offices for the shared meals, celebrations, interesting discussions and new experiences. I also would like to thank Dr Yolanda De Miguel at Tecnalia Bilbao, Dr Florian Mayer at Fraunhofer IBP near Munich and all the members of ECO-SEE project for their expertise and ideas. I want to express my gratitude to my best friends Rosario Crisci, Andrea Tummino and Giovanni Puglisi, all the friends from Complesso 10, Catania, Baia del Gambero and around the globe for not letting the distance undermine our friendship and be there for me at any time of the day for anything.

A special mention to my fiancé and perfect companion Alice Grimaudo, thanks to your huge support in all this long way. We are so good together that all the things that will ever happen to us will be sorted out with love (and willpower)! To conclude, I want to dedicate this thesis to my parents Maria Rita and Marcello and my wonderful brothers Luca and Gabriele. If I have been able to finish this thesis and carried on without stopping, it is entirely thanks to you. I will never be able to express in word how much I love you for loving me as I am, full of defect and stubbornness, despite sometimes we clash!

Grazie di cuore a tutti

Abstract

The photocatalytic properties of titanium dioxide have been widely studied since the discovery in 1972 of water photolysis by TiO_2 electrodes. Rutile and anatase are the most studied of the different TiO_2 polymorphs due to their chemo-physical properties. When irradiated with ultraviolet light, TiO_2 is able to absorb photons, creating on the surface an electron and a positive "hole". This electron-hole pair then reacts with water and oxygen, generating chemical radicals. These are very unstable and reactive species which can neutralise pollutants. In the introduction pollutants and their influence in the air quality are described as well as the state of art of TiO_2, photochemistry; semiconductor doping, chemo-physical principles, and TiO_2 coatings. Various protocols to test photoactivity of both powders and coatings are discussed studying both gas phase and liquid phase reactions looking at UV and visible light irradiation.

The sol-gel synthesis of pure and tungsten- and cobalt-doped TiO_2, as well as graphene/TiO_2 hybrids, was explored modifying the conditions and parameters to optimise the photocatalytic activation of TiO_2 in the visible light range.

A comprehensive study of manufactured and commercially available TiO_2 powders and coatings was performed to identify the differences between photocatalytic properties, using electron microscopy, Raman and UV-vis diffusive spectroscopy and X-ray diffraction. An important question that was answered in this thesis is whether the physical properties of nanoparticles or their electronic properties are critical for their photocatalytic behaviour. Results for doped powders of different particle size and surface area showed how the positioning of their electronic band gap with the wavelength of the visible light source was fundamental for an effective photocatalytic process for the application wanted

In the application of TiO_2 for the built environment, lime and MDF were considered as substrates for coatings. Lime-based coatings were prepared mixing commercial K7000 TiO_2 with the plaster and photoactivity of the coatings was evaluated looking at formaldehyde degradation. MDF based coating were produced using both produced sol-gel pure, doped TiO_2 and tested by observing degradation of Ink Intelligent inks under both UV and visible light confirming the photoactivity.

Throughout this work sol-gel was employed for the production of pure and doped TiO2 nanoparticles with the anatase crystalline phase. Photocatalytic tests on the synthesised particles under UV light shows comparable performances with commercial particles.

Synthesised particles and coatings shows promising performances, higher than commercially available particles when irradiated with visible light confirming a possible application in indoor environment.

Dissemination of the research work

Conferences

- Giampiccolo, A., Ball, R.J., Ansell, M.P. and Maskell, D., 2014. Synthesis of Co-doped TiO_2 nanostructures for novel photocatalytic coatings. In: ENERGY FORUM on Advanced Building Skins, 2014-10-28 - 2014-10-29, Forum Bressanone, Via Roma 9 in Bressanone.
- Giampiccolo, A., Ball, R., Ansell, M Photocatalytic Co doped TiO_2 coatings for lime and wood substrates In European Congress and Exhibition on Advanced Materials and Processes EUROMAT 2015 Mazurkas – Congress and Conference Bureau Wojska Polskiego 27 01-515, Warsaw, Poland
- A. Giampiccolo, Doped TiO_2 nanostructured photocatalytic coating for MDF and lime-based substrates, BRE Trust Research Conference 2017

Publications in international journals

- Giampiccolo A., Ansell M. P., Tobaldi D. M., and Ball R. J., Synthesis of Co–TiO_2 nanostructured photocatalytic coatings for MDF substrates, Green Materials 2016 4:4, 140-149

Accepted paper subjected to final review

- Giampiccolo, J. A. Ibáñez Gómez, Y. R. de Miguel, S. Mair, D. Maskell, A. M. Casado, C. F. da Silva, D. M. Tobaldi, F. Mayer , M. P. Ansell, J. A. Labrincha, R. J. Ball, TiO_2-based photocatalytic lime plaster for indoor air quality improvement using visible light in Journal of Physics and Chemistry of Solids

Paper in submission:

- Giampiccolo A., Tobaldi D. M., Kurchania R., Ansell M. P., Ball R. J.; Sol-gel W/TiO_2 with improved photocatalytic activity under visible and solar irradiation in **Indian Journal of Physics**
- Giampiccolo A., Tobaldi D. M., Kurchania R., Ansell M. P., Ball R. J.; Photocatalytic activity and gas sensing of sol sel Graphene/TiO_2 nanoparticles in **Sensors and Actuators B**

Acronyms and abbreviations

Abbreviation	Full name
K7000	Anatase KRONOClean 7000
P25	Anatase Aeroxide P25
DRS	Diffuse reflectance spectroscopy
EDX	Energy dispersive X-ray
FESEM	Field emission scanning electron microscope
A	Absorbance
BET	Brunauer–Emmett–Teller theory
IAQ	Indoor air quality
LED	Light emitted diode
MB	Methylene blue
LDF	Low-density fibreboard
IPA	Isopropyl alcohol
MDF	Medium density fibreboard
MUF	Melamine urea formaldehyde
SEM	Scanning electron microscope
SBS	Sick Building Syndrome
TEM	Transmission electron microscope
UV	Ultra violet
λ	Wavelength
QPA	semi-quantitative phase analysis
XRD	X-ray diffraction
WPPM	whole powder pattern modelling

Molecular formula	Full name
$Ca(OH)_2$	Calcium hydroxide
$CaCO_3$	Calcium carbonate
HNO_3	Nitric acid
HCOOH	Formic acid
C	Carbon
CO	Carbon monoxide
Co	Cobalt
CO_2	Carbon dioxide
CFCs	Chlorofluorocarbons
e^-	Electron
CH_3CH_2OH	Ethanol
h^+	Hole
H_2	Hydrogen
$^{\bullet}OH$	Hydroxyl radicals
CH_3OH	Methanol
N	Nitrogen
NO_2	Nitrogen dioxide
NO	Nitrogen monoxides
NO_x	Nitrogen oxide
O_2	Molecular oxygen
$^1O_2$	Singlet state molecular oxygen
H^+	Proton
NaOH	Sodium hydroxide
SO_2	Sulphur dioxide
H_2SO_3	Sulphurous acid

H_2SO_4	Sulphuric acid
$O_2^{\bullet-}$	Superoxide anion
Ti	Titanium
TiO_2	Titanium dioxide
$TiCl_4$	Titanium chloride
PU	Polyurethane
VOCs	Volatile organic compounds
W	Tungsten
H_2O	Water

Abbreviation	**Unit**
°C	Celsius degree
cm^3	Cubic centimetre
cm^{-1}	Wavenumber
eV	Electronvolt
h	Hour
l	Litre
ml	Millilitre
m	Metre
mm	Millimetre
µm	Micrometre
nm	Nanometre
min	Minute
s	Second

Contents

List of Figures

List of Tables

1 Introduction

In the past few decades, there has been increasing alarm over the effect of indoor air quality on health. In general, the indoor environment when filled with chemicals generates various symptoms and illness.

The development of new material and a more detailed study of existing ones is a fundamental step for the creation of new solutions. Titanium dioxide is one of these materials well known since the seventies with auspicious potential.

When this material is irradiated with the ultraviolet light source, due to the structure and properties it starts a series of reactions that are known to reduce or oxidize chemical compounds to reduce their concentration.

The aim of this PhD is to explore modification and application of titanium dioxide pure and doped to reduce indoor pollution. The idea is to cover all the surface of an indoor environment with a coating that can reduce photocatalytically the inorganic and organic pollutants using visible light instead of ultraviolet.

The beginning of this research was to use the sol-gel method to synthesise pure and doped TiO_2 nanoparticles. The process of doping will ensure that titanium dioxide reacts efficiently with visible light. Various substrates were used to increase the surface area or the reactivity of the titanium dioxide.

Coatings were formulated and applied to wood and lime based substrate to be used in the indoor environment. They were developed using both commercially available and synthesised nanoparticles.

This PhD research has focused on the study of sol-gel TiO_2 and TiO_2 coatings for the purpose of creating healthier buildings. This is a key objective of the European FP7 project ECO-SEE, led by the University of Bath, which aims to develop new eco-materials and components. The consortium worked towards the creation and use of natural eco-materials for healthier indoor environments through hygrothermal (heat and moisture) regulation and the removal of airborne pollutants through both passive capture and photocatalysis

2 Review of the literature

This chapter describes the literature relevant to this research. Important aspects of Indoor Air Quality (IAQ) and the term Sick Building Syndrome (SBS) will be introduced. Physical and chemical properties of titanium dioxide (TiO_2) semiconductor materials relevant for the treatment of pollution are outlined. Mechanistic aspects of the photocatalytic processes responsible for decomposition of pollutants are given before expanding the process to surface interactions on photocatalytic coatings.

2.1 Indoor Air Quality (IAQ) and Sick building syndrome

An air pollutant is a particulate or chemical substance (inorganic or organic) from a natural or anthropogenic source that is harmful to living organisms and the built environment [1, 2]. The main constituents of air pollutants widely acknowledged are microbes, heavy metals, oxides of nitrogen (NO_x), sulphur dioxide (SO_2), carbon monoxide (CO), carbon dioxide (CO_2) chlorofluorocarbons (CFCs), particulates and volatile organic compounds (VOCs).

The quality of the air inside homes, offices, schools and hospitals influences the health and well-being of occupants considering the significant amount of time spent indoors [2] (WHO guidelines for indoor air quality) [3]. IAQ is influenced by numerous factors such as temperature, humidity ventilation and presence of particles and pollutants

The extensive use of synthetic materials in construction has resulted in the release of pollutants from many emission sources as shown in Table 2-1 [4]

Table 2-1 Major indoor pollutants and emission sources [1].

Pollutant	**Major emission source**
Allergens	House dust, domestic animals, insects
Asbestos	Fire retardant materials, insulation
Carbon dioxide	Metabolic activity, combustion activities, motor vehicles in garages
Carbon monoxide	Fuel burning, boilers, stoves, gas or kerosene heaters, tobacco smoke
Formaldehyde	Particleboard, insulation, furnishings
Micro-organisms	People, animals, plants, air conditioning systems
Nitrogen dioxide	Outdoor air, fuel burning, motor vehicles in garages
VOCs	Adhesives, solvents, building materials, volatilization, combustion, paints, tobacco smoke
Ozone	Photochemical reactions
Particles	Re-suspension, tobacco smoke, combustion products
Polycyclic aromatic hydrocarbons	Fuel combustion, tobacco smoke
Pollens	Outdoor air, trees, grass, weeds, plants
Radon	Soil, building construction materials (concrete, stone)
Fungal spores	Soil, plants, internal surfaces
Sulphur dioxide	Outdoor air, fuel combustion

Poor IAQ can lead to a phenomenon called sick building syndrome (SBS) [4, 5], which consists of irritation of mucosal and skin together with general symptoms that are correlated with the time spent in a building [6, 7].

Solutions to poor indoor IAQ could include eliminating or controlling emission [8, 9] of building materials [10-12], increasing ventilation, and air cleaning solutions by physical or chemical reaction. Applying photocatalytic coatings based on a semiconductor that can reduce the concentration of harmful chemicals [13-15] and used as self-cleaning surfaces in both outdoors and indoors [16, 17].

2.2 Band theory for semiconductors

Electrical conductivity is the conduction of electrical charge carriers such as electrons or ions through the structure of a material [18]. All materials can be subdivided into ranges of electrical conductivity. The insulators (ceramic and polymers) have the lowest values of conductivity, conductors (metals and metal alloys) have the highest values and semiconductors (crystalline or amorphous) including titanium dioxide possess values in between as shown in Figure 2-1.

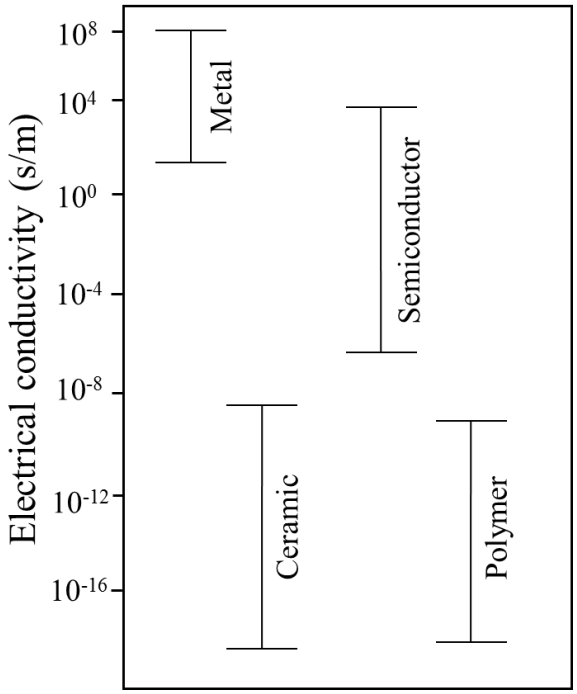

Figure 2-1 Bar chart of electrical conductivity in Siemens/metre for metal, ceramic, semiconductors and polymers.

Molecular orbital theory predicts the structure of a through the combination of the atomic orbitals of the constituent elements as shown in Figure 2-2.

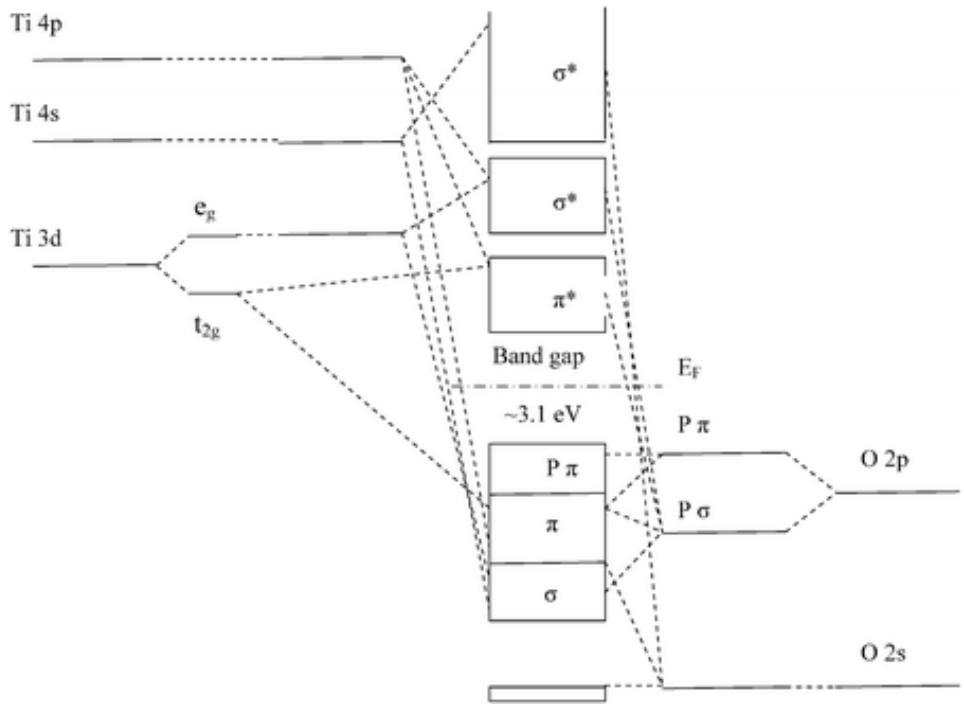

Figure 2-2 Diagram showing the combinations of the atomic orbitals of titanium and oxygen [19].

Molecular orbital theory predicts the structure of a lattice through the combination of the atomic orbitals of the constituent elements. In the case of TiO_2, because titanium and oxygen atoms have different orbital shapes, the structure will be octahedral for anatase and rutile crystal structures. The appropriate model to explain the electrical properties of a metal is the free electron model, but it fails for semiconductors and insulators so for these materials a different approach is needed. The band theory is used to describe the electronic structure. Using this theory the conductivity behaviour of all materials can be defined [18, 20].

A crystalline material has atoms arranged in an ordered way and, the distance between atoms is sufficient for the electric field generated by one atom to influence the atomic orbitals of the adjacent atoms. This phenomenon perturbs the normal behaviour of the electrons in the lattice. This influence transforms the set of energy levels in the band due to the atomic overlaps of atomic orbitals with similar energies. There are energy levels that are prohibited to electronic bands which create a gap between the bands. This interval

of inaccessible energy levels is called a band gap and is determined by material properties such as number of free electrons, bond length and bond strength.

The valence band is occupied by the valence electrons. These electrons are held around the nucleus and are responsible for chemical bonds but do not contribute to the electrical conductivity.

The conduction band is the combination of atomic orbitals in which the attraction between electrons and nuclei is weak. This level is constituted by the outer orbitals of the atoms and is filled with electrons that are shared with the rest of atoms constituting the solid.

At 0 K three type of band structure can be identified as shown in Figure 2-3:

- Overlapped conduction and valence band.
- Partially filled band where the highest occupied level is called Fermi level
- Bands of energy separated by a band gap

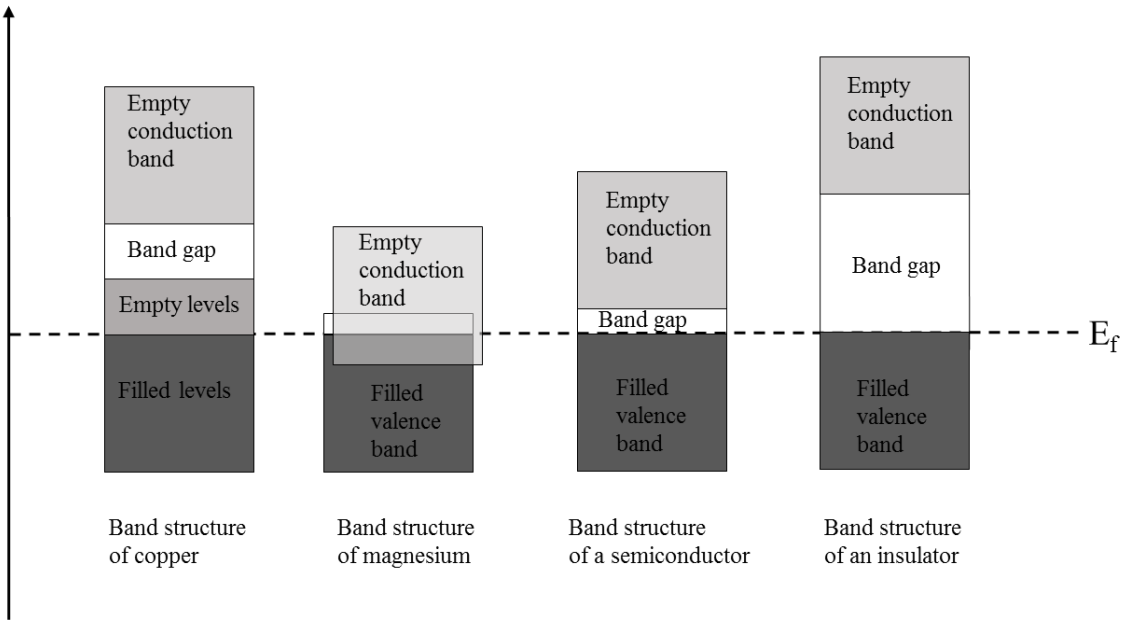

Figure 2-3 Band structures in various materials at 0K [21].

When a material gains energy from an external source (absorption of photons, heat, electricity) the atoms enter into an excited state and, some of their electrons may absorb a part of this external energy. This can cause the promotion of an electron from the valence band to the conduction band.

The band gap is the main indicator of the difference in electrical properties between metal, semiconductor and insulator. The band gap value for an insulator is higher than 5 eV [18].

This is large enough to forbid electrons from being promoted by excitation from the full band to the empty one.

In a semiconductor, the band gap is between 1 and 4 eV. The promotion of an electron depends strongly on the source of excitation. The electron can exceed the gap if the energy absorbed is higher than the band gap. In metals such as magnesium, the overlap of the bands gives the electrons the capacity of moving freely in the solid. Other metals such as copper, have a band that is partially filled and therefore able to accommodate other electrons in the valence band.

2.3 Semiconductor characteristics

The unique characteristics of the semiconductor materials involve them in a wide range of technological application. Some semiconductors change their properties such as thermal and electrical conductivity in the presence of external input such as heat or light. Transistors solar cells and light emitting diode (LED) are all based on semiconductor technology. The most common semiconductors are pure crystals but amorphous semiconductors have also been developed.

Semiconductors can be subdivided into two types

- Intrinsic semiconductors which are pure semiconductors
- Extrinsic semiconductors which are semiconductors with impurities added to the lattice

The properties of a semiconductor can be tuned by introducing a different element into the structure, which is called “doping”. A number of impurities required to modify the properties are usually between 10^{-2} and 10^{-6} percent (atomic ratio). Depending on the type of dopant added to the system the extrinsic semiconductor can be divided into two categories depending on whether the dopant modifies the number of electrons or holes in the system. N and P type semiconductors are described below.

- **N-type semiconductor**: Is a material that contains impurities that add electrons to the system. For example, if silicon (tetravalent) is doped with phosphorous (pentavalent), it will gain an extra electron for each phosphorous atom. In addition to the different charge, the change in dimensions will create a distortion in the crystal structure.

- **P-type semiconductor**: Is a material that contains impurities that add extra holes to the system. For example, if silicon (tetravalent) is doped with boron (trivalent), an electron from the silicon will fill the vacancy in the boron creating a hole.

2.4 Titanium dioxide

Titanium dioxide (TiO_2) is the most common oxide of Ti^{+4}, it occurs in nature in three crystallographic phases: anatase, rutile and brookite. At high pressure, there are various polymorphs: TiO_2 (II) with the alpha-PbO_2 structure, TiO_2 (B), TiO_2 (H), baddeleyite, fluorite and pyrite phases. The most common minerals fond in nature that contain titanium are rutile (TiO_2), ilmenite ($FeTiO_3$) and titanite ($CaTiSiO_5$) [20].

Figure 2-4 shows the Ti-O phase diagram as a function of composition and temperature whereas Figure 2-5 shows the TiO_2 phase equilibria between rutile and anatase. Figure 2-6 shows the UV-visible reflectance spectra and band gap for the three main pure TiO_2 polymorphs.

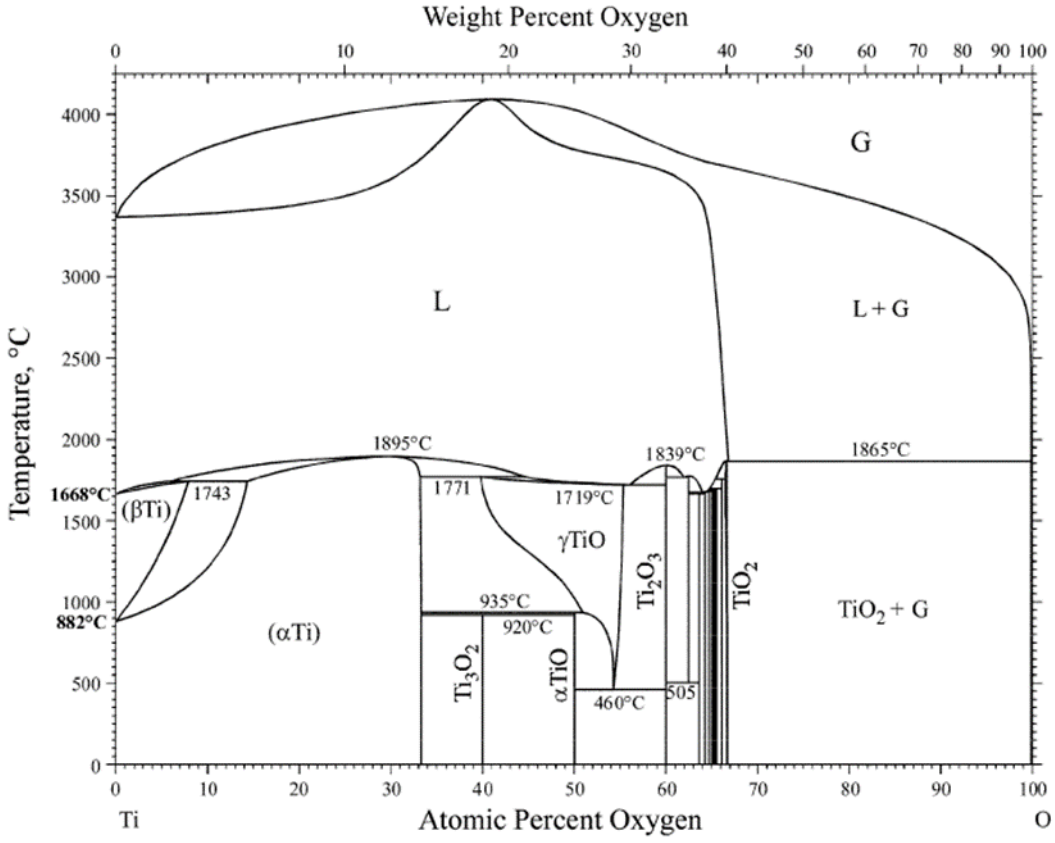

Figure 2-4 Titanium-Oxygen phase diagram in function of composition and temperature. It shows the most predominant oxides in specific ration Ti/O and temperature [22].

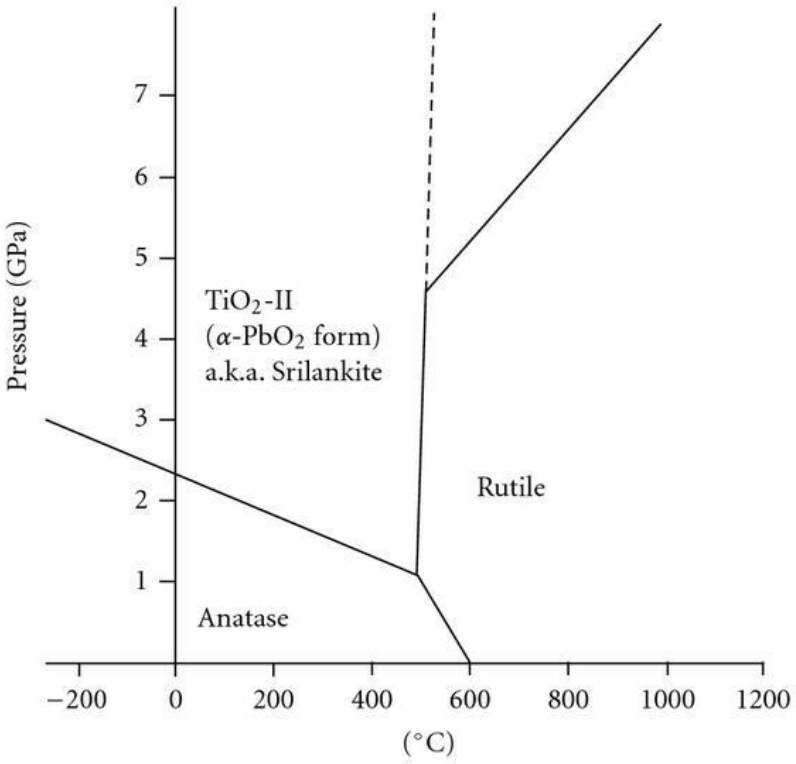

Figure 2-5 Phase equilibria in function of pressure and temperature between TiO_2 in form of anatase, rutile and TiO_2 (Srilankite).

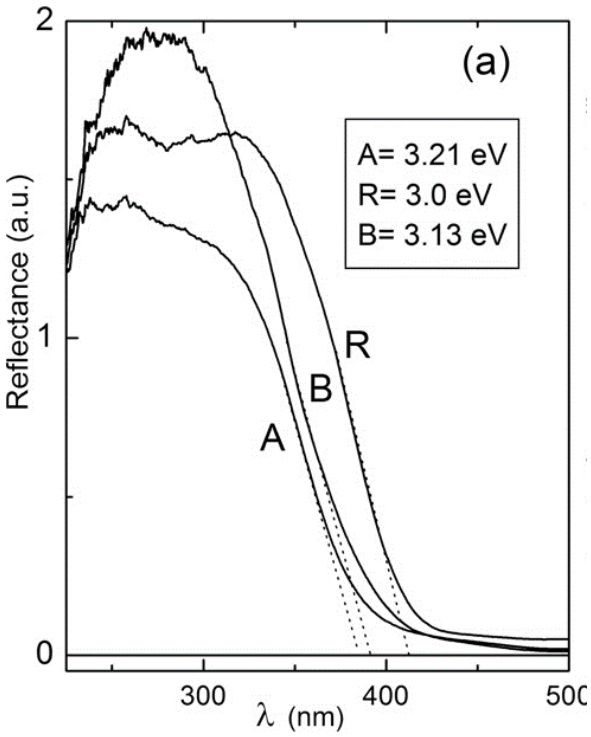

Figure 2-6 UV-Visible reflectance spectra for the pure phase of the three polymorphs of TiO_2. A= Anatase, R= Rutile, B= Brookite [23].

Rutile

Rutile is the most common polymorph of TiO_2 being also the most thermodynamically stable [24] and has the lowest molecular volume of the three polymorphs considered. Rutile is used as a white pigment in various products including paints, polymers, paper and whitening agents and it is the most common form of TiO_2 used worldwide [23, 25]. The unit cell of rutile is a tetragonal cell, the base unit is octahedral with the octahedra sharing vertices as shown in Figure 2-7 and the space group is $P4_2/mnm$ as shown in Table 2-2. The band gap in rutile is 3.0 eV [23], [26].

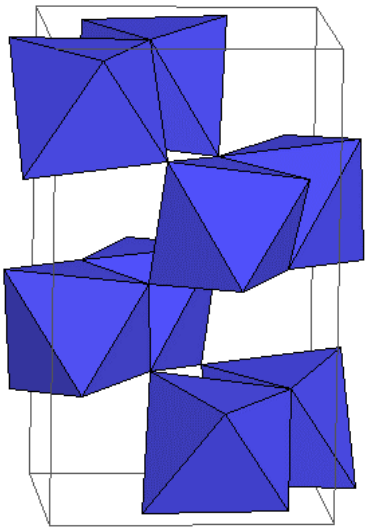

a)

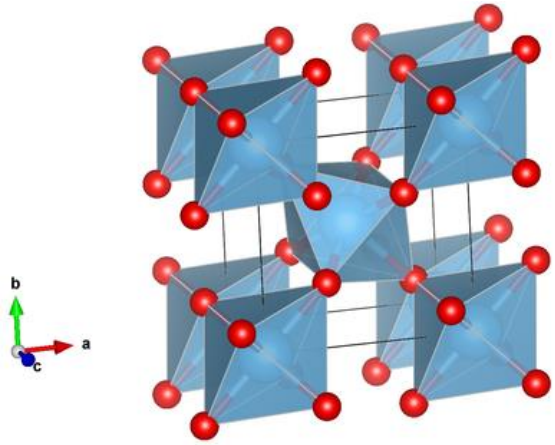

b)

Figure 2-7 a) Rutile crystal structure [27], Rutile structure showing the atomic structure [28].

Anatase

Anatase is one of the three natural polymorphs of TiO_2. Anatase is a metastable phase at room temperature and it transforms irreversibly to rutile at temperatures higher than 500/600 °C [12][29]. The structure is tetragonal, the base units are octahedrons that share an edge, as shown in Figure 2-8 and Table 2-2, making anatase the natural polymorph with the lowest density. The band gap is the highest among the three natural crystalline structures equal to 3.21 eV [10][26] although other values have been reported 3.4 eV. [30] and 3.1 eV [31]. This difference could result from a change in semiconductor carriers[32] or the particles size [33]. The position of its band gap (related to the Standard hydrogen electrode) influences the photochemistry of the crystal [34].

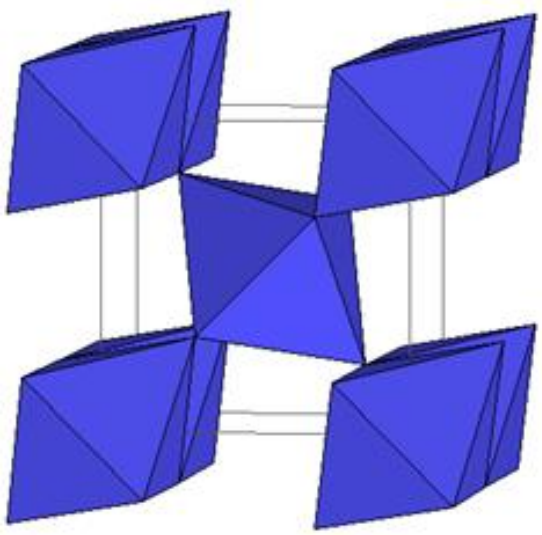

Figure 2-8 Anatase crystal structure [23].

Brookite

Brookite is another polymorph of TiO2 that can be found in nature. Compared with the other two structures, its crystal system is orthorhombic instead of tetragonal and the space group is Pbca [35] as shown in Figure 2-9 reported in Table 2-2. This crystal structure has an optical band gap of 3.13 eV [10[26, 36]. Brookite shows photocatalytic properties as well as Anatase [37].

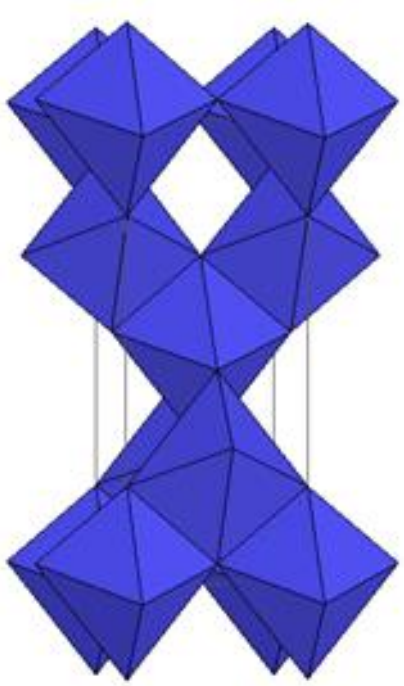

Figure 2-9 Brookite crystal structure [23].

Table 2-2 Mineral structure and properties of Rutile, Anatase, Brookite and TiO_2 (II).

	Rutile	**Anatase**	**Brookite**	**TiO_2(II)**
Crystal system	Tetragonal	Tetragonal	Orthorhombic	Orthorhombic
Space group	P42/mnm	I41/amd	Pcba	Pbcn
Unit cell parameters (Å)	a=4.594 c=2.959	a=3.785 c=9.514	a=9.184 b=5.447 c=5.145	a=4.59 b=5.44 c=4.94

2.5 Manufacture of TiO_2

TiO_2 is extracted from either ilmenite or rutile following either the sulphate process or chloride route depending on the chemicals and process used.

The sulphate process employs simpler technology but has higher production costs and the acid treatment facility is more expensive to build than a chloride plant.TiO_2 produced via the chloride route is purer, but anatase can only be produced by the sulphate route.

TiO_2 nanoparticles can be also produced in various chemical synthesis routes that include chemical vapour deposition (CVD), inverse micelle synthesis and sol-gel.

CVD synthesis is carried out oxidising titanium halides (titanium chloride for example) in a tubular reactor at a high temperature producing spherical particles with small nanometric particles size [38-40]. The variables that can be modified and include the heat flux, the amount of halides used and the temperature and duration of the process.

Degussa P25 is produced via flame vaporization. The process is based on the use of high purity liquid titanium chloride as a raw material that is vaporized and mixed with air and hydrogen. This gas is then directed onto a high temperature flame (1000-2400°C) producing nanoparticles with an average particle size of 25 nm [41].

A chemical process to synthesise TiO_2 in solution is the hydrated reverse micelles. This method is based on the formation of a microemulsion that produces uniform nanoparticles. Variables that influence the dimensions and amount of nanoparticles relate to the actual dimensions of the micelles to the kind of surfactant used that can influence nucleation grow and agglomeration of the particles as reported in the literature [42-44].

Sol-gel is one of the most commonly used methods due to several advantages such as low processing temperature, high homogeneity, simplicity, stability and versatility of processing.

The method is based on the production of a sol by hydrolysis of a (titanium in this case) metalorganic precursor dissolved in alcohol, adding water drop by drop to the solution under reflux at an elevated temperature. The sol produced is then dried and calcined to obtain nanoparticles with the desired crystal structure.

The variables to be tuned in sol-gel synthesis include the titanium precursor and the solvent type which both influence the ratio between crystalline phases Reflux and calcination temperatures also play a critical role in determining the ratio of crystalline phases having higher temperatures will promote the formation of rutile form over the anatase phase.[45].

2.6 Photo induced processes

Within the whole electromagnetic spectrum ranging from short wavelengths (less than the diameter of an atom) to long radio waves (km), visible light is just a minor portion as presented in Figure 2-10. Semiconductors require a certain range of wavelengths within the electromagnetic spectrum to be excited thus changing their conductivity. Photocatalysis is defined as a process where a reaction is promoted by the absorption of light by the catalyst.

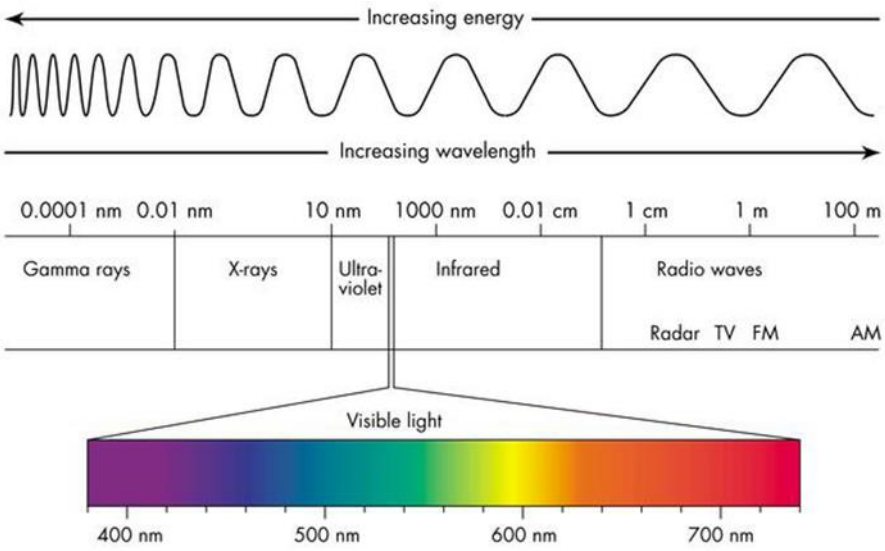

Figure 2-10 Electromagnetic spectrum [46].

If a semiconductor is irradiated by photons more energetic than the band gap electrons can be photoexcited. These reactions are called photochemical and involve the promotion of an electron as shown in Figure 2-11

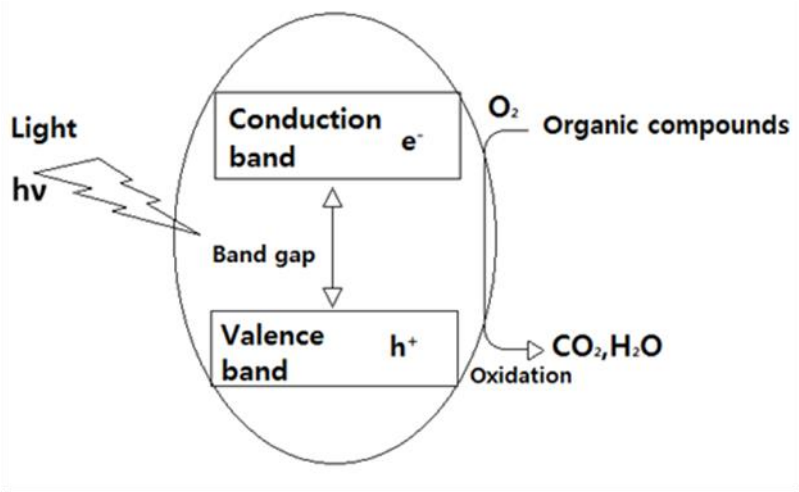

Figure 2-11 Electron-hole couple formation process scheme.

Acceptors like oxygen and organic compounds are able to accept an electron (reduction), whereas donors, the semiconductor, in this case, can provide one of their electrons (oxidation) in the process shown in Figure 2-11.

This promotion process causes charge separation, positive where electrons are removed (valence band) and negative where the electrons are received (conduction band). Photocatalytic materials have the ability to promote these redox reactions as a function of the position of their bands.

A general redox reaction is described in equation (2-1)

$$Ox_1 + Red_2 + h\nu \rightarrow Red_1 + Ox_2 \quad \text{when } h\nu > \text{Energy Gap} \qquad (2\text{-}1)$$

One of the first publications on photo-electrochemistry involving TiO_2 was published by Akira Fujishima and Kenichi Honda in 1972 [47]. In this article, the photo-electrochemistry of rutile in water splitting was described with reactions (2-2) to (2-5) as shown in Figure 2-12.

$$H_2O + h\nu \rightarrow + \tfrac{1}{2}\, O_2 + H_2 \qquad \text{General process} \qquad (2\text{-}2)$$

$$TiO_2 + h\nu \rightarrow 2e^- + 2h^+ + TiO_2 \qquad \text{(process of excitation of } TiO_2 \text{ by light)} \qquad (2\text{-}3)$$

$$2h^+ + H_2O \rightarrow \tfrac{1}{2}\, O_2 + H_2 \qquad \text{(Semi-reaction at the } TiO_2 \text{ electrode)} \qquad (2\text{-}4)$$

$$2e^- + 2H^+ \rightarrow H_2 \qquad \text{(Semi-reaction at the platinum electrode)} \qquad (2\text{-}5)$$

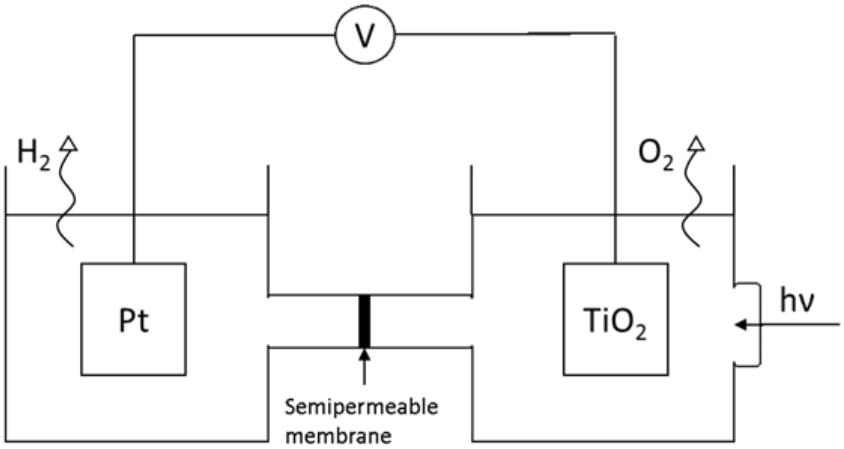

Figure 2-12 Electrochemical cell with TiO_2 and platinum electrodes used by Fujishima and Kenichi for water splitting [47].

2.7 Photocatalytic behaviour of titanium dioxide

Since the first publication on the photocatalytic properties of TiO_2 [47], the number of publications and research have increased exponentially. They are mainly focused methods for air treatment [48, 49], water treatment [50-52], self-cleaning surfaces [14, 15, 53] or for a new super hydrophilic surface [54].

The understanding of how titanium dioxide generates oxidizing species is fundamental to an actual application of this semiconductor. This mechanism was reported by Akira Fujishima [34, 47], Kenichi Honda [55] and Koichi Iwata [47]. Photocatalysis by TiO_2 starts with the absorption of UV photons that promote electrons from the conduction band to the valence band creating a separation of the charges [47, 56, 57]. The separation produces an electron (e_{cb}^-) and hole (h_{vb}^+) couple that migrates to the surface of the material and react with molecules such as H_2O and O_2 participating to the photocatalytic process.

This process leads to the formation of free radicals which are described by equation (2-6) to (2-12) [34, 56] and have a characteristic short half-life [58-61]. Radicals are described as chemical species (molecules or atoms) with at least one unpaired electron. Due to their instability and high reactivity, they have a short half-life and the ability to react with a wide range of different compounds with time scales in the order of femtoseconds. The oxidizing species are usually h^+, hydroxyl radicals, superoxide ($O_2^{\cdot -}$) and singlet state molecular oxygen [59-62].

$$TiO_2 \xrightarrow{h\nu} e^- + h^+ \quad (2\text{-}6)$$

$$h^+ + H_2O \rightarrow {}^{\bullet}OH + H^+ \quad (2\text{-}7)$$

$$e^- + H^+ \rightarrow {}^{\bullet}H \quad (2\text{-}8)$$

$$H^+ + O_2^{\bullet -} \rightarrow HO_2^{\bullet} \quad (2\text{-}9)$$

$$e^- + h^+ \rightarrow \text{heat or } h\nu \quad (2\text{-}10)$$

$$e^- + O_2 \rightarrow O_2^{\bullet -} \quad (2\text{-}11)$$

$$h^+ + O_2^{\bullet -} \rightarrow {}^1O_2 \quad (2\text{-}12)$$

The reaction between free radicals and chemicals results in the reduction-oxidation (redox) processes that are associated with the neutralization and removal or harmful molecules. Titanium dioxide can be found in three different metastable polymorphs where anatase, with a gap of 3.2 eV [22, 26], is widely accepted as the most efficient structure for separation of the charges on the surface under irradiation with UV light [63].

Water is a necessary component for the formation of hydroxyl radicals, but these species alone are not responsible for oxidizing some substances such as organic molecules (e.g. benzene, formaldehyde, alcohols and dienes). The initiator of these reactions has to be a hole [34]. Fujishima et al. concluded that electrons are trapped by molecular oxygen changing the equilibrium between charge generation and charge recombination [64, 65].

The process described before generate a photo excited hole/electron couple and can explain some of the properties of the surface. For example, the hydrophilic property can be assigned to the formation of more OH groups on the surface by breaking Ti-O bonds. [66, 67].

2.8 Removal of atmospheric pollutants

The reactions that form the free radicals described previously make photocatalysts perfect materials for removing air pollutants. Reactive species generated are able to react with organic and inorganic pollutants in order to transform them into harmless species.

Two different oxides of nitrogen; nitrogen monoxide (NO) and nitrogen dioxide (NO_2), are produced naturally or by human activities (combustions by-products).

Photocatalytic processes involved in the oxidation of these compounds to form nitric acid on the surface of the catalyst are presented in equations (2-13) to (2-15) [68].

$$NO + {}^{\bullet}OH \rightarrow HNO_2 \quad (2\text{-}13)$$

$$HNO_2 + {}^{\bullet}OH \rightarrow NO_2 + H_2O \quad (2\text{-}14)$$

$$NO_2 + {}^{\bullet}OH \rightarrow HNO_3 \quad (2\text{-}15)$$

A successful study by Yu et al [69], oxidizes nitrogen oxides to nitric acid following the proposed mechanism. Sulphur dioxide, as well as nitrogen dioxide, could be reduced in the presence of carbon monoxide [70, 71] following reactions (2-16 and (2-17.

$$SO_2 + 2CO \rightarrow S + 2CO_2 \quad (2\text{-}16)$$

$$2NO + 2CO \rightarrow N_2 + 2CO_2 \quad (2\text{-}17)$$

The degradation of SO_2 causes the formation of sulphur deposited on the photocatalytic surface.

CH_4 and CH_3OH are the main products of the photoreduction of CO_2 in the presence of TiO_2 and H_2O and absence of O_2 as previously reported in both the gas-solid phase and the liquid-solid phase [72-74].

A CO_2 photoreduction mechanism has been proposed to consume electrons and hydrogen radicals as shown in equations (2-18 to (2-23

$$CO_2 + e^- \rightarrow {}^{\bullet}CO_2^- \quad (2\text{-}18)$$

$${}^{\bullet}CO_2^- + 8{}^{\bullet}H + h^+ \rightarrow CH_4 + 2H_2O \quad (2\text{-}19)$$

$${}^{\bullet}CO_2^- + 6{}^{\bullet}H + h^+ \rightarrow CH_3OH + 2H_2O \quad (2\text{-}20)$$

$${}^{\bullet}CO_2^- + 2{}^{\bullet}H + h^+ \rightarrow HCOOH \quad (2\text{-}21)$$

$${}^{\bullet}CO_2^- + 4{}^{\bullet}H + h^+ \rightarrow HCHO + H_2O \quad (2\text{-}22)$$

$${}^{\bullet}CO_2^- + 12{}^{\bullet}H + 2h^+ \rightarrow C_2H_5OH + 3H_2O \quad (2\text{-}23)$$

Halmann et al. [75] reported that reoxidation of CO_2^- by hydroxyl radicals could be the reason for the reduced level of photo reduction. Anpo et al. [76, 77] proposed the reaction mechanism in Figure 2-13 involving the anchoring of CO_2 on the TiO_2 surface.

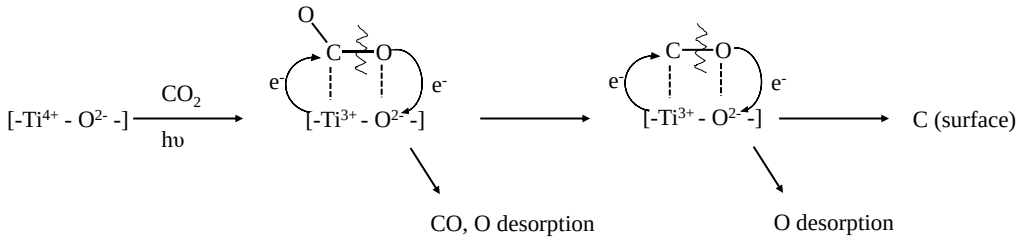

Figure 2-13 Schematic representation of the photocatalytic reduction of CO_2 [76, 77].

2.9 Study of photocatalytic reactions

The most common way to report and measure the photocatalytic activity of various materials in the form of powders or nanoparticles is to study the behaviour of these materials in the form of an aqueous suspension. ISO (International Organization for Standardization) 10678 [78] describes how to follow the decomposition rate of methylene blue, to establish the level of photocatalytic activity.

Methylene blue is an organic poly-heterocycle with a maximum peak of absorption at 670 nm (molar extinction coefficient in water, ε= 71089 $l \times mol^{-1} \times cm^{-1}$). When it is reduced, in this case by photocatalytic activity, it turns colourless in an aqueous solution (see Figure 2-14). When using methylene blue it is important to consider its molecular structure which is different to that of a pollutant. Under photo catalytic degradation caution must be exercised when correlating results obtained with methylene blue to that of an air pollutant. This can be assigned to different interface, solid/gas in the case of the pollutant and also to different bonds broken down by photocatalytic activity.

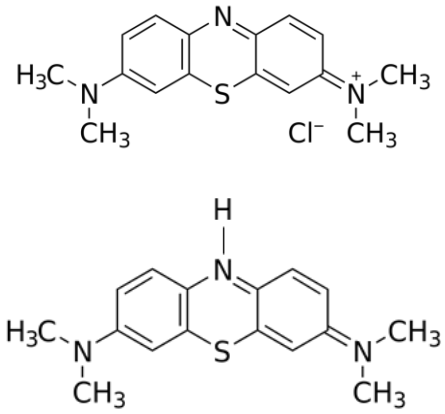

Figure 2-14 Chemical structure of methylene blue oxidised state (left) and reduced state (right).

However, when compared with gas-phase reactions, the mechanisms involved in aqueous based methods is significantly different making a comparison between liquid and gas phase reactions very difficult. There are currently another two published ISO methods related to air purification, each one being specific to one pollutant:

- Nitric oxide (NO) ISO 22197-1
- Toluene ($CH_3C_6H_5$) ISO 22197-3

These methods use the same system which consists of a reactor chamber (usually stainless steel) with a quartz glass window where a UVA light source is used to irradiate the inside of the reactor. The pollutants of interest are included in a gas mixture inside the chamber at 50 % RH and room temperature. The reactor is connected to an analyser and for NO the detection system is based on its chemiluminescent reaction with luminol [79] whereas for $CH_3C_6H_5$ the detector is a gas chromatograph coupled to a flame ionization detector [80].

2.10 Tailoring TiO_2 photocatalytic properties

Various methods which can be used to modify TiO_2 to enhance the photocatalytic properties are described in the following sections.

Modification of TiO_2 lattice

Photocatalysis in semiconductors such as TiO_2 has proved to be a very effective method for neutralizing pollutants. To exploit this property, UV photons are required, which constitute less than 5 % of the total solar spectrum. Visible light constitutes 45 % of the total solar spectrum [81]. However visible photons have insufficient energy to promote charge separation in TiO_2.

This is the main motive for the investigation of a new generation of photocatalysts designed to exploit visible radiation. The main strategy to achieve this is to move the band gap of TiO_2 towards the visible region effectively increasing the number of photons which interact with the semiconductor generating the process of charge separation. This successful strategy was achieved by modifying the physical properties of TiO_2 by the inclusion of metallic ions [82-84] or noble metals [85-87] in the lattice or the use of non-

metallic elements, such as nitrogen [83, 88], [89] or carbon [90, 91] to replace oxygen in the TiO_2 structure.

Coupling TiO_2 to other substrates

An alternative strategy to modifying the electronic transfer properties and recombination time of the charges, generated during the photocatalytic process of the system, involves coupling TiO_2 to different particles such as other semiconductors including Al_2O_3 [92-94], SiO_2 [95] [96, 97], inorganic systems such as zeolites [98-101] and organic molecules such as carbon nanotubes (CNT) [102, 103] and graphene sheets[104-107]. Some studies have proven how electron-accepting and charge-transport properties of CNT and graphene provide a way to direct and stabilize the photocatalytically generated charges. This increases the lifetime of the electron-hole couple generated on the surface and consequently, improves their photocatalytic activity.

2.11 Heterojunctions

When doping the crystalline structure of TiO_2 with noble or transition metal there is the possibility to create oxides from the doping metal. At the interface between the two materials with different band gap a heterojunction occurs. The behaviour of the heterojunction mainly depends on the alignment between the energy bands of the two oxides. Interfaces can be divided in three types: straddling gap (type I), staggered gap (type II) or broken gap (type III) as seen in Figure 2-15

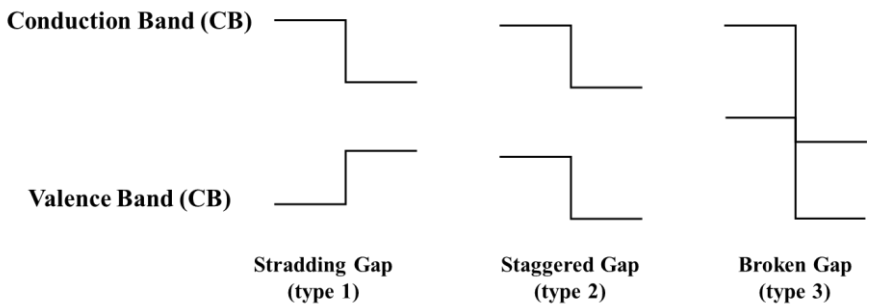

Figure 2-15 Bands disposition in heterojunctions type I, II and III

Various methods are used to predict the band alignment; a common anion rule was proposed relating valence band of anionic states, supposing that materials with the same anions should have very small valence band offsets. This theory was modified by Tersoff who proposed a gap state model based on metal-semiconductor junctions; in this case conduction band offset is given by the difference in Schottky barrier height. This model agrees well with systems where both materials are closely lattice matched [108, 109]

A heterojunction for the couples cobalt oxide/TiO_2 and tungsten oxide/ TiO_2 is presented in Figure 2-16. The system cobalt oxide/ TiO_2 is reported to improve photocatalytic properties and promote longer charge recombination in visible light [110]. The system tungsten oxide/ TiO_2 has been studied as a multi-layered thin film for improved visible-light absorption capability as well as charge transfer efficiency [111] improving the system's photocatalytic performance.

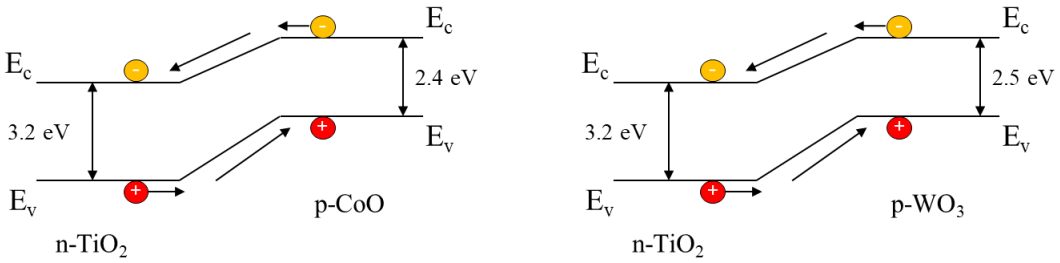

Figure 2-16 Electron–hole movement after hetero-junction formation in CoO/TiO_2 and WO_3/TiO_2

2.12 Photocatalytic film

The application and development of photocatalysts for paint and coatings for air quality improvement in both indoor and outdoor areas is a flourishing field of research [112-115]. Coatings are used for various applications, from solar cell to pigments to screening agents against UV light [116]. Several methods can be used to prepare a coating and between them, sol-gel processing [117-119]and chemical vapour deposition have been extensively studied [120-122].

The aim of this research is to use existing film preparation techniques to apply TiO_2 based coatings on building materials.TiO_2-based coatings on Lime and MDF based substrates were produced using a simple system of application of photo catalytically active layer.

Photocatalytic coatings on Lime based substrates

Lime has been used by the construction industry for thousands of years. Recently many researchers have been developing and modifying its properties through the incorporation of TiO_2 into mortars and plasters. However, this research mainly exploited PC activity using the UV portion of the solar irradiation and NO_x as a model pollutant [123, 124]. For instance, Park *et al*. investigated NO_x removal using plaster mixed with TiO_2 with a UVA lamp light source [125]; Vieira *et al*. incorporated a commercial nano-TiO_2 (Evonik-previously Degussa, P25) into plasters, and evaluated their PC activity against NO_x, using an artificial solar light irradiation [126]. Also, Lucas and co-workers, tested the PC activity, against NO_x degradation, of plasters containing P25 TiO_2 using a lamp simulating the solar radiation containing a UVA component [127]. Other research groups, used organic dyes *i.e.* methylene blue or rhodamine B to monitor the PC activity of TiO_2 based plasters using UV-lamps as the light source [127, 128].

Despite the promising applications of TiO_2 coatings, photocatalytic coatings have not been applied widely as a novel coating for buildings beyond laboratory scale. Available products based on this technology are commercialized, photocatalytic paints (KNOxOUT© by Boysen and ECO-EX© by TOTO ltd., Ecogreen plus) or pigments for paints (KRONOCLEAN series). TiO_2 is usually employed for its hydrophilic properties, an excellent advantage for self-cleaning and anti-fogging windows. Hydrophilic properties originate from the decomposition (photocatalytic oxidation) and adsorption on the surface of the photocatalyst under UV conditions [66, 129].

Because the concentration of pollutants is higher at street level[116], research involving coating cementitious materials with titanium dioxide has been undertaken with encouraging results [130] [131] [132]. The main problem associated with TiO_2 based coatings is poisoning of the active sites; Ameen and Raupp found that exposure for as little as 100 min was sufficient to decrease the photoactivity due to deactivation [133]. Reactants poison the photocatalyst and in the case of NO_2, nitric acid is formed and accumulates on the coating surfaces inhibiting the reaction with subsequent NO_x. In the presence of liquid water, these deposits of nitric acid are easily removed [116].

Examples of buildings currently using this technology can be found worldwide. The most representatives for their impact and iconic style are reported in Figure 2-17 and Figure 2-18:

- "Chiesa di Dio Padre Misericordioso" in Rome; where the architect, Richard Meier used white cement based on TiO_2 (developed for Italcementi S.p.A.) to maintain its white colour despite the massive traffic related pollution.

Figure 2-17 - Chiesa di Dio Padre Misericordioso.

Toyota's Tsutsumi plant in Aichi (), where they manufacture hybrid cars, was painted with Hydrotect colour coat ECO-EX.

Figure 2-18 Toyota's Tsutsumi plant (Image property of TOTO Ltd.).

Photocatalytic coatings on MDF based substrates

MDF is used worldwide for many applications including building and furniture construction. It has a number of advantages when compared to natural wood which is mainly associated with its homogeneity and absence of defects such as knots and irregularities. Properties can be tuned by varying the type of resin, the constitution of the fibres and manufacturing parameters for the fibreboard [134-136]. For certain applications, this manufacturing flexibility can be a distinct advantage, but the formaldehyde based resins (e.g. melamine urea formaldehyde, MUF) used to bind the wood fibres are responsible for the particularly high emission of aldehydes [137] and other VOCs. These are particularly detrimental to human health and use of photo catalysts may provide a means to reduce their concentrations.

To use a photocatalytic material effectively it is necessary to immobilise it on the surface of a substrate. This can present a challenge as the coating procedure must maintain the photocatalytic activity of the particles and not lead to any adverse consequences, such as degradation of the surface. A review of recent developments in nanomaterials for application to timber was provided by Ansell [138] including discussion of the work of Allen et al. who investigated the photochemical stability of TiO_2 containing water-based acrylic paints in comparison with standard paints to prevent the yellowing of wood with exposure to UV radiation. The study found increasing the proportion of rutile nano-TiO_2

particles between 1 and 5% by weight correlated with improved colour stability of a wood-substrate, however, the improvement from anatase was less evident. Subsequent research also found nano TiO_2 to have effective properties as an antibacterial agent when compared with standard titanium dioxide used as a pigment [135]. Nano TiO_2 has been successfully used in wood coatings as a UV absorber to improve physicomechanical as well as thermal properties [136].

2.13 Aims and objectives

The overall aim of this thesis was to synthesise and characterize TiO_2, W-TiO_2, Co-TiO_2 and Graphene/TiO_2 hybrids as well as testing them for photocatalytic activity looking at the decomposition of liquid and gaseous pollutants. Synthesised and commercially available TiO_2 were included and tested in coatings in order to improve indoor air quality in the building environment.

Therefore, the particular objectives of this research were:

- To synthesise TiO_2, W-TiO_2, Co-TiO_2 and Graphene/TiO_2 hybrids using the sol-gel method
- Characterize surface morphology, elemental composition and crystalline phases in all the samples
- To study photocatalytic reactions, such as dye degradation in aqueous phase as well as the activity of photocatalysts in the gas phase
- To produce and characterize coatings based on sol-gel either produced in this research or commercially available TiO_2 applied to building materials such as MDF and lime mortar
- To test the photocatalytic performance of the coatings produced either in the aqueous phase or the gas phase

3 Analytical techniques

This chapter describes the analytical techniques used during the programme of research and the theoretical approaches employed to analyse data.

3.1 X-ray diffraction

X-ray diffraction is a powerful technique regularly used to characterize crystallographic structures of raw materials and coatings. Compared to some other analytical techniques the sample preparation is generally more straightforward and less problematic.

A monochromatic beam of X-rays is focused on the surface of the sample, interacting with the electrons of the three-dimensional crystal structure. The diffracted beam is composed of many interferences, both constructive and destructive, as showed in Figure 3-1 (a) and (b) respectively. Knowledge of the diffracted X-ray beam intensity and its corresponding incident angle with the atomic planes, allows deduction of many types of information about the crystal structure [139].

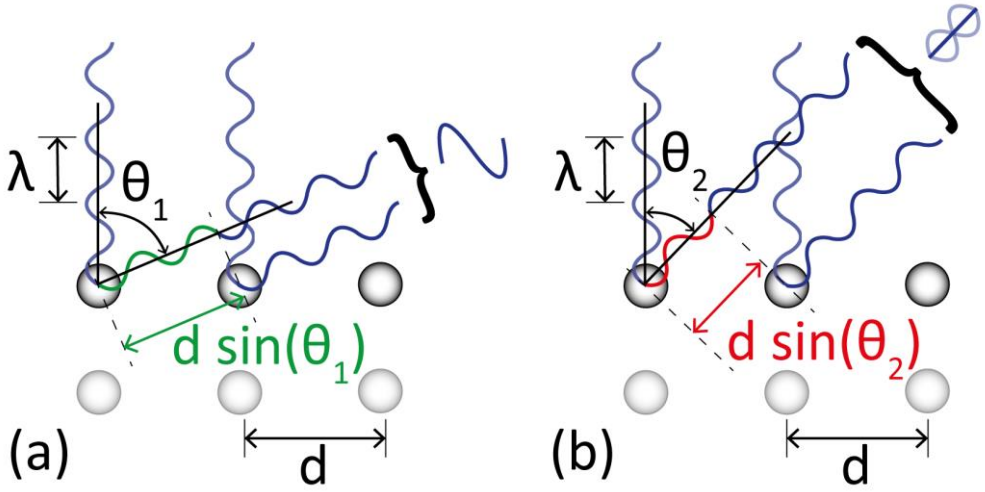

Figure 3-1 Constructive interference of reflected beams in XRD [140].

Constructive interference occurs when the phase shift of beams reflected from different planes, 2dsinθ, is an integer value, *n*, of the X-ray wavelength as expressed by Bragg's law, equation (3-1):

$$n\lambda = 2dsin\theta \qquad (3\text{-}1)$$

Where *d* is the interplanar spacing in the atomic lattice and θ is the angle formed by the scattering plane and the incident X-ray beam.

From XRD raw data, it is possible to estimate the particle size of the material. Different approaches have been studied; including the width of the line at half the maximum intensity [141] and the integral breadth [142] of the peak. Another approach is a semi-quantitative phase analysis (QPA) attained by way of the Rietveld method on the XRD data[143, 144]. Microstructural features are derivable from XRD raw data using the whole powder pattern modelling (WPPM) method [145] as implemented in the PM2K software package [145]. By means of this novel methodology, the size distribution of individual phases in nanoparticles can be accurately defined [146]. In this work, crystalline domains were assumed to be spherical, and their diameter distributed according to a log-normal curve. A typical Rietveld method spectrum for anatase and brookite is reported in Figure 3-2.

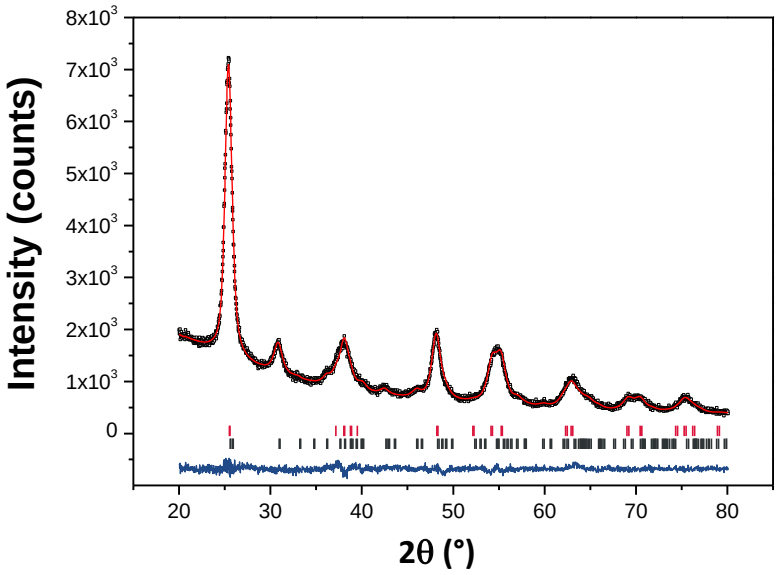

Figure 3-2 Graphic output of the Rietveld refinement of a typical synthesised TiO_2 specimen. The continuous red line represents the calculated pattern, the black open squares represent the observed pattern, and the difference curve between observed and calculated profiles is plotted below continuous blue line. The position of reflections is indicated by the small vertical bars (red: anatase; black: brookite).

XRD apparatus and conditions

XRD data were measured with a PANalytical X'Pert Pro (NL) θ/θ diffractometer, using Cu Kα radiation (45 kV and 40 mA emission current) with a step size of 0.02 °2θ and time per step of 0.2 s over a 20–80 °2θ range The instrumental broadening was measured using the NIST SRM 660b standard (LaB_6) and used to correct all the spectra. The XRD was equipped with a flat plate sample holder configuration as shown in Figure 3-3, where a smooth surface is mandatory for good acquisition of spectra.

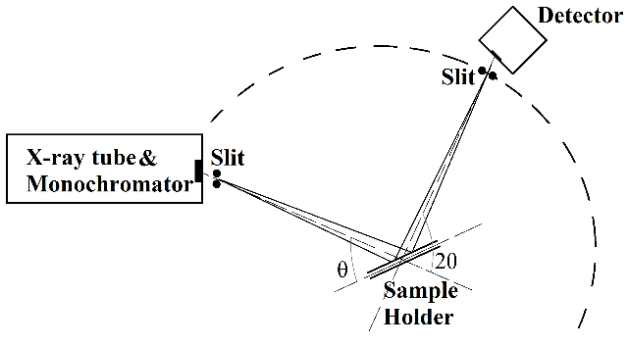

Figure 3-3 Diagram of XRD flat plate mode configuration.

3.2 Electron and ion microscopy

The following sections describe all the electron microscopy techniques employed in the research.

3.2.1 Scanning electron microscopy

The scanning electron microscope (SEM) is utilized to obtain high magnification images of a specimen by scanning the surface with an electron beam and analysing the intensity of electrons emitted. Compared to optical microscopy, the electron used in electron microscopy have a much shorter wavelength compared to visible light. This allows magnifications of up to x250000 to theoretically be achieved with a spatial resolution of 50 to 100 nm [147]. Coupling the technique with an analyser that measures the energy of X-rays emitted as a consequence of the interaction between the electron beam and the atoms in the sample (Energy-Dispersive X-Ray Spectroscopy), allows the study of the near-surface chemical composition.

The electron sources employed are usually thermionic crystals or tungsten filaments which emit electrons under vacuum by heat or high voltage. The electrons produced accelerate towards an anode containing a small aperture which produces a beam of

electrons. This electron beam is then collimated and focused onto the surface of the sample through magnetic lenses. In order to produce an image, the beam is scanned over the area of the specimen surface that is of interest in a raster pattern. The intensity of the signal from the detector is then plotted relative to a grey scale on a monitor thus constructing an image. When the electron beam interacts with the sample surface secondary electrons, backscattered electrons and Auger electrons are produced, in addition to fluorescence and X-rays as shown in Figure 3-4.

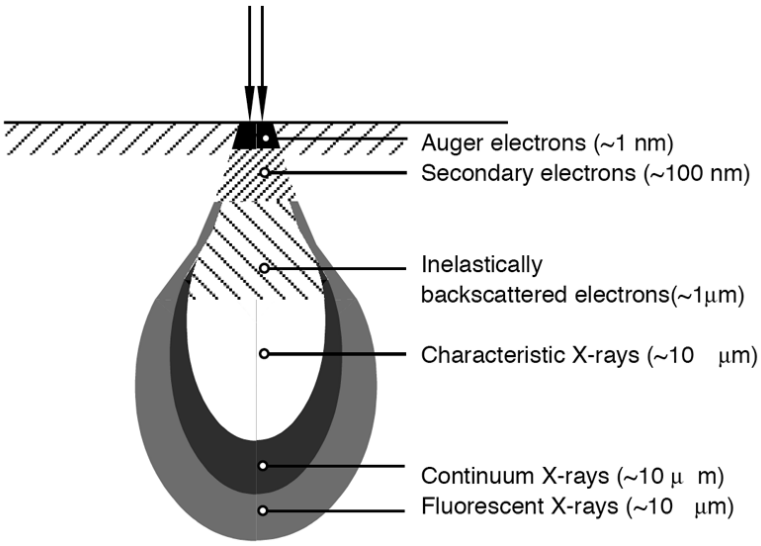

Figure 3-4 Different emissions generated by x-ray interaction with the surface.

In the field of electron microscopy, specific detectors designed to detect either backscattered or secondary electrons are commonly used. Secondary electron images reveal the morphology of the surface while compositional information where lighter areas correspond to higher relative atomic masses are produced by backscattered electrons as shown in Figure 3-5.

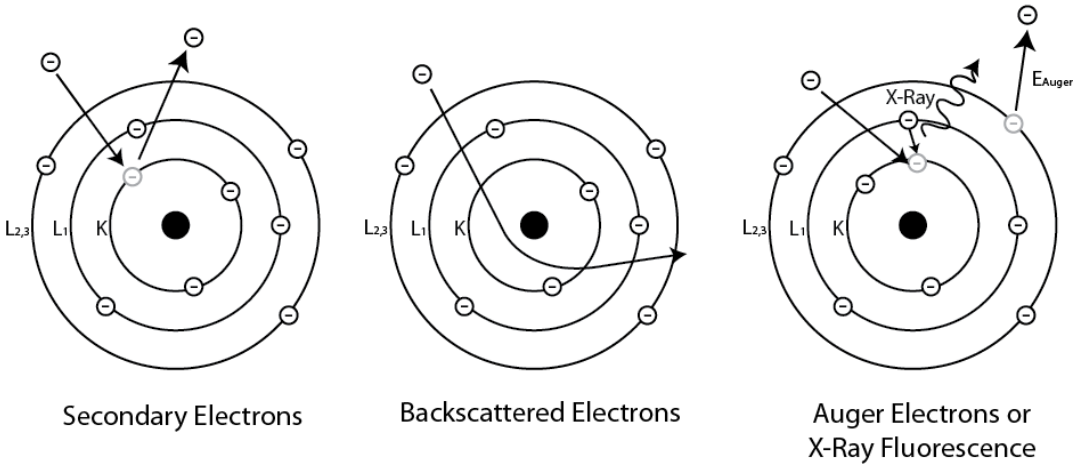

Figure 3-5 Various mode of electron emission from incident electrons [148]

- **Energy dispersive X-ray analysis**

As **Figure 3-4** Different emissions generated by x-ray interaction with the surfaceFigure 3-4 shows, once the sample is irradiated, different radiation emissions can be analysed. X-ray radiation is characteristic for each element. If X-ray energy is measured, identification and quantification of elements (EDX) can be performed at low vacuum and with an uncoated sample. The sensitivity of the technique is determined by the resolution and accuracy of the detector.

- **Specimen preparation**

When samples to be used in SEM are electrically conductive, special preparation is not required and the sample can be deposited on carbon tape on top of a holder. If the material is an insulator or a semiconductor as is the case for TiO_2, a conductive layer can be deposited over the surface to reduce charging greatly improving the image quality. A film of 10 nm of chromium was deposited using a Q150T S Turbo-Pumped Sputter Coater with a thickness control feature.

- **SEM apparatus and conditions**

The SEM apparatus used was a JEOL SEM6480LV unit equipped with a motorised stage alongside a coupled Oxford INCA X-ray analyser. The beam of electrons employed was accelerated with a typical working voltage between 5 to 15 kV. The incident electron beam should have a diameter between 20 nm and 50 nm which is controlled via a magnetic lens.

3.2.2 Field Emission SEM

The Field emission scanning electron microscope (FE-SEM) is a more refined version of SEM with the difference of the electron source, higher vacuum conditions, more complex lens system and a lower working voltage. Field emission guns consist of a sharp metal or ceramic (with a high melting point) section of the order of 100 nm thick which is held in a high electrical potential gradient, required for field emission of electrons. The magnification of an ideal sample can reach x500,000.

- **Specimen preparation**

The specimen preparation is the same as the one described for SEM in section 29.

- **FE-SEM apparatus and conditions**

The equipment used was a JEOL FESEM6301F equipped with a motorised stage, allowing the use of low accelerating voltages (from 1 to 10kV).

3.2.3 Transmission electron microscopy

Transmission electron microscopy (TEM) was used to characterise materials at high resolution, allowing magnifications up to x 1,000,000 to be achieved at high accelerating voltages. TEM forms a visual image from electrons that pass through an ultrathin sample. This technique allows the study of the crystal grains of nano-materials, allowing the determination of the particle size, and the observation of atomic lattices.

- **Specimen preparation**

Powdered samples were finely ground and dispersed in ethanol; after centrifugation, the supernatant was taken and diluted with ethanol until the colloidal suspension was quasi-transparent. A drop of this dispersion was placed on copper coated carbon grids and dried overnight under vacuum.

- **TEM apparatus and conditions**

The equipment used was a JEM-2100Plus Transmission Electron Microscope (TEM) using an acceleration voltage of 200 keV and a spot size of 1 nm.

3.2.4 Scanning helium ion microscopy

Scanning helium ion microscopy (SHIM) was used to characterize the surface of specimens obtaining sharp images with a larger depth of field when compared to standard electron microscopy due to the smaller excitation volume. Employing ions instead of electrons allows combining milling and observation of particles at sub-nanometer resolutions. The images were obtained), at the School of Mechanical and Systems Engineering, Newcastle University with a Zeiss Orion NanoFab, using He^+ ions with an accelerating voltage of 25kV and beam current of 0.3 pA with the angle varied between 0 and 54 deg.

3.3 Raman spectroscopy

Raman spectroscopy is a non-destructive technique which observes frequency modes in an excited system. Raman spectroscopy has been used in chemistry, especially in the aqueous phase, as infrared spectroscopy cannot be performed in that medium (water interferes with the spectra). Raman spectroscopy allows analysis of the chemical composition and molecular structure looking at an energetic difference of the vibrational modes, oscillating the dipole moment [149]. These oscillations provoked by the light absorption are subjected to relaxation processes by emission of light as showed in Figure 3-6

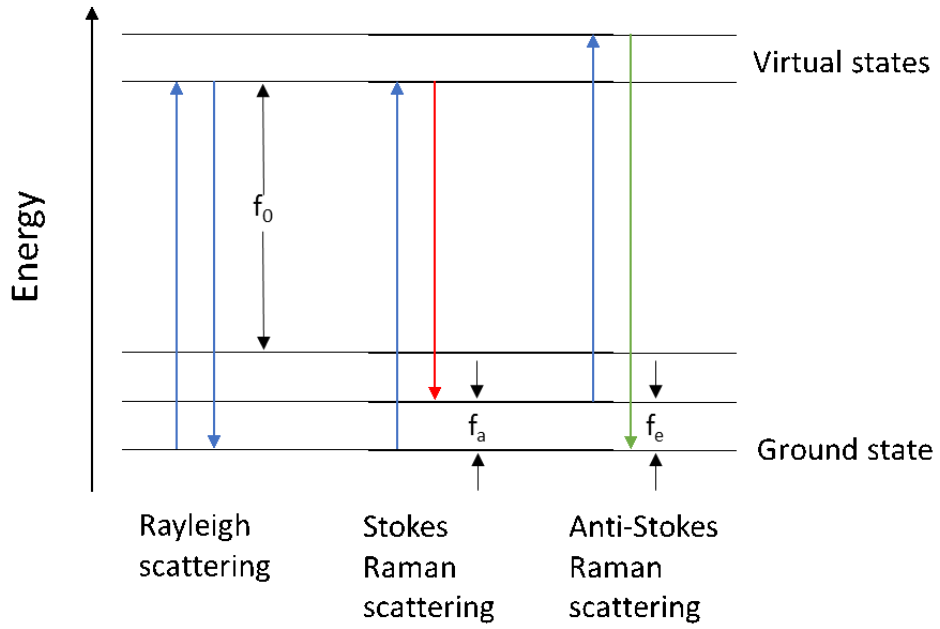

Figure 3-6 scheme of energy-level diagram showing states involved in Raman signal generation

- Elastic Rayleigh scattering is the usual process involved in Raman-inactive compounds, where the molecule absorbs the photon with frequency f_a and then emits radiation with the identical frequency f_0.
- Stokes frequency: When a photon with frequency f_0 is absorbed by a Raman-active molecule, which is the basic vibrational state, part of the energy of the photon is transferred. Therefore the scattered light has a frequency $f_0 - f_a$.
- Anti-Stokes frequency: When a photon with frequency f_0 is absorbed by a Raman-active molecule, which is the excited vibrational state, part of the energy of the photon is transferred. Therefore the scattered light has a frequency $f_0 + f_e$.

During a Raman analysis, the sample is irradiated with a laser, usually in the visible or UV, and the radiation emitted by the sample is collected by a lens and sent to a monochromatic filter and a photodetector. Since the Raman scattering is usually very weak, the main problem is to separate it from the Rayleigh scattering. In many cases, the problem is solved by cutting off the spectral range where this phenomenon is present (80-120 cm^{-1}).

- **Apparatus and conditions**

A Renishaw System 2000 spectrometer was used equipped with an inVia Raman microscope using a He-Ne laser as an excitation source operating at 785 nm and a maximum power of 20 mW. The samples were analysed by focusing the laser with objective magnification ×100 onto the sample surface corresponding to a laser spot diameter of about 10 μm. The acquisition time of 1s was used for each spectrum over the wavenumber range 100–3500cm^{-1} with a 4 cm^{-1} resolution.

The evaluation of the crystalline phases of the samples was analysed using a Renishaw inVia Raman microscope equipped with excitation sources of 532 nm and 785 nm Diode Renishaw. The analyses were performed using objective magnification 100 x and 50 x. Laser power was reduced from 1 to 5%, the acquisition time was set at 3s with a total of 10 accumulations over the wavenumber range 100–3500cm^{-1} with a 4 cm^{-1} resolution. Prior to the analysis, a monocrystalline silicon standard was used as a reference for the calibration. Renishaw WiRe 4.0 software was used to analyse the raw data.

3.4 UV-Visible diffuse reflectance spectroscopy

UV-Vis diffuse reflectance spectroscopy, along with the Kubelka-Munk function [12] (Eq. 2.5) converting the reflectance (R) into the absorption coefficient 'F(R)' were employed to determine the bandgap of the semiconductors.

$$F(R) = \frac{(1-R)^2}{2R} \qquad (3.2)$$

A Tauc plot is used to determine the optical bandgap, or Tauc gap, in semiconductors. Combining the Kubelka-Munk function with the Tauc plot (Eq. 2.6) provides the absorption energy which corresponds to the bandgap:

$$(h\upsilon F(R))^2 = A(h\upsilon - E_g) \qquad (3.3)$$

Where R is the reflectance, 'h' is Planck's constant, 'υ' is the frequency of vibration, 'E_g' the bandgap energy and 'A' is a proportionally constant.

- **Apparatus**

A Shimadzu UV 3100 (JP) spectrometer and spectra of the samples were acquired in the UV–Vis range (250–850 nm), with 0.2 nm step-size, and Spectralon® white reference material.

3.5 BET surface area analysis

This method is based on the adsorption of a non-corrosive gas (usually N_2, Ar, CO_2 or He) on a solid surface. BET theory extends the Langmuir monolayer molecular adsorption theory to a multilayer adsorption based on two hypotheses:

- Gas molecules physically adsorb on a solid in layers infinitely
- None of the adsorbed layers interact with each other

The surface area is measured by measuring the amount of gas adsorbed at a given pressure [150]. The BET equation correlates the adsorbed gas quantity 'υ', equilibrium and saturation pressure of adsorbates 'p' and p_0' respectively, and the monolayer adsorbed gas quantity 'υ_m'. 'c' is the BET constant which depends on the difference between the heat of adsorption for the first layer and the heat of liquefaction.

$$\frac{1}{\upsilon(\frac{p_0}{p}-1)} = \frac{c-1}{\upsilon_m c}\left(\frac{p}{p_0}\right) + \frac{1}{\upsilon_m c} \qquad (3.4)$$

The graphical plot of equation 2.13 is a straight line when the adsorption is isotherm. The value of the slope and the interception on the y axis can be used to calculate 'υ_m' and 'c'. The value of the specific surface area is given by:

$$S_{BET} = \frac{\upsilon_m N s}{V a} \qquad (3.5)$$

Where 'N' is Avogadro's number, 's' is the adsorption cross section of the adsorbing species, 'V' the molar volume of adsorbed gas and 'a' the mass of the sample.

- **Apparatus**

A Micromeritics Gemini 2380 Surface Area Analyser was used to measure the specific surface area of powders using N_2 as adsorbant.

3.6 Mercury intrusion porosimetry

This technique studies the intrusion of mercury at high pressure into the material to determine properties such as average pore diameter, total pore volume, as well as bulk and absolute densities. The pore size can be determined assuming that they are all cylindrical using Washburn's equation [151]

$$P_L - P_G = \frac{4\sigma \cos\theta}{D_P} \quad (3.6)$$

Where 'P_L' is the pressure of liquid, 'P_G' is the pressure of the gas, 'σ' is the surface tension of the liquid, 'θ' is the contact angle of mercury, 'D_P' is the pore diameter.

- **Apparatus**

Porosity was measured using a Micromeritics Autopore IV 9500 model with a mercury filling pressure range between 0.0036 MPa and 228 MPa with an equilibration time of 10 s. For this work representative fragments, each with a mass of approximately 2 g, were taken from the surface of each sample

4. Experimental methods

This chapter describes the preparation of TiO_2nanoparticle aggregates using a sol-gel process and also variations in the technique used to manufacture doped particles and novel compositions including secondary phases such as graphene. Application of the particles onto the surface of different substrates is also described in detail. Ultimately the chapter describes the tests employed for evaluating the photocatalytic performance of both powders and coatings.

4.1 Pure and doped TiO_2 synthesis

The following subsections describe the synthesis route employed for the manufacture of the various particles used.

4.1.1 Pure TiO_2 synthesis

Manufacture of TiO_2 through a sol-gel method is based on the hydrolysis and polymerization of a metal-organic precursor to form a colloidal suspension. In the synthesis 10 ml of Ti tetraisopropoxide (Sigma Aldrich, ≥ 98 %, MM = 284.22; d = 0,96 g/mL) was mixed with 40 ml of 2-propanol (Sigma Aldrich, ≥ 99,7 %, d = 0,785 g/mL) in a round bottom flask [152, 153]. The flask, which also acted as the reaction vessel, was positioned above a hotplate/magnetic stirrer (Figure 4-1) within a fume cupboard. The reaction vessel was placed inside a flat crystallizer dish filled with water thereby ensuring the flask was heated evenly and maintained at the reaction temperature of 80 °C. A separator funnel mounted above the round bottom flask was filled with deionized water adjusted to a pH of 2 using nitric acid. The acid provided the optimum pH for the hydrolysis reaction to occur.

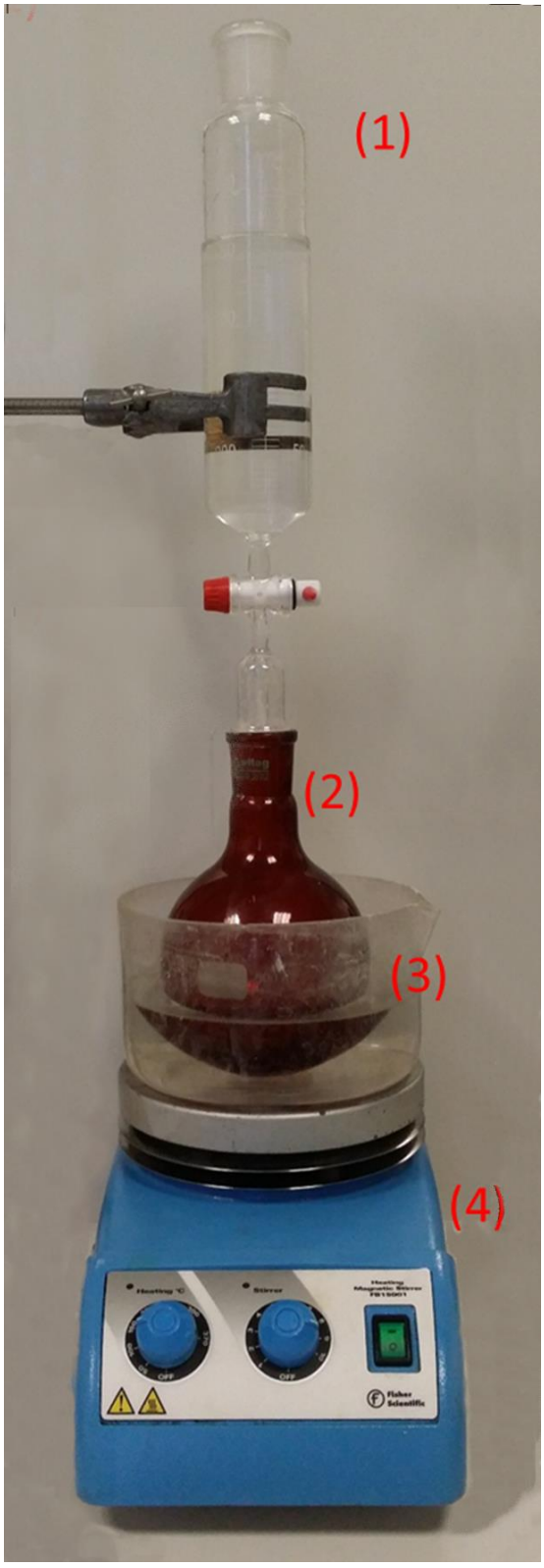

Figure 4-1 Sol -Gel reaction system, (1) Separator funnel containing 250 ml of a solution acidified water, (2) Round bottom flask containing 2-propanol and the titanium precursor, (3) Crystallizer plate with water for the temperature bath and (4) Hotplate/magnetic stirrer.

The 2-propanol and the titanium precursor were maintained at a temperature of 80°C under constant vigorous magnetic stirring for 1 hour before the acidified water was allowed to flow into the reaction vessel at a rate of 2ml/min. After continuous stirring for 6 hours, a colloidal system with a concentration of 5g/L undoped TiO_2 was obtained through the reaction described in equation (4-1)

$$Ti[OCH(CH_3)_2]_4 + 2H_2O \xrightarrow[(CH_3)_2CHOH]{HNO_3} TiO_2 + 4(CH_3)_2CHOH \qquad (4\text{-}1)$$

The excess solvent was removed immediately after completion of the reaction. The TiO_2 was initially amorphous and required annealing to form the anatase crystalline phase. Compared to either amorphous or rutile TiO_2 this phase exhibits a higher photocatalytic activity [154]. Annealing was carried out using an Elite BRF 14/10-2416 CG furnace with the material held in an alumina crucible of internal volume 20 ml. The annealing was achieved by ramping the temperature at a rate of 200°C/h followed by a dwell time of 2.5h at 450°C, prior to cooling.

4.1.2 Cobalt doped TiO_2

The protocol used to produce cobalt doped TiO_2 was a modified version of that used when manufacturing the un-doped particles. The acidified water to be added to the alcoholic solution in the vessel was substituted with a $7x10^{-4}$ M solution of $CoCl_2$ that was used to achieve a dopant concentration of 1 atomic percent in the TiO_2 lattice. $CoCl_2$ was used as a source of cobalt that is easily reachable and with a relatively low toxicity. The aqueous cobalt chloride was introduced into the reaction vessel with a flow of 2 ml/min. After continuous stirring for 6 hours a colloidal system with a concentration of 5g/L cobalt doped TiO_2 was obtained through the reaction described in equation 4.1.1. The resulting Co-doped TiO_2 structures were amorphous and required annealing to allow the formation of the anatase crystalline phase. Annealing was carried out at 450°C and 550°C for two and a half hour to compare the two structures as suggested by Regonini [155]. The furnace used was an Elite BRF 14/10-2416 CG and the material was held in an alumina crucible of internal volume 20 ml.

4.1.3 W TiO_2 synthesis

W-doped TiO_2, with various percentages of tungsten, was prepared using a modified version of synthesis route described by Tobaldi et al. [156]. Tungstic acid (Sigma-Aldrich, WH_2O_4, ≥ 98 %, MM = 249.85) was used as a source of tungsten at various concentrations. The stoichiometric quantity was dissolved in concentrated ammonia (15 ml of 25% NH_3) due to the insolubility of the acid in water or 2-propanol. The ammonia and tungstic acid solution was then added to 25 ml of water and successively to 80 ml of 2-propanol. A separator funnel was filled with the solution and then manually mixed for a sufficient time for the light opalescence to disappear. Nitric acid (HNO_3 Sigma-Aldrich, ≥ 70 %, MM = 63.01; d = 1.413 g/mL) was then added to adjust the pH to 2. This final solution was added dropwise to the Ti tetraisopropoxide in 2-propanol under continuous mechanical stirring. Following completion, the solvent was then removed and the powder was thermally treated at 450°C for 2.5 h following the procedures described previously.

4.2 Graphene/TiO_2 sample preparation

The samples with graphene were prepared following two different protocols. In the first synthesis 1g of CamGraph GR1 graphene (Cambridge Nanosystems) (10% w.t.) was added to the reaction vessel together with the titanium tetraisopropoxide and stirred at 80°C for 2 hours before initiating the reaction through the addition of acidified water. This led to the formation of a grey colloidal solution of pH 1.8 measured using an Omega PHB23 pH-meter. Following completion of the reaction, the sample was then annealed following an identical procedure to that described previously for the pure TiO_2. Following the annealing, a change in colour of the powder from grey to white was observed. Hereafter the sample is referred to as GTiO_2S.

In the second synthesis pure TiO_2 prepared following the synthesis described previously was placed into a beaker together with a mixture of 10% pure sol-gel TiO_2 40% ethanol, 40% water and 10% w.t. of CamGraph graphene (Cambridge Nanosystems). This solution was stirred at 70°C for two hours and then the solvent was removed to collect the powders. Hereafter this sample is referred to as GTiO_2M.

5. Application of coatings on building materials

Preparation protocols for producing TiO2 base coatings on lime and MDF substrates are described in this chapter

5.1 Production of coatings on MDF

MDF wood board with a paper décor finish impregnated with melamine urea formaldehyde (MUF) were used as substrates for the coating. MDF boards were provided by Kronospan (UK). Kronospan produces panels in a number of different finishes suitable for use as flooring, wall and furniture panels. An aspen oak wood-effect panel, manufacturer reference 8630, Figure 5.1, was selected for use as the substrate material due to the representative nature of the finish in comparison to the wood panel products currently on the market and appropriateness of the colour for the application of a white coating

Figure 5-1 Aspen oak wood-effect panel 8630 by Kronospan

The panels were cut, using a band saw, into square test coupons approximately 30mm by 30mm and the edges were filed down by hand to remove burrs.

Water based solutions were prepared containing 1% polyurethane (PU), 25% isopropyl alcohol (IPA) and 0.5% (0.02 g) of TiO_2 by weight. These components were weighed out using a balance with a sensitivity of +/-0.1mg. The water and IPA components were placed together in a glass beaker before the TiO_2 was added. The beakers were then placed in an ultrasonic bath for a minimum of five minutes to ensure mixing prior to the addition of polyurethane via a pipette. The beakers were then returned to the sonic bath for at least ten minutes prior to application of the coatings onto the substrate.

Prior to coating, the coupons were wiped with a dry lint-free cloth to remove any contamination. A clean natural-bristle brush was used to apply the coating submerging it into the relevant mixture with excess wiped off at the edge of the vial, before applying three brush strokes across the coupon. The brush direction was changed without re-dipping to spread the solution evenly across the coupon which deposited approximately 0.25ml of liquid on an area of 9 cm^2. The mass of applied coating was not measured, however, a coating thickness of 20 microns was estimated. As only the top layer of the mixture would contribute to photocatalytic activity the coating thickness is not expected to influence the photocatalytic activity, however, thickness could determine long term durability when in service. Achieving a consistent surface finish was of greater importance than maintaining a constant mass.

5.2 Preparation of lime coating

This section provides the details of each stage necessary for the production of photocatalytic lime substrates.

Preparation of substrates:

The substrate used was composed of 3 layers: The bottom layer consisted of an A4 size low-density fibreboard (LDF) on which the second layer of lime binder, produced by Lhoist, 'Tradical PF 80' was cast [157]. The lime binder used was suitable for application onto soft vapour permeable LDF substrate which provides protection from deformation and thermal shocks in addition to waterproofing properties. The third and the top most layer comprised of the lime render marketed by BCB of the group Lhoist as 'Tradical Décor'. This is generally applied as a face or finisher for interior purposes. In all cases, manufacturer's instructions for applications were followed.

Preparation of lime render:

The lime render was prepared by weighing 625g of mortar powder in a mixer container. 112.5 g of distilled water was weighed in a container labelled as 'A'. 25g of distilled water was weighed in a container labelled as 'B' as showed in Figure 5-2.

Figure 5-2 Lime mortar in the mixing bowl and the two beakers with water to be added.

The mortar powder was then placed in the mortar-mixing machine and the distilled water in container A was added. The mixture was rotated for 90 seconds. After 90 seconds, the mixture was allowed to rest for 5 minutes and all the mortar stuck to the mixer paddle was removed with a spatula and was then added back to the mortar mixer container. After 5 minutes, the water in container B was added and the machine was started again, rotating the mixture for a further 90 seconds as shown in Figure 5-3

Figure 5-3 Mortar and water mixed together.

Once the mixing was completed, it was taken out from the mixer and applied to the substrate as described previously.

5.3 Substrate preparation for the application of lime render

A small piece of cardboard of thickness 3mm was placed below the substrates to raise the frame of 3mm, therefore, allowing this thickness of the lime render to be accurately applied using the edge of the frame as a guide. The surface of the substrate was lightly sprayed with water to make it moist. The fresh lime mortar was then added to the surface of the substrate with a spatula to obtain a smooth and flat layer as shown in Figure 5-4.

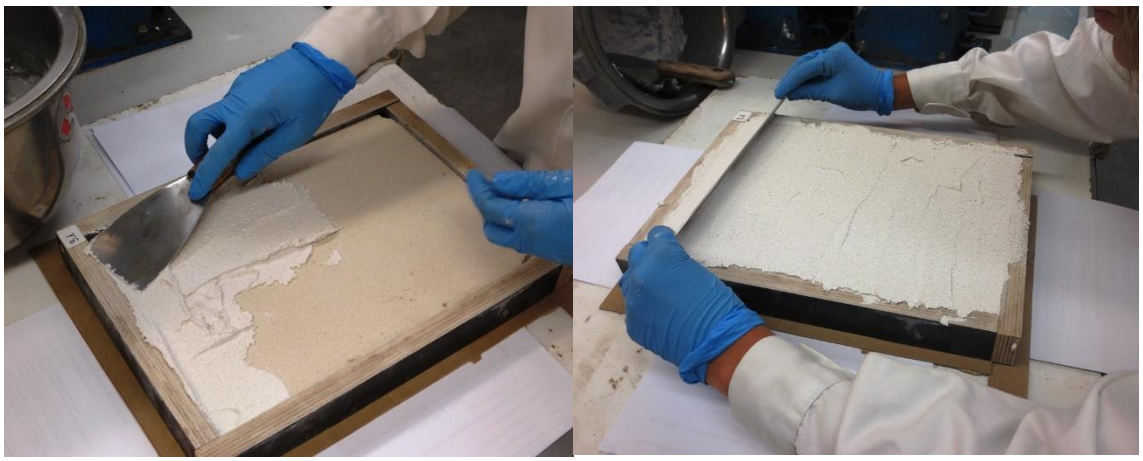

a) b)

Figure 5-4 a) application of the mixed mortar on the substrate, b) smoothing of the surface, finishing it with a metal bar.

After the application of the lime mortar, the substrate was kept in a conditioning room for 28 days at a temperature of 22°C (±2°C) and relative humidity of 53% (±3%) to set and dry. Once each A4 sized panel had cured to a sufficient strength it was cut into 6 equal parts ready for testing.

The tested materials were all based on commercially available lime plasters. The Tradical Décor lime plaster was supplied by BCB - L'hoist. Four specimens of these plasters were prepared with different contents of TiO_2 nanoparticles with respect to the dry mixture (2, 3 and 5 wt%) including a control with 0% particles added. Dimensions of the specimens were A4-size and, although the plaster thickness could range from 2 mm to 20 mm, in the case of the samples described in this manuscript, 20 mm thick specimens were employed. The titanium dioxide was KRONOClean 7000® (K7000) from KRONOS, with a BET specific Surface area >225 m^2/g, the crystallite size of around 15 nm (according to manufacturer's data), where anatase is the only crystalline phase, with amorphous phase content between 6.5-8.1 wt% [158].

The dry components were mixed (using an automatic plaster mixer) without any previous treatment. Then water was added according to the Tradical Décor technical data sheet [157]. The plasters mix was then mixed in an automatic plaster mixer that met the European Norm: EN 196-1 [159].

The ideal thickness for these novel photocatalytic plasters is to ensure a suitable workability was in the range 2 to 3 mm.

All the fresh samples prepared were cured for at least 28 days in an environmental chamber at 22°C (± 2°C); relative humidity of 53% (± 3%) before any testing and characterization was carried out. Samples are referred to as ETD, ETDK2, ETDK3 and EDTK5 corresponding to the percentage of K7000 incorporated into the plaster, 0, 2, 3 and 5 wt% respectively.

6. Determination of photocatalytic activity of powders and coatings

This chapter describes the different methodologies used for the determination of the photocatalytic performances of both powders and coatings. Liquid/solid interface reactions in powders were studied following the degradation of a solution containing methylene blue and the catalyst under UV and white light irradiation. Gas/solid interface reactions in powders were determined using a bespoke NO_x degradation reactor. Finally, coatings were studied using qualitative analysis employing commercial inks and also formaldehyde degradation in a bespoke reactor.

6.1 Determination of photocatalytic activity of nanoparticles aggregates using methylene blue degradation test

The PC activity was evaluated using an adaptation of the ISO/TC 206 standard [78] at the liquid solid interface by monitoring the degradation of a methylene blue (MB) solution, containing the nanoparticles. The solution was irradiated with ultraviolet (UV) light of wavelength 375-385 nm, visible green light of wavelength 525-535 nm and LED white light specified in the ISO 10678:2010 standard. The degradation was monitored quantitatively with a Jenway 6300 Spectrophotometer set at 670nm using deionized water for calibration in a 1 cm wide plastic cuvette. Initial absorbance of the MB solution was between 0.85 and 0.9 units depending on the sample. This value was recorded at the beginning of each experiment. To correlate the absorbance to the concentration the Lambert-Beer law was applied following equation 6-1

$$A=\varepsilon_\lambda lC \qquad 6\text{-}1$$

where: A is the absorbance; ε_λ is the molar absorption coefficient, typical for each compound and depending on the wavelength considered; l is the path length, in this case, was the width of the cuvette and C is the concentration of the dye.

For each sample sufficient drops of a 1 M solution of methylene blue was added to 100 ml of deionized water to obtain the appropriate initial value of absorbance. Approximately 0.1 g of powder then was mixed into these solutions. After a short period where the solution was stirred without irradiation the first sample of solution for measurement was extracted using a 10ml syringe and a filter unit (Sartorius Stedim, Minisart®, 0.10 μm)

to remove solid particles from the solution. After the first measurement, the light source was turned on to initiate the degradation reaction. A sample of the solution was taken at 5-minute intervals and a comparison made between commercially available and synthesised particles with different light sources.

6.2 NO_X reactor

The reactor employed for gas−solid phase tests operated under a constant flow of NO_x into the chamber, referred to as continuous conditions, as previously described in detail by Lucas et al. [127]. The reactor consisted of a chamber fabricated from a high-grade stainless steel cylinder (35 L in volume) with a stainless steel top equipped with a sealed quartz glass window, thereby allowing the sample, placed in a 6 cm petri dish, inside the chamber to be irradiated. A schematic diagram is shown in Figure 6-1. The light source employed was a solar lamp (Osram Ultra-Vitalux, 300 W, 280 to 780 nm), set at a distance 65 cm from the sample placed inside the chamber; the light intensity was measured with a radiometer (Delta OHM, HD2302.0, IT). Values were 3.6 W m^{-2} in the UV-A range and 25 W m^{-2} in the visible-light range. The temperature measured by means of a thermocouple in the chamber was 27 ± 1 °C. Throughout the tests a stable relative humidity of 31% was measured using a sensor located in the inlet pipe. A chemiluminescence analyser (AC-31M, Environment S.A) was used to record the concentration of the pollutant gas exiting the chamber.

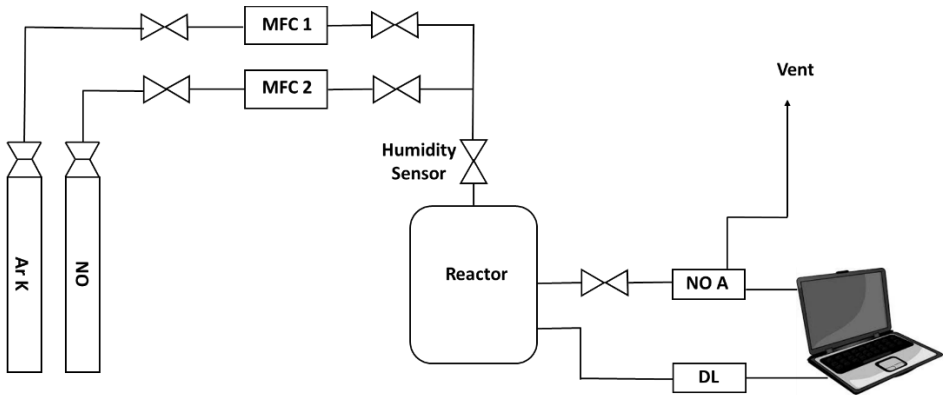

Figure 6-1 Schematic diagram of the NO_x degradation reactor showing the mass flow controller (MFC), NO analyser (NOA) and data logger (DL).

The experimental procedure involved firstly placing the petri dish containing the photocatalyst inside the reactor and covering the glass window with a sheet of aluminium to avoid irradiation inside the chamber. A pre-defined mixture of NO_x and air was automatically controlled in real time using a mass flow controller and introduced into the chamber at a flow rate of 1 L min^{-1} until a stable concentration of 0.2 ppm was reached. The condition of continuous flow and stabilisation of the concentration in the chamber was necessary to ensure saturation of the sample during the test. Under these experimental conditions, the photocatalytic process could be determined without the influence of the absorption of gas whether onto the sample or reactor surface influencing the measurements [160]. Once a concentration of 0.2 ppm was reached, the window glass was uncovered, the lamp turned on, and the photocatalytic reaction started. Measurements were carried out until the pollutant concentration stabilised to a minimum value meaning that any NO_x was no longer decomposed by the catalyst. The conversion rate (%) of the initial NO_x concentration was calculated using equation (6-2) [161] and used as an indicator of the photocatalytic activity.

$$(NO_x \text{ conversion})\ \% = \frac{(NO_x)_0 - (NO_x)_t}{(NO_x)_0} \times 100 \qquad (6\text{-}2)$$

where $(NO_x)_0$ is the initial NO_x and $(NO_x)_t$ is the NO_x after a certain irradiation time. Both these concentrations are expressed as ppmv

6.3 Determination of photocatalytic activity of coatings on MDF using Ink Intelligent dyes

Ink Intelligent dyes were employed to qualitatively evaluate the photocatalytic activity of the TiO_2 based coatings applied to the MDF substrates and Lime substrate. Ink Intelligent is a spin-off company from Queen's University, Belfast, UK. The company specialises in the production of inks that provide a rapid and reliable method of evaluating the photocatalytic activity of a substrate.

A semi-quantitative measure of the activity can be determined by monitoring the rate of colour change [162, 163]. Following application of the inks to the MDF specimen. the surface was irradiated with UV light (375-385 nm) of average intensity of 5.02 W/m^2.

The intensity was determined using a Deltha OHM photo radiometer HD 2102.1 with a UV Probe of spectral range from 315 nm to 400 nm and irradiance range from 0.1 mW/m^2 to 2000 W/m^2. Three different inks with different sensitivities were employed.

The Validator ink (patented dye) was the lowest sensitivity dye, suitable for surfaces of low PC activity, the Explorer (Resazurin based dye) was suitable for medium activity surfaces and the Visualiser (Basic Blue 66 based dye) was sensitive for high activity surfaces. As the activity of the surface was unknown all specimens were evaluated using all three dyes described above simultaneously. Testing followed the same protocol with half of the dye-coated-surface covered with aluminium foil during irradiation. This allowed a comparison of colour change between irradiated and non-irradiated surfaces to be made

6.4 Photocatalytic formaldehyde degradation test

A custom-made experimental set-up, based on the ISO standard 18560-1 [164] was developed for the evaluation of photocatalytic formaldehyde degradation performance, Figure 6-2 at the Fraunhofer Institute for Building Physics IBP. This section describes the operation of the equipment (which was carried out at IBP) and the methodology applied to analyse and interpret the results obtained. Samples were placed in 28.2 L test chambers sealed on the top by a special type of borosilicate glass with a 100% transmission down to a wavelength of 350 nm. Flexibly adjustable slot floors in the test chamber, kept the surface of the sample at 5 mm below the glass panel, regardless of the sample height. The fluorescent tubes were placed on top of the glass windows. The air flow was fed through the gap between the glass panel and the surface of the sample in the test chamber after which, the exhaust was divided into two streams allowing both on-line and offline analysis. The whole system included a total of six test chambers for parallel operation.

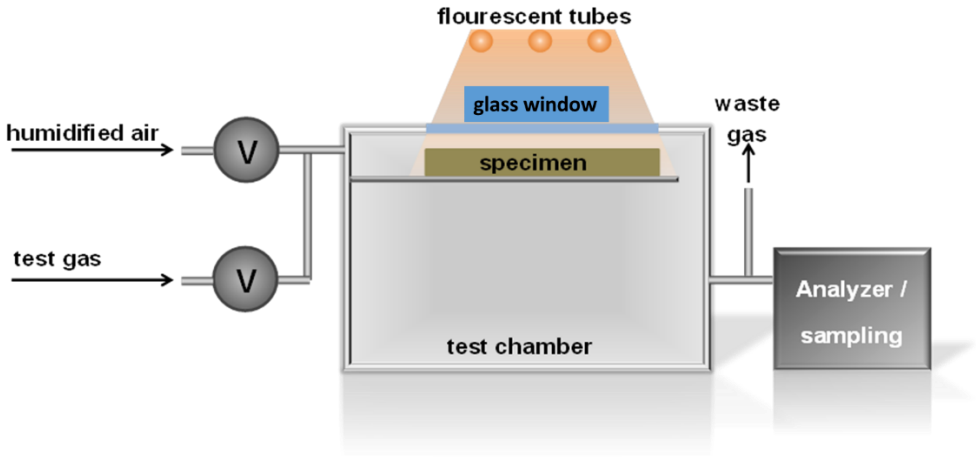

Figure 6-2 Photocatalytic formaldehyde degradation test chamber assembly, schematic.

A flowmeter was connected in line with the gas supply to each chamber and adjusted in order to ensure an equal flux of test gas was delivered to all six test chambers as seen in figure 6.3.

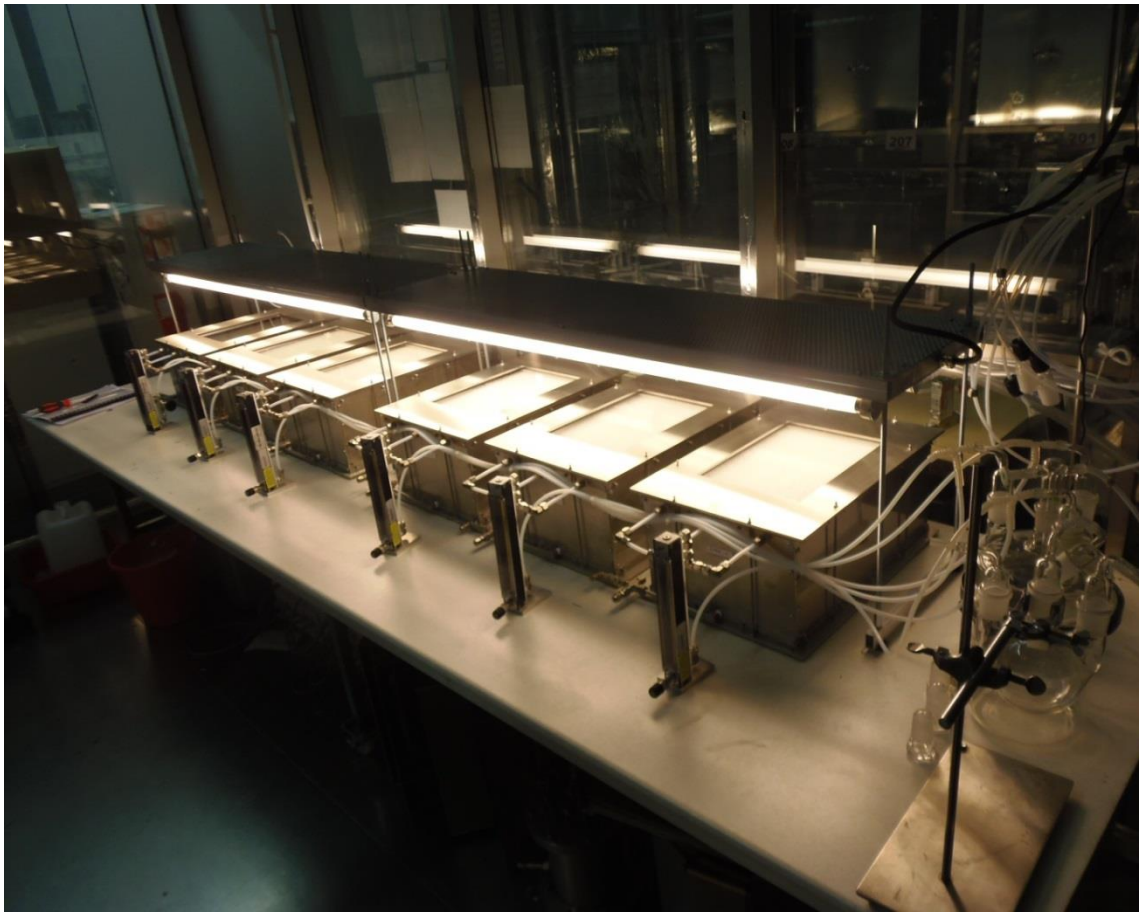

Figure 6-3 Assembly of the six test chambers in the glass cabin.

The test gas was enriched through the addition of calibration gases which contained approximately 15ppm of formaldehyde in nitrogen. A total flow of 1.6L/min comprised of both neutral air and test gas containing the pollutants was regulated using mass flow controllers. Tests were conducted under irradiation from Osram Lumilux warm white 36W tubular fluorescent lamps of 26 mm diameter mounted to G13 bases which ensured the entire irradiated area was illuminated evenly. This type of lamp is one commonly used for indoor lighting, e.g. in offices.

The concentration of formaldehyde was measured using an AL4021 analyser manufactured by Aero-Laser GmbH (Garmisch-Partenkirchen, Germany). Fluorescent emission after the reaction of formaldehyde with acetylacetone and ammonia was measured in a linear detection range between 0.1 and 3000ppb with a detection limit of 0.1ppb. The analyser was calibrated beforehand for a measurement range between 0.1 and 400ppb.

6.5 Photocatalytic formaldehyde degradation

In the course of this test for photocatalytic formaldehyde degradation under visible light, four different phases were studied: In Phase 1, the chamber was flushed with neutral air. Here the intrinsic emissions from the specimen without exposure to light could be detected. In Phase 2, the chamber was flushed with neutral air and the lamps (visible light) were turned on irradiating the specimen surface. This was done in order to examine the light-induced emission of formaldehyde from the samples. In Phase 3, additional gas with an airflow of 1,65 l/min and a concentration of formaldehyde of approximately 90 ppb (a total of 12.2 µg/h of formaldehyde) is introduced over the surface of each sample with the lamps still turned on. Thus, at this stage, the photocatalytic degradation of formaldehyde by the sample can be detected. In Phase 4, the lights were switched off and the addition of the formaldehyde was continued. Thus, the adsorption of formaldehyde by the sample could be determined at this stage. All phases were maintained until a stable formaldehyde concentration status was reached for all samples. For these samples, a total of 839 hours were required to carry out all phases of the test. An example of a formaldehyde degradation test profile is shown in Figure 6-4.

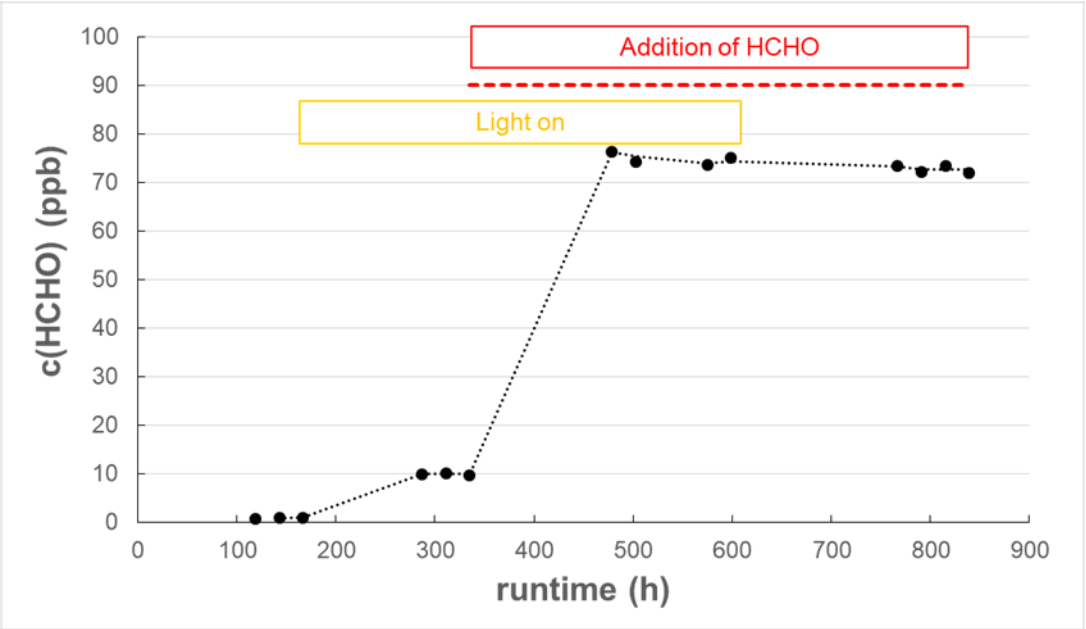

Figure 6-4 Typical photocatalytic formaldehyde degradation test profiles for ETDK2. The red line represents the incoming concentration of formaldehyde during phase 3 and 4.

From the equilibration formaldehyde concentrations in the different testing phases, the desired variables are defined as shown below. For every phase, the resulting formaldehyde concentration can be calculated by (6-3):

$$cRes = cin + cProdO + cProdL – cRedL - cRedA \quad (6\text{-}3)$$

where

cRes = resulting formaldehyde concentration

cin = formaldehyde concentration measured in the empty reference chamber

cProdO= formaldehyde concentration from own emission of the specimen

cProdL= formaldehyde concentration from own emission caused by radiation

cRedL = reduction of formaldehyde concentration caused by radiation

cRedA = reduction of formaldehyde concentration caused by adsorption

For the different phases of the experiment (see Figure 6-4), the resulting formaldehyde concentration can be calculated using the following equations:

$$cRes(phase1) = cProdO \quad (6\text{-}4)$$

$$cRes(phase2) = cProdO + cProdL \quad (6\text{-}5)$$

$$cRes(phase3) = cin + cProdO + cProdL – cRedL - cRedA \quad (6\text{-}6)$$

$$cRes(phase4) = cin + cProdO - cRedA \quad (6\text{-}7)$$

And the specimen performance parameters are obtained from the following equations:

$$cRedL = cRes(phase4) - cRes(phase3) + cRes(phase2) + cRes(phase1) \quad (6\text{-}8)$$

$$cProdL = cRes(phase2) - cRes(phase1) \quad (6\text{-}9)$$

$$cRedA = -cRes(phase4) + cRes(phase1) + cin \quad (6\text{-}10)$$

Based on the equilibrium concentrations, the reduction rates of formaldehyde (either caused by photocatalytic reactions or by adsorption) can be calculated for the different samples. Equations (6-8) and (6-10) were used and a normalisation in relation with the incoming air (89.9 ppb) was carried out to compare the results.

7 Pure and Cobalt doped TiO_2

The aim of this chapter is to fully characterise and analyse sol-gel synthesised cobalt doped TiO_2 (macro-pictured in Figure 7-1 a) by using, XRD, UV-Visible diffusive spectroscopy, Raman spectroscopy, He Beam, SEM, FESEM and TEM comparing them with commercially available TiO_2 particles. The photocatalytic performance was studied in the aqueous phase as well as the gas phase, previously described in Chapters 4, 5 and 6

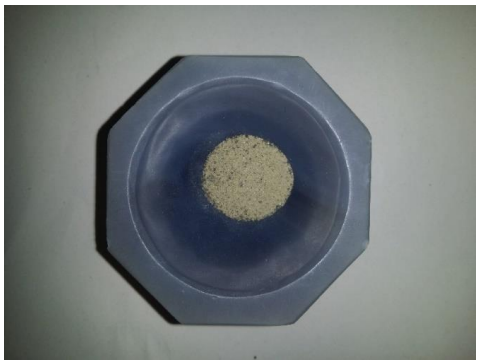

a)

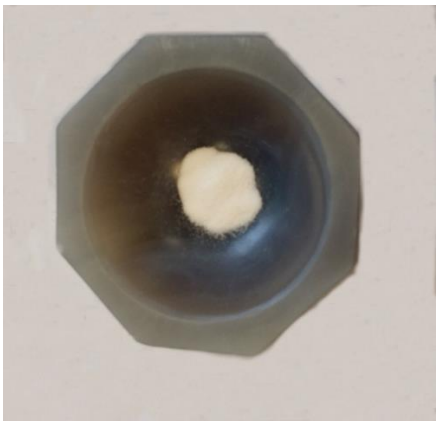

b)

Figure 7-1 a) Cobalt doped TiO_2 aggregated nanoparticles during the milling process using an agate mortar and pestle, b) Pure TiO_2 aggregated nanoparticles during the milling process using an agate mortar and pestle.

The synthesis process described in chapter four was followed by annealing which resulted in greater aggregation. A milling stage was then carried out to reduce the dimension of the aggregates as much as possible.

7.1 Scanning electron microscopy

The morphology of nanoparticles at different magnifications was studied using SEM. During the thermal treatment, sintering was evident between the nanoparticles which led to the formation of aggregates. Figure 7-2a) and b) reveal large aggregates of nanoparticles around 100 microns wide together with smaller aggregates, from 1 to 30 microns wide in both first batch samples annealed at 450°C and 550°C.

SEM images of undoped TiO_2 and the second batch of cobalt-doped TiO_2 are presented in Figure 7-3 a) and b) respectively. All the aggregates are formed from individual nanoparticles as shown in both pictures.

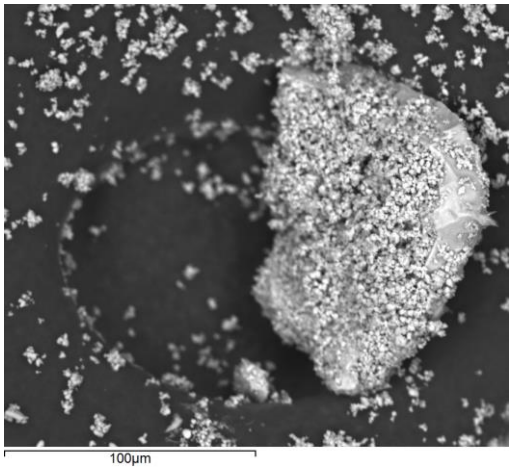

a)

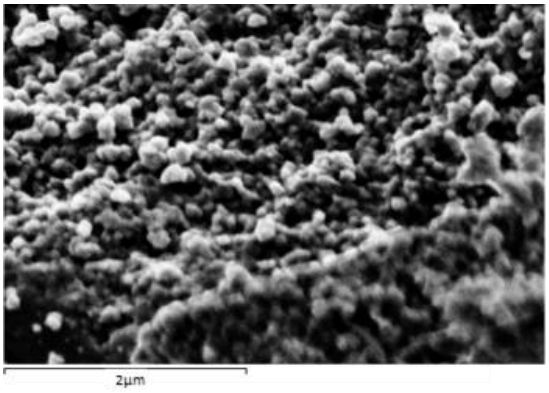

b)

Figure 7-2 a) SEM image of first batch Co-doped TiO_2 annealed at 550°C with a scale bar = 100 microns, b) SEM image of the surface of the first batch of TiO_2 Co-doped aggregate annealed at 550°C with scale bar = 2 microns.

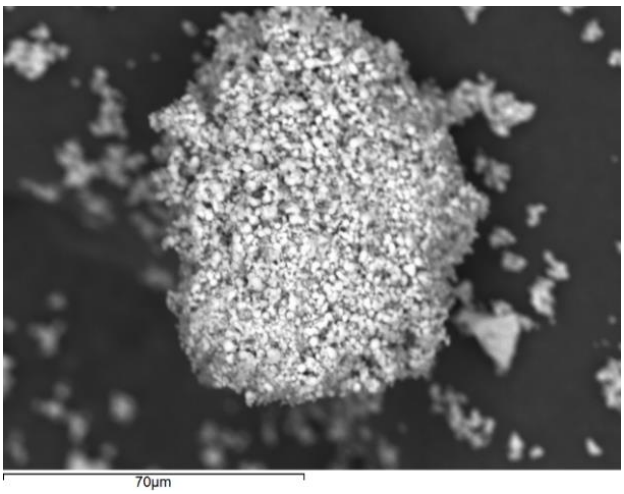

a)

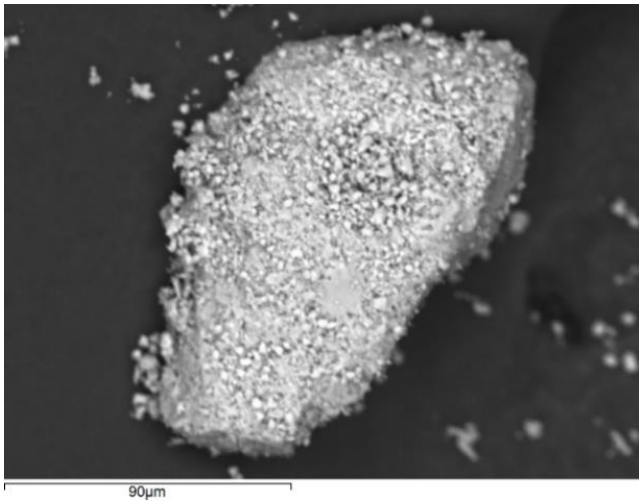

b)

Figure 7-3 a) SEM image of the second batch of an aggregate of pure TiO_2 nanoparticles b) SEM image of the second batch of an aggregate of cobalt doped TiO_2 nanoparticles.

7.2 He beam microscopy, field emission scanning electron microscopy images and transmission electron microscopy images

He beam, field emission and transmission electron microscopy were employed to better understand aggregation of the nanoparticles and the morphology of the surface of the samples.

Figure 7-4 a) and b) together Figure 7-5 a) and b) show how the presence of cobalt in the lattice does not significantly modify the surface structure or the aggregates morphology.

The transmission electron microscope image in Figure 7-6 a) reveals the driving force for aggregation into nano-metric particulate aggregates. Figure 7-6 b) suggests that the direction of the crystalline planes varies with no preferred nucleation direction showing nanoparticles with various lattice directions overlapping.

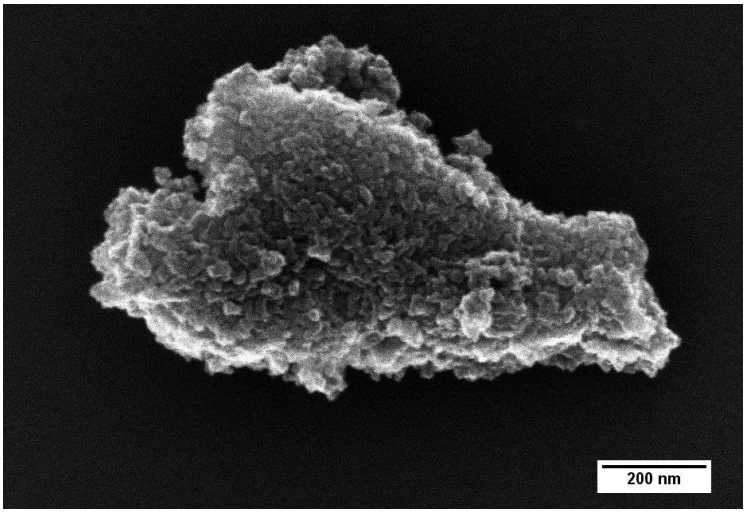

a)

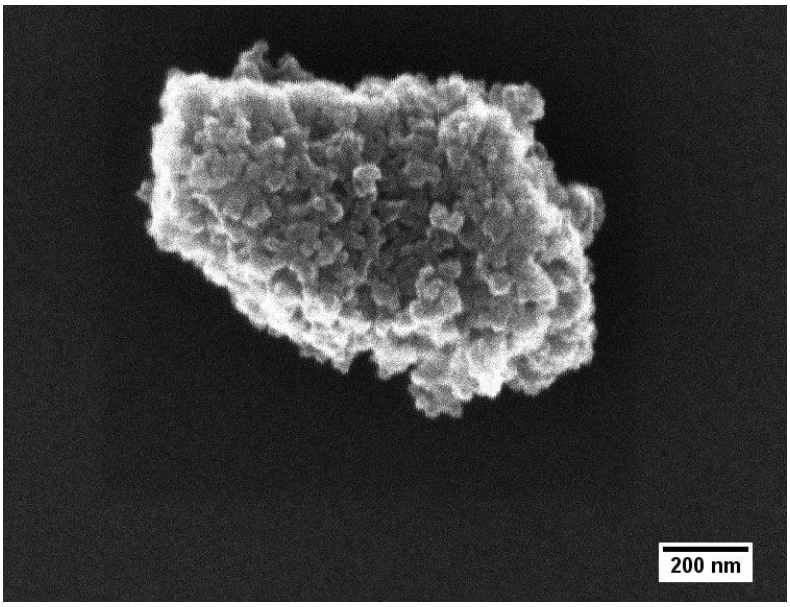

b)

Figure 7-4 a) He beam image of aggregated Co-doped TiO_2 particles with scale bar = 200 nm b) He beam image showing the nanostructures of undoped TiO_2 particles with scale bar = 200 nm.

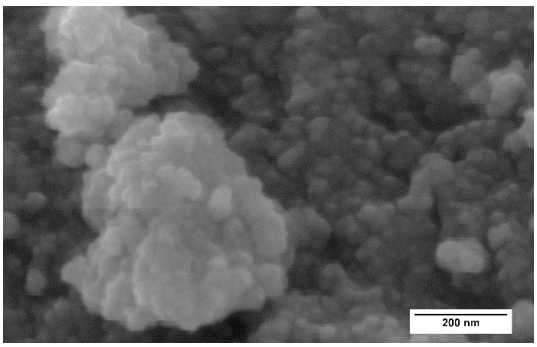

a)

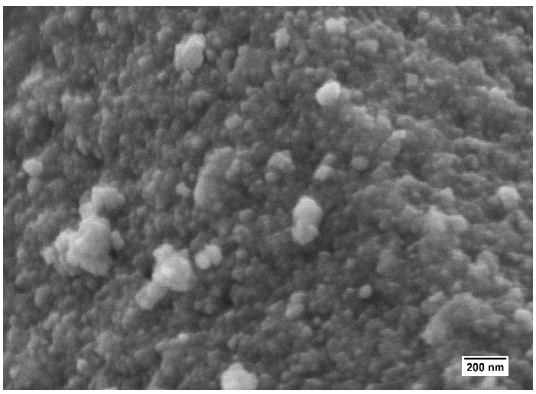

b)

Figure 7-5 a) FE-SEM image of aggregated Co-doped TiO_2 particles with scale bar = 200 nm b) FE-SEM image showing the nanostructures of undoped TiO_2 particles with scale bar = 200 nm.

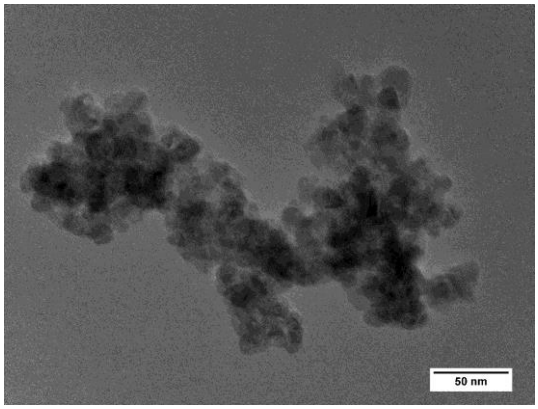

a)

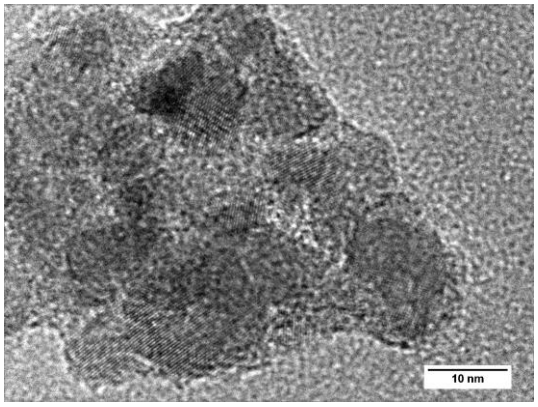

b)

Figure 7-6 a) High magnification TEM image of cobalt doped TiO_2 nanoparticle aggregate, b) high magnification TEM image of cobalt doped TiO_2 showing atomic planes and lattice.

7.3 X-ray diffraction

As previously described in chapter 4 the first batch of synthesised cobalt doped TiO_2 was annealed at two different temperatures. XRD patterns for the two annealing temperatures were generated for the two batches. The XRD pattern in Figure 7-7 a) shows that the sample annealed at 450°C has peaks at 2-theta values of 25° and 48° which are typical of an anatase crystalline phase. The low noise/signal ratio is due to the low crystallinity of

the sample synthesized and a possible contamination in the detector of the X-ray diffractometer. The sample annealed at 550°C in Figure 7-7 b) shows peaks typical of the rutile structure at 2-theta values of 27°, 36° and 55°. Moreover, the presence of anatase is noticeable from the same peaks observed in the sample annealed at 450°C as well as the peaks from rutile and brookite. All the peaks correspond to the standard reference data (JCPDS no.: 88-1175 and 84-1286) [165].

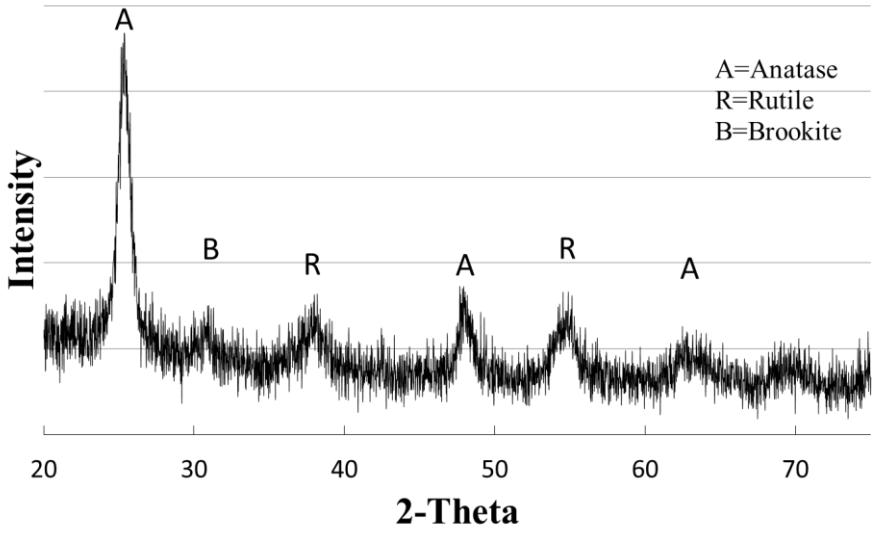

a)

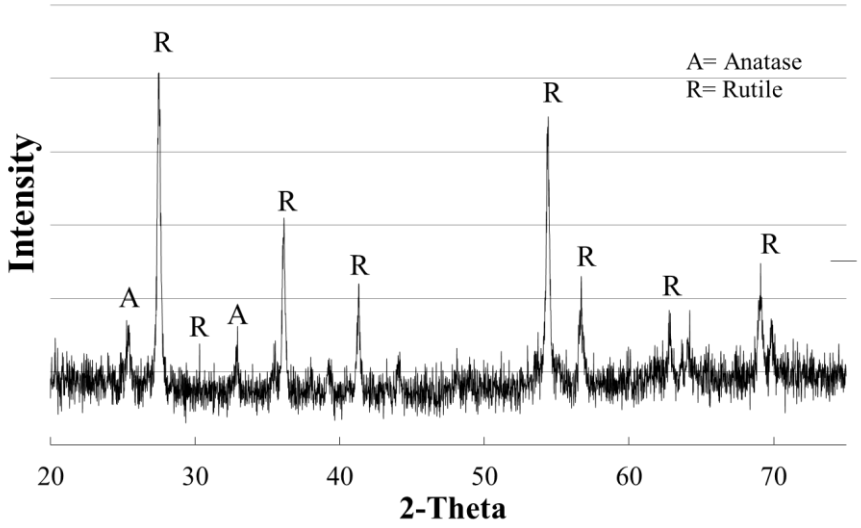

b)

Figure 7-7 a) X-ray powder diffraction pattern of Co-doped TiO_2 annealed at 450°C b) X-ray powder diffraction pattern of Co-doped TiO_2 annealed at 550°C.

XRD patterns of the second batch of pure and cobalt doped TiO_2 specimens are presented in Figure 7-8; Quantitative phase analysis (QPA) data are reported in Table 7-1.

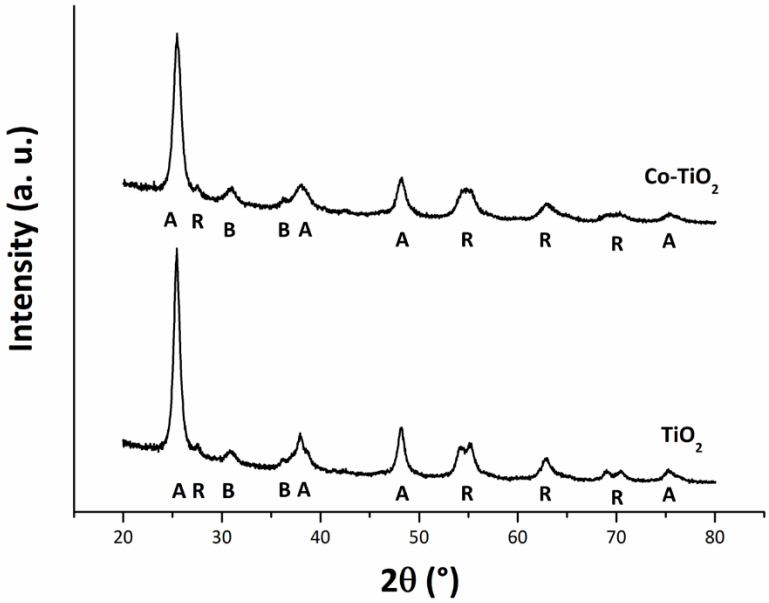

Figure 7-8 XRD patterns of second batch specimens (k – A, R and B are symbols, standing for anatase, rutile and brookite, respectively.

Table 7-1 Rietveld agreement factors and crystalline phase composition of the prepared specimens.

Sample	**No. of variables**	**Agreement factors**			**Phase composition (wt%)**		
		$R(F^2)$ (%)	R_{wp} (%)	χ^2	anatase	rutile	brookite
K7000	22	3.56	4.31	1.98	100	0	0
TiO_2	22	2.33	4.14	1.45	67.7	3.9	28.4
Co-TiO_2	22	2.28	3.97	1.32	59.9	3.5	36.6

As shown in Table 7-1, the synthesized specimens contain the three most abundant TiO_2 polymorphs. Unmodified TiO_2 contain 67.7 wt% anatase, 3.9 wt% rutile and 28.4 wt% brookite. Co-TiO_2 is composed of 59.9 wt % anatase, 3.5 wt % rutile, and 36.6 wt % brookite. The strong presence of brookite has to be ascribed to the acidic conditions of the synthesis [166]. On the other hand, the presence of cobalt favoured the brookite crystallization at the expense of anatase. Whilst the cobalt doped and undoped TiO_2 contain the three polymorphs and no amorphous phases, the commercial K7000 consist of anatase.

Microstructural features of the synthesized specimens are reported in Table 7-2. The primary average crystalline domain size of anatase in the commercial TiO_2 specimen is 3.3 nm. The presence of cobalt in the synthesized sample increased this dimension to 6.7 nm, as the anatase in the undoped TiO_2 is 9.0 nm in size. The average crystalline domain sizes of rutile and brookite are 7.6 and 8.9 nm for the undoped TiO_2, and 12.4 and 8.6 nm for the cobalt doped TiO_2, respectively.

Table 7-2 Mean crystalline domain diameter for K7000, undoped TiO_2 and Co-doped TiO_2 for anatase, rutile and brookite.

Sample	**Mean crystalline domain diameter**		
	$\langle D_{ant} \rangle$ **(nm)**	$\langle D_{rt} \rangle$ **(nm)**	$\langle D_{brk} \rangle$ **(nm)**
K7000	3.3±0.1	0	0
TiO_2	9.0±0.9	7.6±0.4	8.9±0.4
Co-TiO_2	6.7±0.6	12.4±2.6	8.6±0.3

7.4 Raman spectroscopy

A confirmation of the results from the XRD patterns is given by Raman spectra obtained for all the samples including the commercial NPs shown in Figure 7-9 to Figure 7-13.

Raman spectra of the commercial particles of K7000 and P25 used as a comparison for doped and undoped TiO_2 particles are showed in Figure 7-9 and Figure 7-10. As expected bands characteristic of anatase are found.

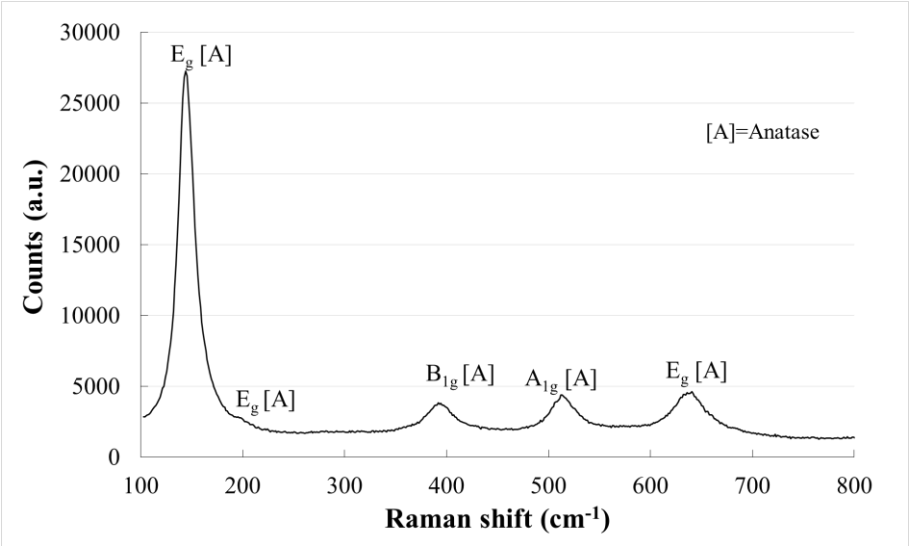

Figure 7-9, Raman spectrum for K7000.

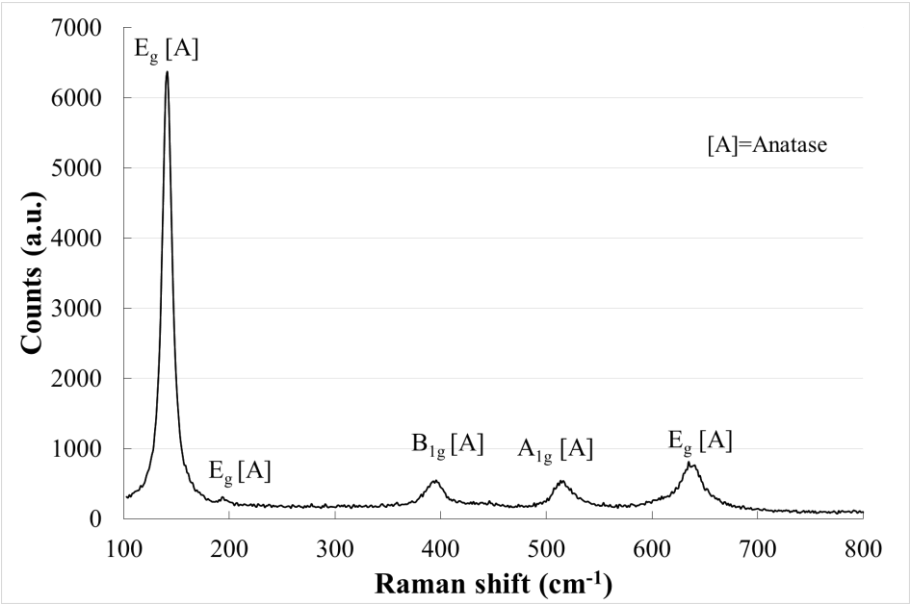

Figure 7-10. Raman spectrum for P25

Raman spectra for pure TiO_2 and the two samples of cobalt doped TiO_2 are presented in Figure 7-11 to Figure 7-13. The Raman spectra of the three synthesised particles reveal the presence of the same phases identified by the XRD studies.

With regarding cobalt doped TiO_2, in the sample annealed at 550°C a significant amount of rutile is detected from the presence of the E_g and A_{1g} peaks as reported in the literature [167, 168] and the presence of the A_{1g} peak at 700 cm^{-1} from CoO [169].

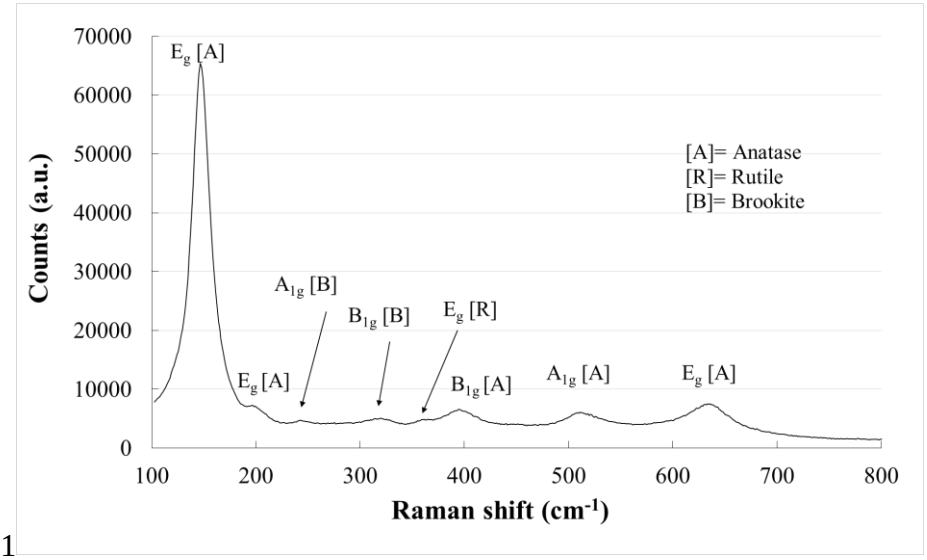

1

Figure 7-11. Raman spectrum for pure TiO_2.

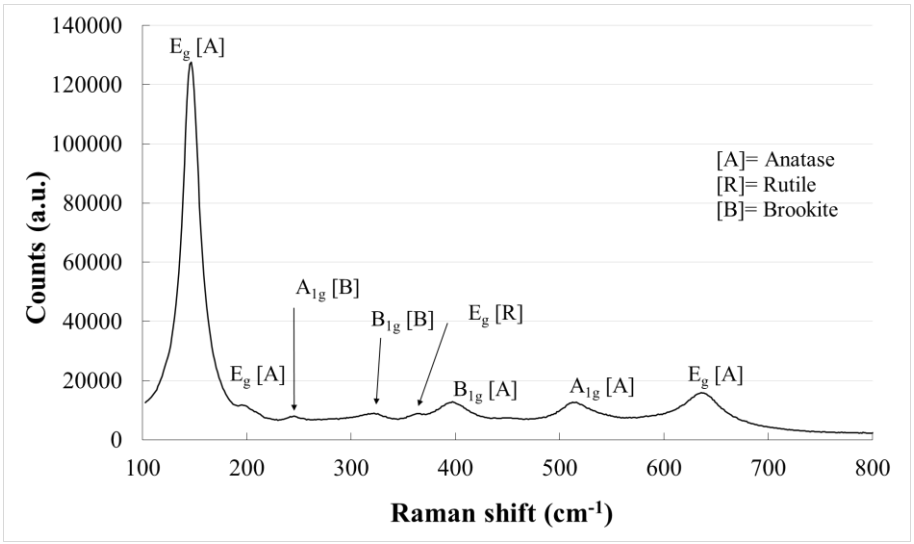

Figure 7-12 Raman spectrum for Co doped TiO_2 annealed at 450°C.

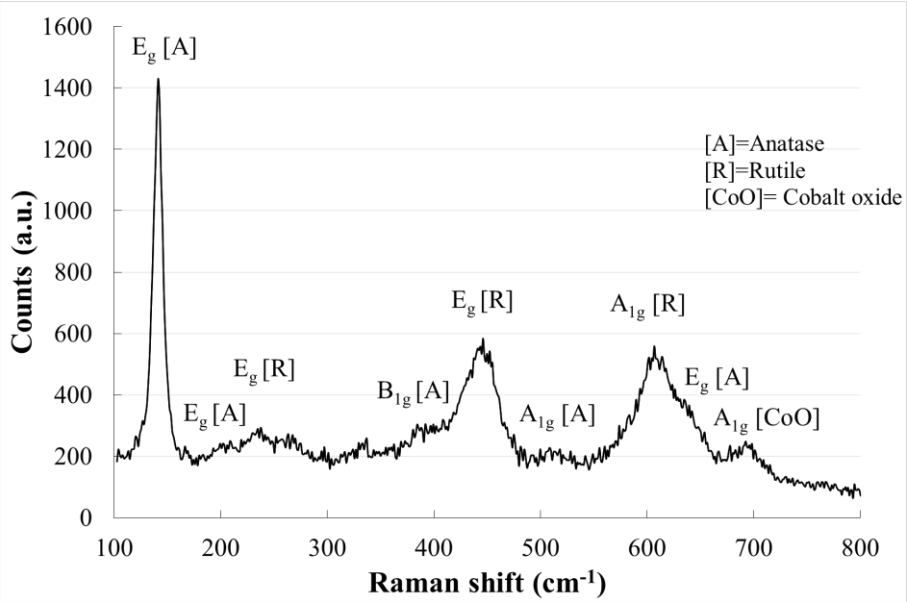

Figure 7-13 Raman spectrum for Co doped TiO_2 annealed at 550°C.

7.5 Diffuse reflectance spectroscopy and Brunauer–Emmett–Teller surface area analysis (BET)

Diffuse reflectance spectroscopy (DRS) results are shown in Figure 7-14 Figure 7-15 and Table 7-3. All the spectra consist of one single absorption edge at around 390 nm in TiO_2.

The values of the optical E_g of the specimens, obtained through the Tauc plot, are listed in Table 7-3. The indirect allowed model (Figure 7-15) fits well to this TiO_2 band structure because the E_g values obtained are consistent with the expected E_g for rutile (*i.e.* 3.0 eV, in agreement with data in previously published literature [170]).

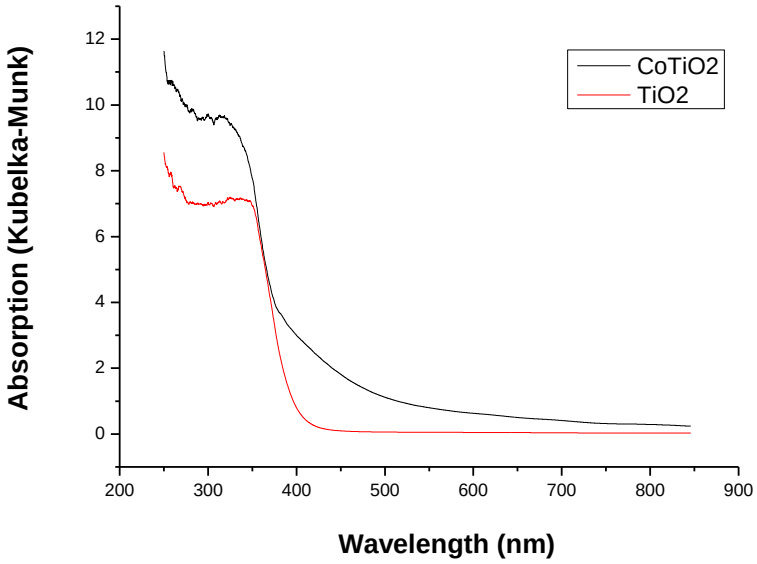

Figure 7-14 Diffuse reflectance spectroscopy (DRS) of the Pure and Co doped specimens.

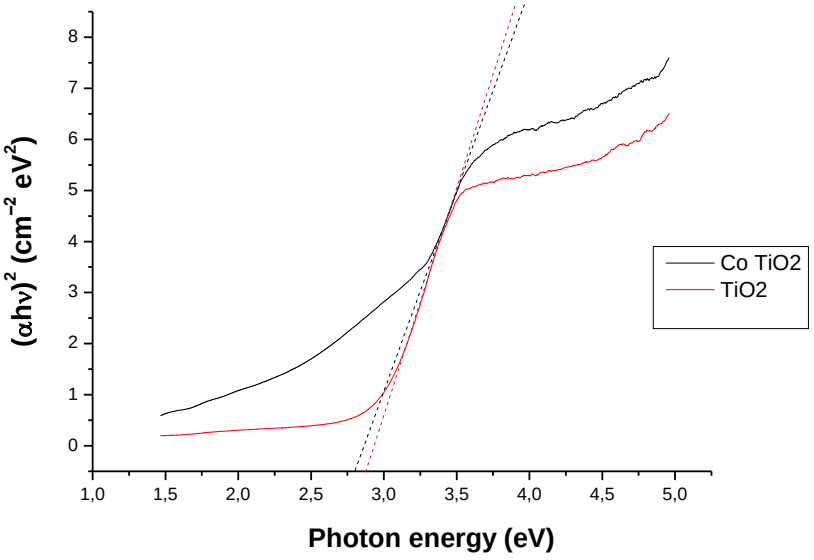

Figure 7-15 Kubelka–Munk elaboration versus photon energy (Tauc plot) according to the INDIRECT E_g model on Pure and Co doped TiO_2. The dashed red and black lines represent the x-axis intercepts of the line that is tangent to the inflexion point of the curve.

Table 7-3 Optical band gap of synthesised and commercial TiO_2.

Sample name	Optical Eg (eV)
P25	3.26 [171]
Pure TiO_2 second batch	2.87
Co-TiO_2 second batch	2.80

BET surface area analysis was carried out an all sol-gel synthesised nanoparticles and commercial TiO_2 to allow a comparison. The BET surface area for the sol-gel TiO_2 was comparable with the commercial P25. The Co-doped TiO_2 was constituted by nanoparticles aggregated in lumps of various dimensions. K7000 results are noteworthy because particle sizes observed in the TEM/FESEM for K7000 and P25 are remarkably similar.

Table 7-4 BET surface area for commercial and synthesised TiO_2 particles.

Sample name	Surface area (m^2/g)
K7000	225.4
P25	65.3
Pure TiO_2 first batch	49.6
Co-TiO_2 first batch annealed at 450°C	59.5
Co-TiO_2 second batch	79.2

7.6 Photocatalytic activity

Photocatalytic activity of particles on different interphases was studied with two tests: liquid/solid phase activity was measured following methylene blue (MB) degradation, whereas the gas/solid interphase activity was measured by assessing NO_x degradation.

7.6.1 Methylene blue degradation tests

By initial observation of the process of degradation of the methylene blue two different interactions occurred between the particles and the dye. During the initial five or ten minutes after initial mixing, the dye adsorbed on the surface of the nanoparticles.

Following this, the dye then desorbed and consequently reacted with the NPs thereby degrading the dye itself. In order to show the trends more clearly the data from the different particles was normalized. This was achieved by dividing the measured concentration by the value of maximum concentration after desorbing.

Under irradiation by UV light, the commercial P25 showed the best performance when compared with the first batch of Co-doped TiO_2, as observed in Figure 7-16. This could be due to the energy gap of pure TiO_2 that is excited by UV light.

The first batch of Co-doped TiO_2 was annealed at two different temperatures to allow a comparison between the different structures obtained. Under the green light (525-535 nm) the synthesised TiO_2 indicated that commercial carbon doped NPs (Kronoclean7000 ®) Co-doped TiO_2 have comparable performance under the visible light as displayed in Figure 7-17.

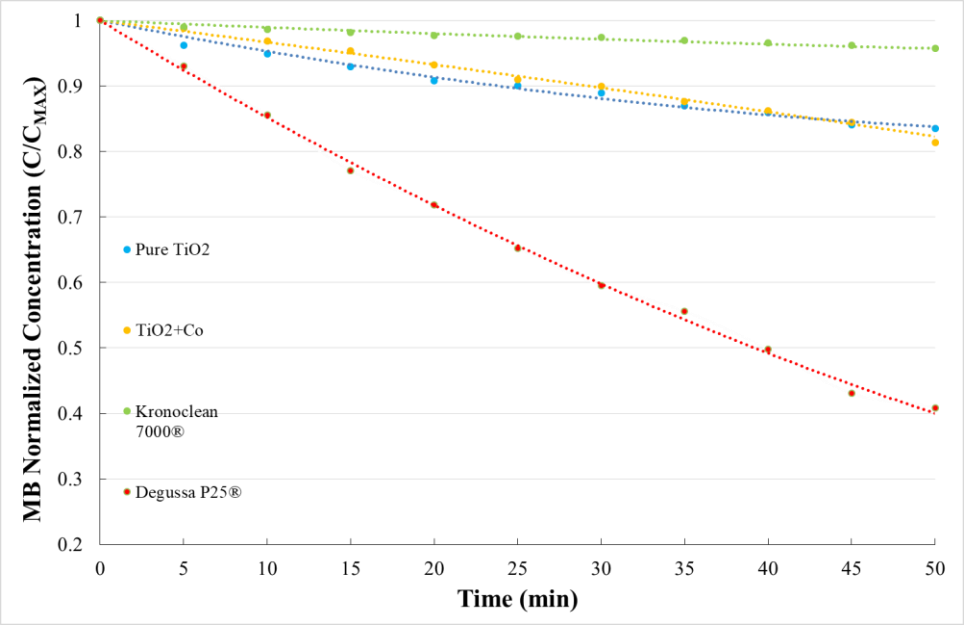

Figure 7-16 Methylene blue degradation under UV light (325-335 nm) for the first batch of Co doped samples and commercial particles as a function of time.

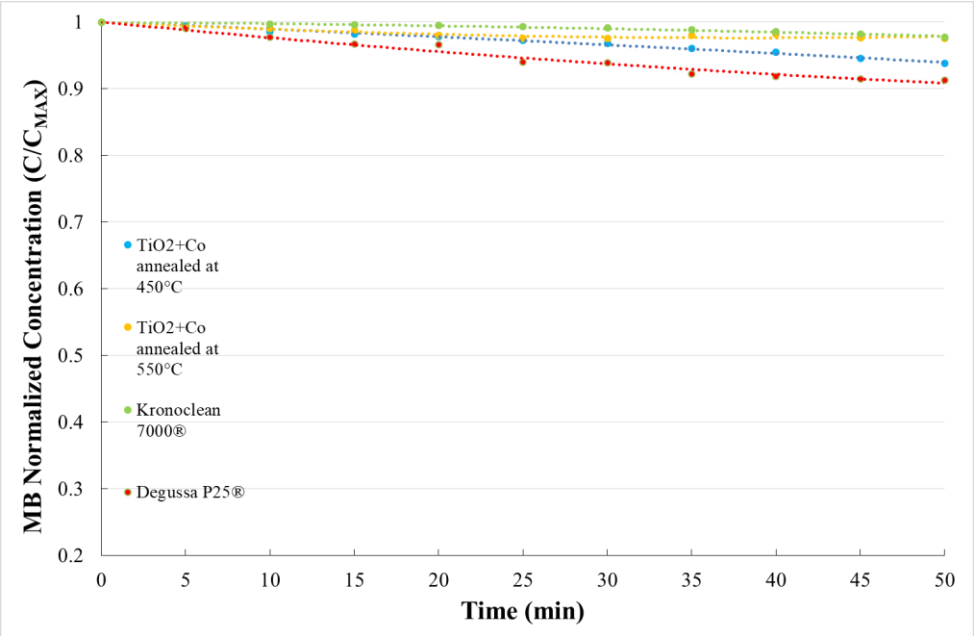

Figure 7-17 Methylene blue degradation test under green light (525-535 nm) for the first batch Co-doped samples and commercial particles as a function of time.

The second batch of doped and undoped TiO_2 was tested irradiating the solution of methylene blue with a white high power LED lamp (5000k and 150 Lumens) shown in Figure 7-18 and with UV light (325-335 nm) in Figure 7-19. Under white light, the performance of Co doped TiO_2 is superior to P25 with almost 20% more MB degraded after 50 min and compared to the pure TiO_2 which performed comparably with P25 shown in Figure 7-18.

Figure 7-19 shows that the Co-doped TiO_2 performs as well as P25 under UV irradiation with the pure TiO_2 just slightly less effective than that of the doped material.

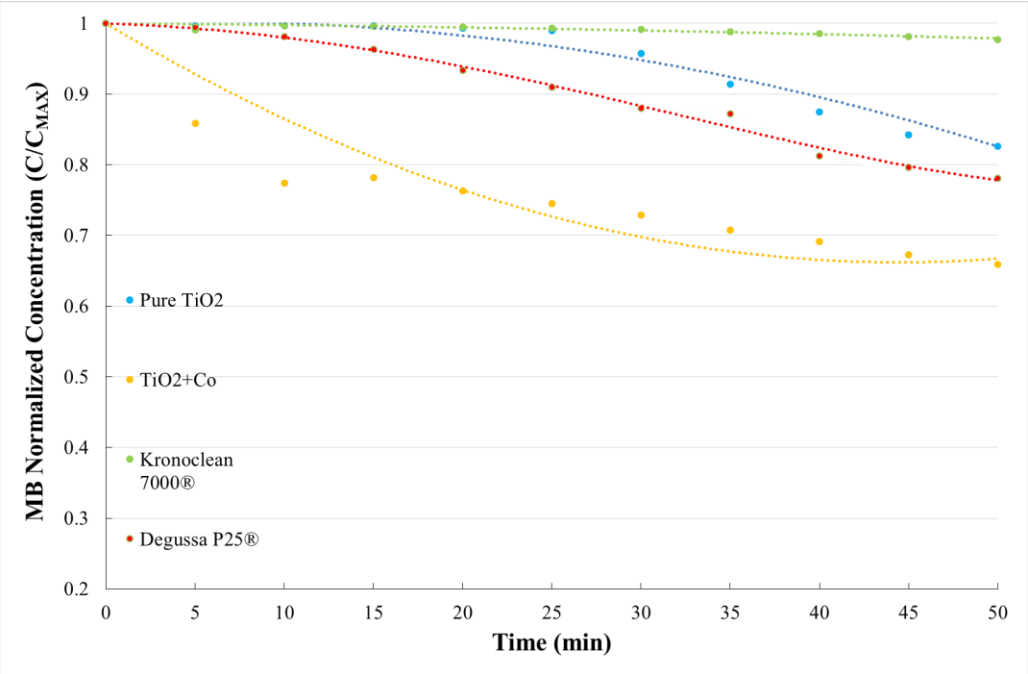

Figure 7-18 Methylene blue degradation test under white LED light for second batch Co-doped and pure samples and commercial particles as a function of time.

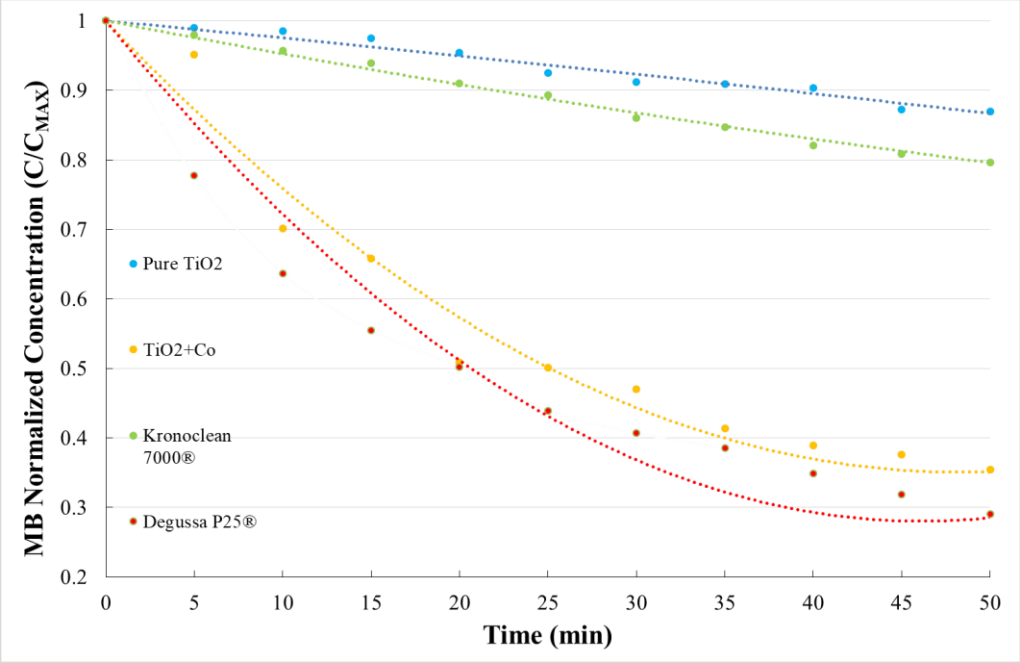

Figure 7-19 Methylene blue degradation test under UV light (325-335 nm) on second batch samples and commercial particles.

7.6.2 NO_x degradation test

The conversion rate (%) of the initial NO_x concentration was calculated using the procedure described in chapter 6 and is plotted in Figure 7-20, the data plotted are an average over three consecutive tests.

All the trends in the reduction of NO_x concentration by photocatalytic activity for the three particles studied are similar. Despite having the commercial P25 more effective than sol-gel samples the difference is slight making them suitable for application in an indoor environment. As seen in Figure 7-20, following an initial degradation, the pollutant concentration reached a plateau, and the samples could no longer keep on decomposing nitrogen oxides – this is particularly noticeable for P25. This deactivating behaviour of TiO_2 is well-known to be caused by the oxidation of NO_2 to HNO_3 [172]. The O_2^- and $OH^{\cdot}$ radicals formed during photocatalysis react with the pollutant gas, produce NO_2 and HNO_3. However, that formed HNO_3 is easily dissolved in water [173].

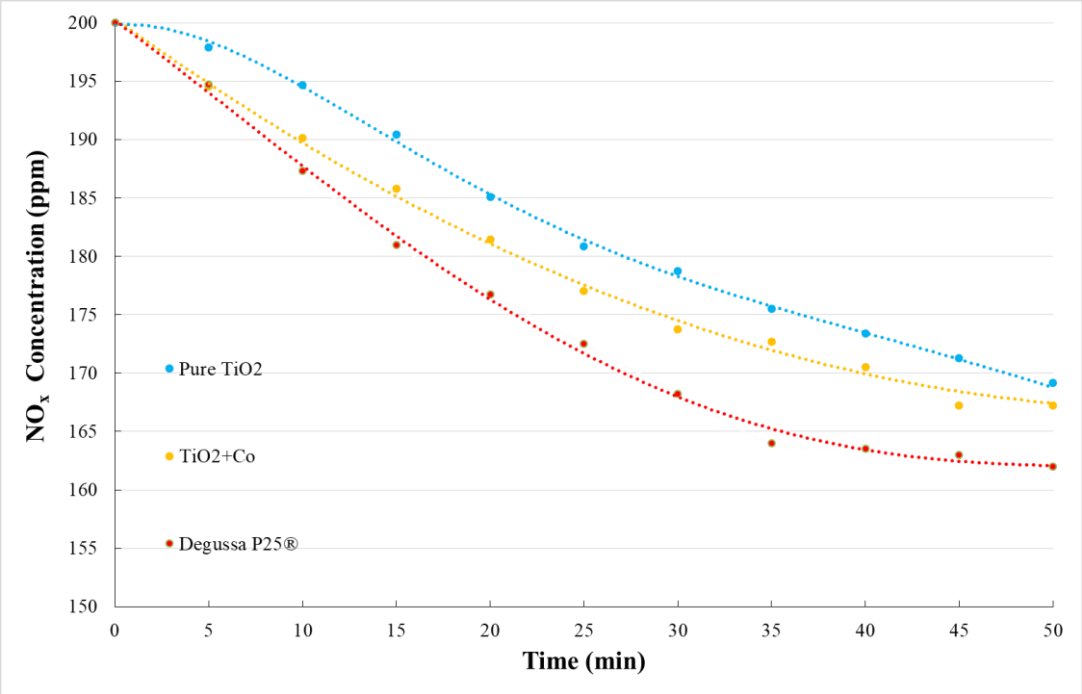

Figure 7-20 Decomposition of NO_x by PC reaction of the nanoparticles irradiated with an Osram Solar lamp. The light was switched on after a period of stabilization were all the NO_x filled the chamber at min 0.

7.7 Conclusions

The following conclusion can be drawn from this chapter:

- Sol-gel synthesis was successfully modified between the first and second batches in order to increase the amount of crystalline anatase in the sample although nanoparticle aggregation was still heavily present.
- Higher levels of aggregation could explain the difference in BET surface area between all the synthesised samples when compared to commercial particles.
- Annealing treatment temperatures is a major variable in terms of the crystalline phases obtained. In the first batch annealed at 550 °C, there was a higher amount of rutile when compared to annealing at 450 °C.
- The second batch contained all the three major polymorphs supported by both XRD and Raman spectra.
- Methylene blue degradation under UV light for the first batch of synthesised and commercial particles confirmed that P25 caused the highest degradation rates but became comparable with the Co-doped samples when irradiated with visible light
- Methylene blue degradation under UV light of the second batch of cobalt doped and P25 particles was comparable in contrast to the first batch.
- Degradation test under visible light for the second batch of synthesised and commercial particles demonstrated that cobalt doped particles degrade 25% more methylene blue than the reference P25 supporting their application in visible light active PC coatings.
- NO_x degradation tests showed that synthesised and commercial particles behaved similarly and the percentage of NO_x removed was the same as a function of time when irradiated with Osram visible light.

8 Tungsten doped TiO_2

The aim of this chapter is to present results from the characterization and analysis of the sol-gel synthesised tungsten doped TiO_2. Specimens containing varying proportions of tungsten were characterised using XRD, UV-Visible diffusive spectroscopy, Raman spectroscopy, FESEM and TEM. Comparisons were then made with commercially available TiO_2 particles. The photocatalytic performance was studied in both the aqueous and gas phase, as previously described in Chapters 4, 5 and 6.

8.1 Electron microscopy

The microstructure of the nanoparticles was imaged using field emission (FE) electron microscopy in order to compare the morphology of the nanoparticle formulations with different tungsten contents. Transmission electron microscopy was employed to examine the particle size and lattice structure.

Field emission scanning electron microscopy images

The microstructure of formulations containing 1, 2.5 and 3% tungsten are presented in Figure 8-1 a) to Figure 8-3. Figure 8-1 a) and b) show 1% W doped TiO_2 at magnifications of 30k and 85k. Examination of the images shows that the particles are in a sintered state. The size of the particles was measured manually using the image analysis software, Image J. which showed an average dimension of 66 ± 10 nm. Figure 8-2**Error! Reference source not found.** shows the 2.5% W doped TiO_2 at the same two magnifications as for the 1% W doped TiO_2. The images indicate that the 2.5% W doped TiO_2 particle sizes are very similar to the 1% W doped TiO_2 and also exhibit a similar morphology and microstructure with an average dimension of the particles of 66 ± 11 nm.

In comparison Figure 8-3 a) and b) show the microstructure of 3% W doped TiO_2 again at the same two magnifications. The morphology is noticeably different in this case with a more porous structure comprised of larger particles with an average dimension of 130 ± 28 nm.

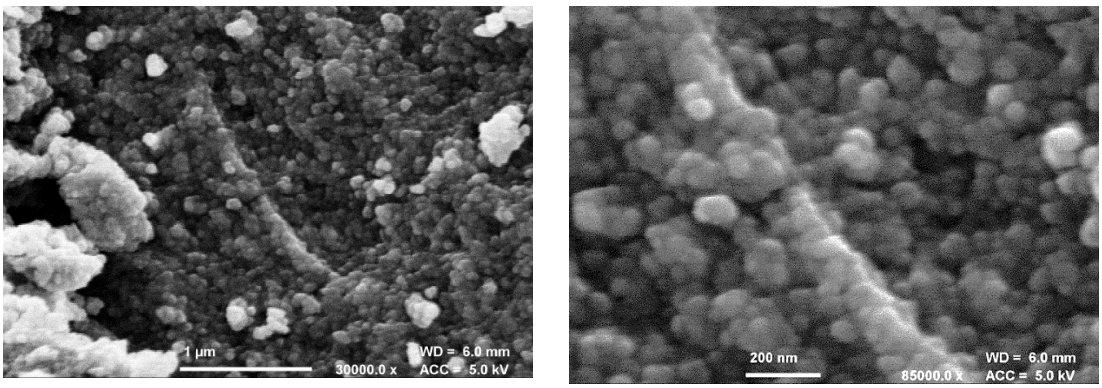

a) b)

Figure 8-1 a) SEM image of the surface of the 1% W-TiO_2 sample with scale bar equals 1 micron, b) higher magnification SEM image of surface of the 1% W-TiO_2 sample with scale bar equals 200nm.

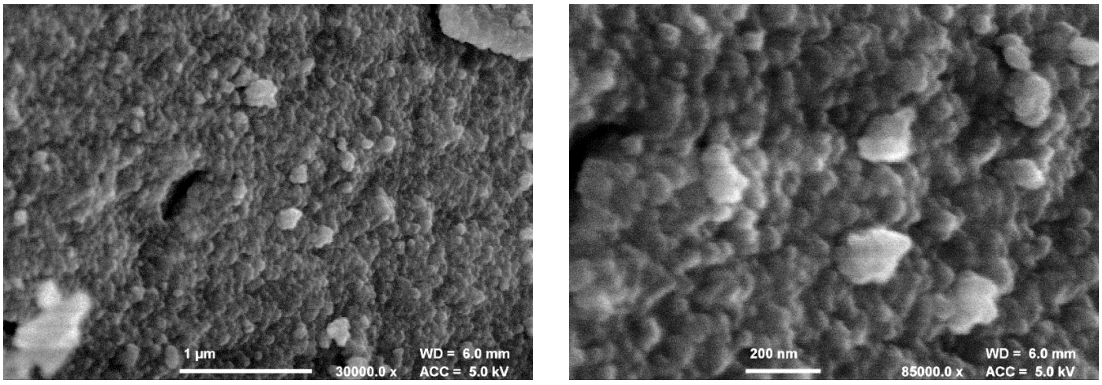

a) b)

Figure 8-2. a) SEM images of the surface of the 2.5% W-TiO_2 sample with scale bar equals 1 micron, b) higher magnification SEM image of the surface of the 2.5% W-TiO_2 sample with scale bar equals 200nm.

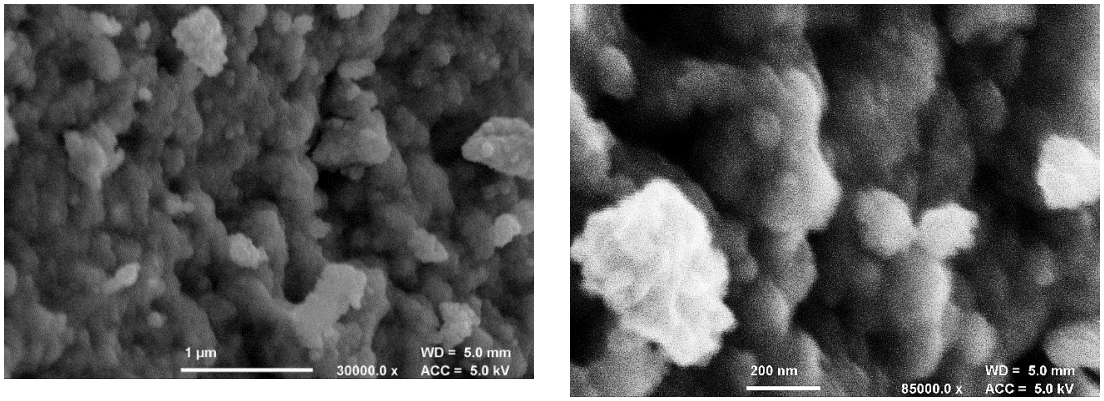

a) b)

Figure 8-3 a) SEM images of the surface of 3% W-TiO_2 sample with scale bar equals 1 micron b) higher magnification SEM image of the surface of 3% W-TiO_2 with scale bar equals 200nm.

Transmission electron microscopy (TEM)

TEM images of the nanoparticles containing 1%, 2.5% and 3% W-TiO_2 are presented in Figure 8-4 to Figure 8-9, respectively, at high magnification. Figure 8-4 shows aggregates and single particles of 1% W-TiO_2 with an average dimension of 14 ± 3 nm measured manually with Image J software. A high magnification image is shown in Figure 8-5. Aggregate particles of 2.5% W-TiO_2 are shown in Figure 8-6 and Figure 8-7. Particle dimensions obtained from Figure 8-6 indicate an average dimension of 10 ± 2 nm. Compared with 1% W-TiO_2 (Figure 8-4) there is more aggregation and atomic lattices are clearly visible in Figure 8-7. Figure 8-8 shows an aggregate of 3% W-TiO_2 with an average particle dimension of 10 ± 2 nm. This is the same as that observed in Figure 8-9. Aggregation was increased in this sample compared with the others which is in accordance with SEM images in Figure 8-3.

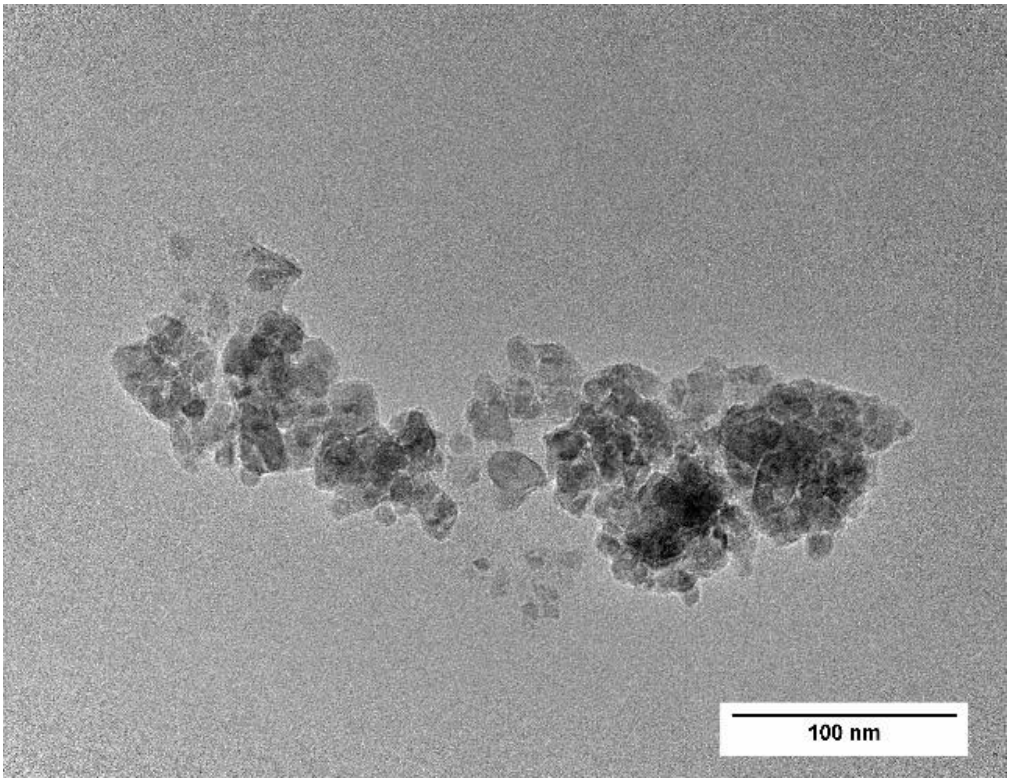

Figure 8-4 TEM image of 1% W-TiO_2 aggregates of nanoparticles.

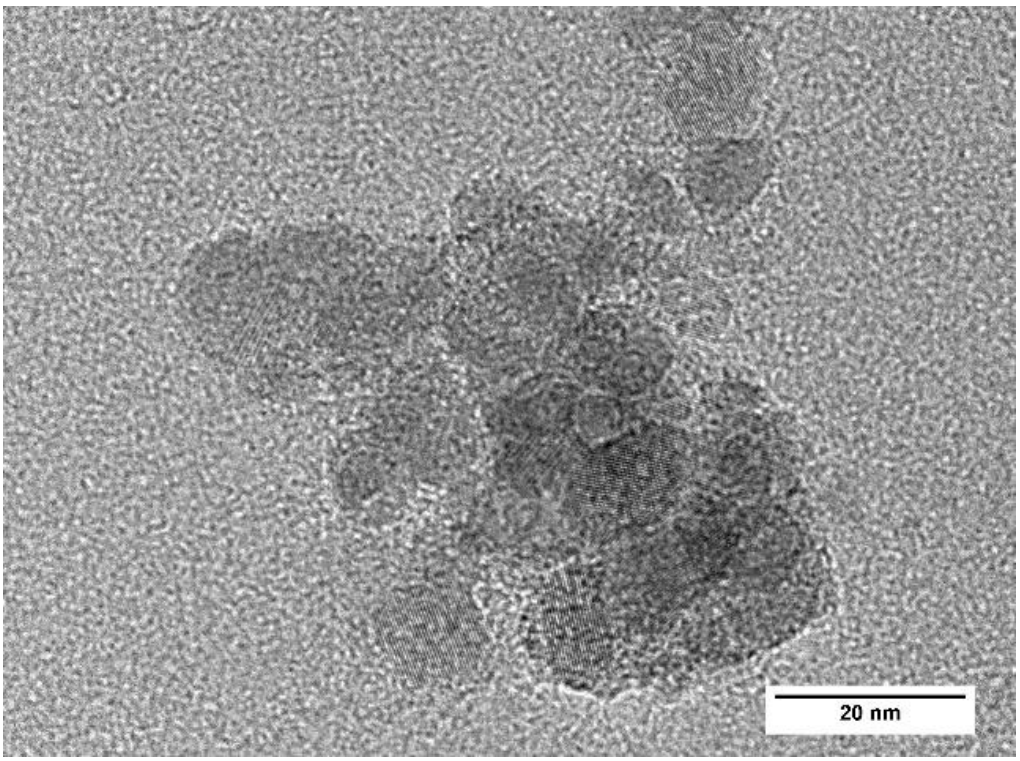

Figure 8-5 TEM high magnification image of a 1% W-TiO_2 aggregate revealing the internal structure of the single nanoparticles.

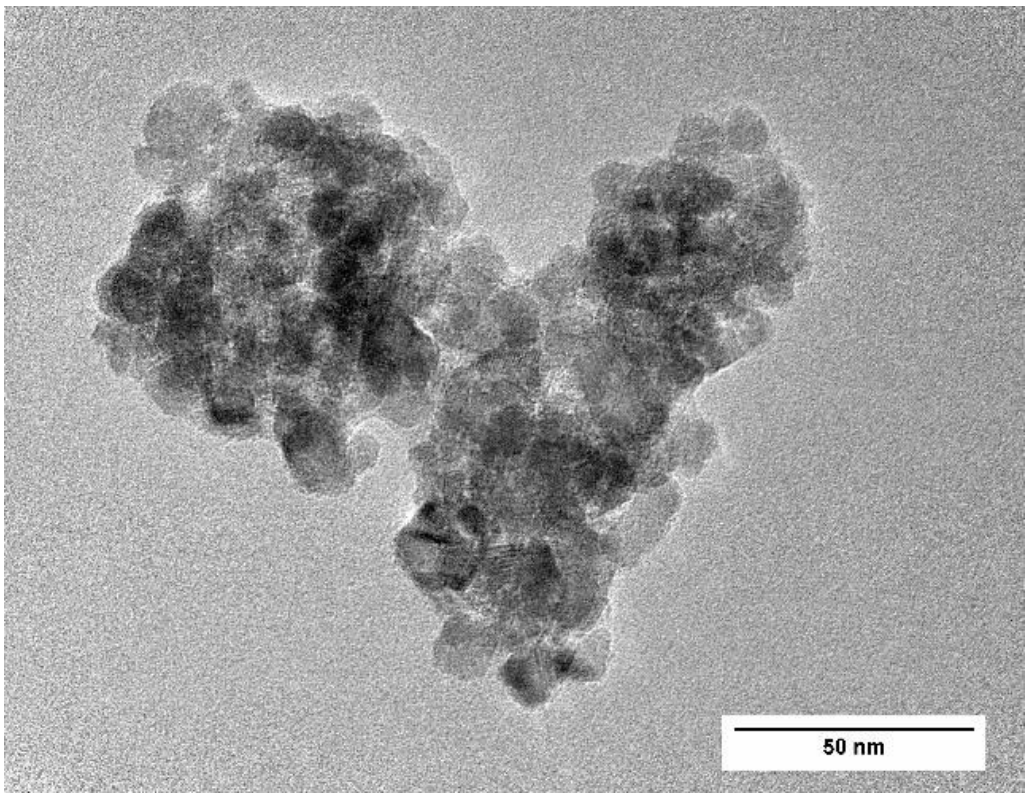

Figure 8-6 TEM images of 2.5% W-TiO_2 aggregates of nanoparticles.

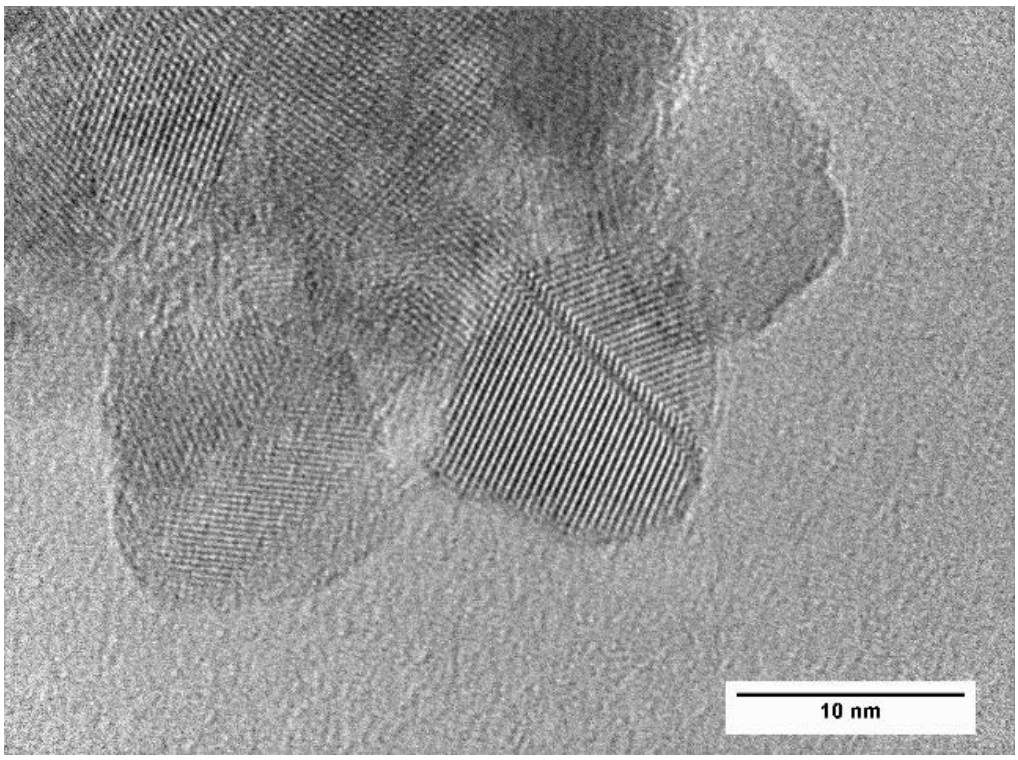

Figure 8-7 TEM high magnification image of a 2.5% W-TiO_2 aggregate revealing the internal structure of the single nanoparticles.

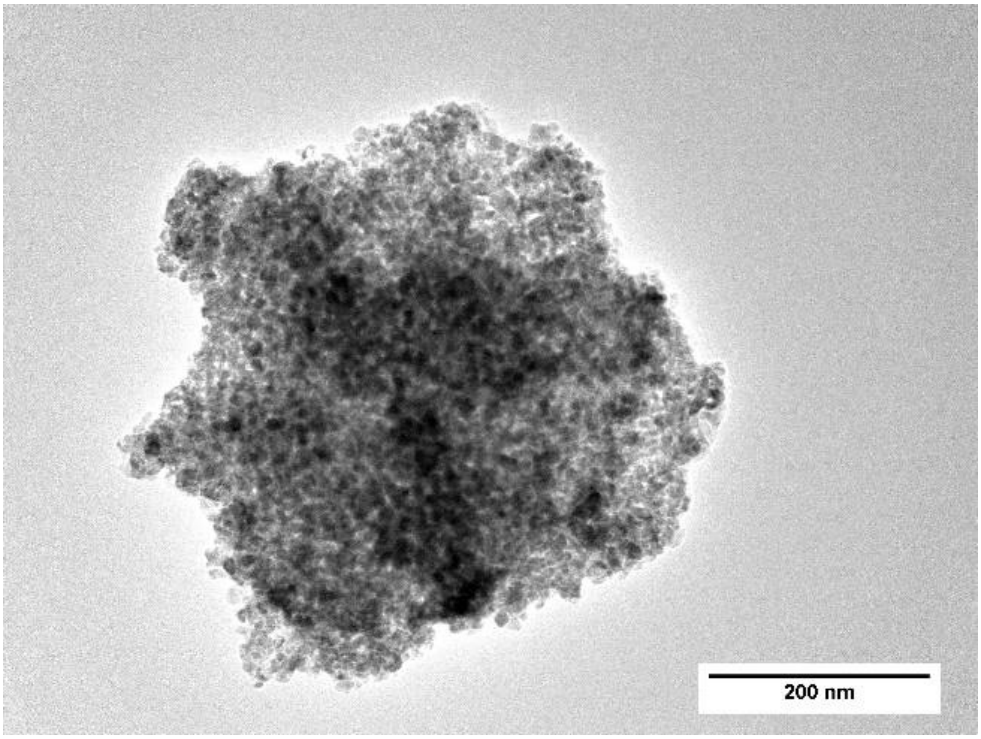

Figure 8-8 TEM high magnification image of a 3% W-TiO_2 aggregate showing the lattice plane of the single nanoparticles.

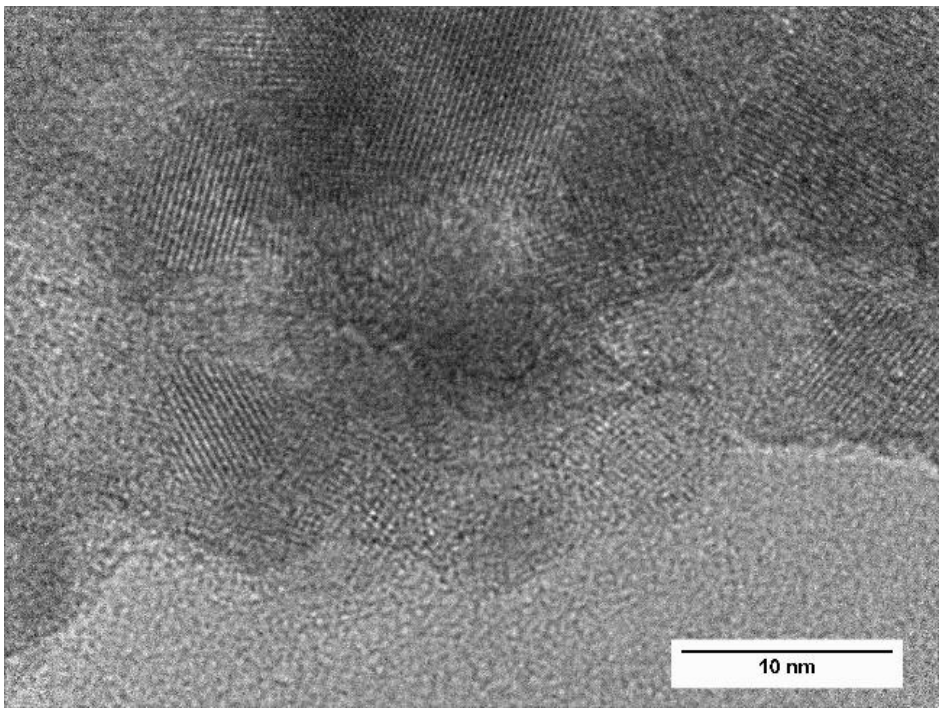

Figure 8-9 TEM high magnification image of a 3% W-TiO_2 aggregate showing the lattice plane of the single nanoparticles.

8.2 XRD analysis

Results of semi-quantitative phase analysis (QPA) are recorded in Table 8-1 Rietveld agreement factors and phase composition of the samples, while a graphical output of a Rietveld refinement is shown in Figure 8-10. As seen in Table 8-1, the unmodified specimen only contains the anatase and brookite TiO_2 polymorphs. Anatase is expected to be present, being the stable TiO_2 polymorph at the nanoscale, because of thermodynamic considerations [24]. On the other hand, the presence of brookite is due to the acidic conditions of the synthesis [166]. The addition of tungsten favoured the formation of the rutile TiO_2 polymorph, mainly at the expense of brookite; it should be noted that the higher the tungsten mol% in the TiO_2, the higher the anatase fraction in the specimen. For example, the specimen with 3 mol% tungsten is composed of 86.7 wt% anatase, 3.1 wt% rutile, and 10.2 wt% brookite. However, in the TiO_2 system, crystallisation and, consequently, the anatase-to-rutile phase transition, is affected by several parameters (the synthesis process, starting materials, atmosphere and the presence of impurities or doping species [174]). Thus, we can fairly assume here that, with this synthesis method and at a moderately low temperature of 450°C, the insertion of tungsten in the anatase-brookite system (*i.e.* the TiO_2 polymorphs present in the unmodified

specimen), favoured the anatase-to-rutile phase transition, although at very low W concentrations.

Table 8-1 Rietveld agreement factors and phase composition of the samples

Sample		**Agreement factors**			**Phase composition (wt%)**		
	No. of variables	$R(F^2)$ **(%)**	R_{wp} **(%)**	χ^2	**anatase**	**rutile**	**brookite**
TiO_2	17	3.61	3.75	1.65	61.3±0.2	–	38.7±0.7
1% W-TiO_2	19	2.46	3.47	1.57	55.0±0.2	17.8±0.2	27.2±0.4
2.5% W-TiO_2	12	2.38	3.20	1.46	77.5±0.1	11.6±0.2	10.9±5
3% W-TiO_2	12	3.63	3.36	1.50	86.7±0.1	3.1±0.2	10.2±0.5

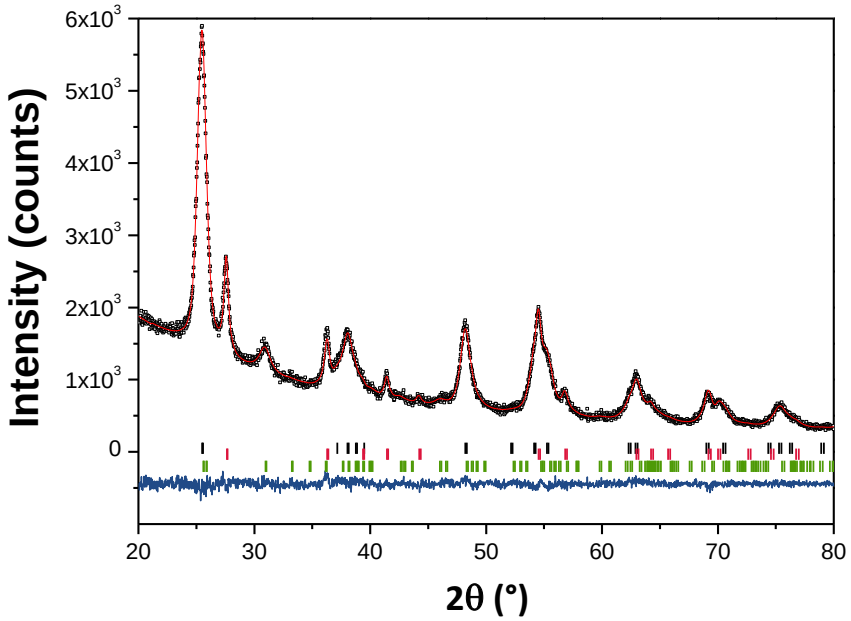

Figure 8-10 Rietveld refinement of XRD data for the sample 1% W-TiO_2. The red continuous line represents the calculated pattern, the black open squares the observed pattern, and the difference curve between observed and calculated profiles is plotted below (blue continuous line). The position of reflections is indicated by the small vertical bars (black: anatase; red: rutile; green, brookite).

Table 8-2 WPPM agreement factors, anatase unit cell parameters and average domain diameters.

Sample	Agreement factors			Anatase unit cell parameters			Average domain diameter (nm)
	R_{wp} (%)	R_{exp} (%)	χ^2	$a=b$ (nm)	c (nm)	V (nm^3)	
TiO_2	6.79	2.45	2.77	0.3783	0.9493	0.136	8.2
1% W-TiO_2	5.34	2.39	2.23	0.3789	0.9511	0.137	11.0
2.5% W-TiO_2	5.60	2.36	2.37	0.3790	0.9500	0.136	8.8
3% W-TiO_2	5.07	2.33	2.17	0.3792	0.9500	0.137	8.3

Results obtained via the WPPM method are listed in Table 8-2. Considering that the presence of tungsten oxides was not detected in the XRD patterns, and looking at the unit cell parameters, the incorporation of W into TiO_2 lattice is likely because the ionic radii of $^{[VI]}W^{4+}$ and $^{[VI]}Ti^{4+}$ are equal to 0.66 and 0.61 Å, respectively [175]. Moreover, the addition of only 1 mol% W gave a higher average crystalline domain diameter for the anatase nanocrystal (*i.e.* 11.0 nm *versus* 8.2 nm in the unmodified sample). This is consistent with the more advanced anatase-to-rutile phase transition in that sample (*cf* Table 1): which is believed to be a nucleation-growth phenomenon [175]. This confirms that for the addition of 1 mol% tungsten, the nucleation and growth of anatase was favoured, and the critical size beyond which the anatase-to-rutile phase transition occurred was achieved faster than with 2.5 and 3 mol% tungsten additions.

8.3 Raman analysis

Raman spectra are presented in Figure 8-11 for P25 commercial TiO_2 and Figure 8-12 the tungsten synthesised particles.

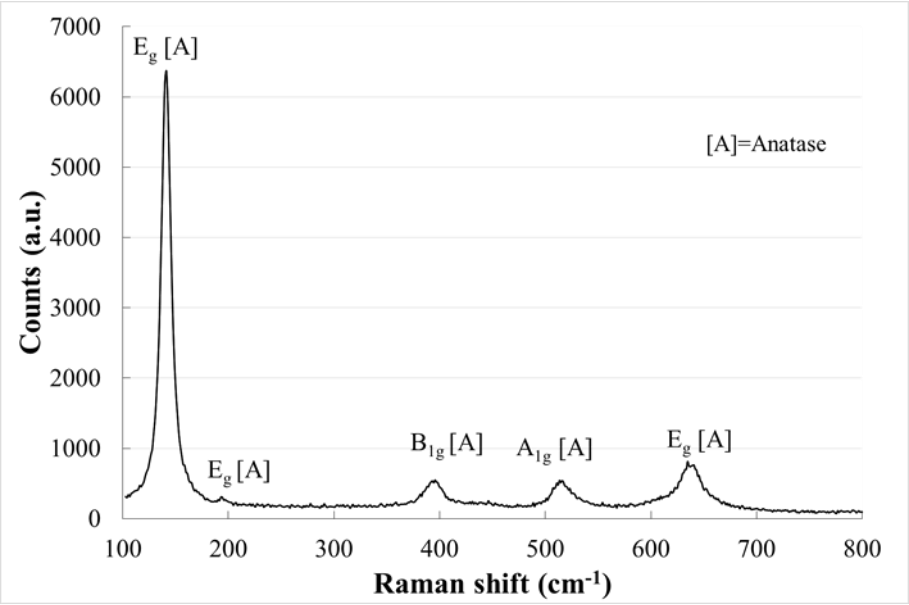

Figure 8-11 Raman spectrum for commercial P25 TiO_2.

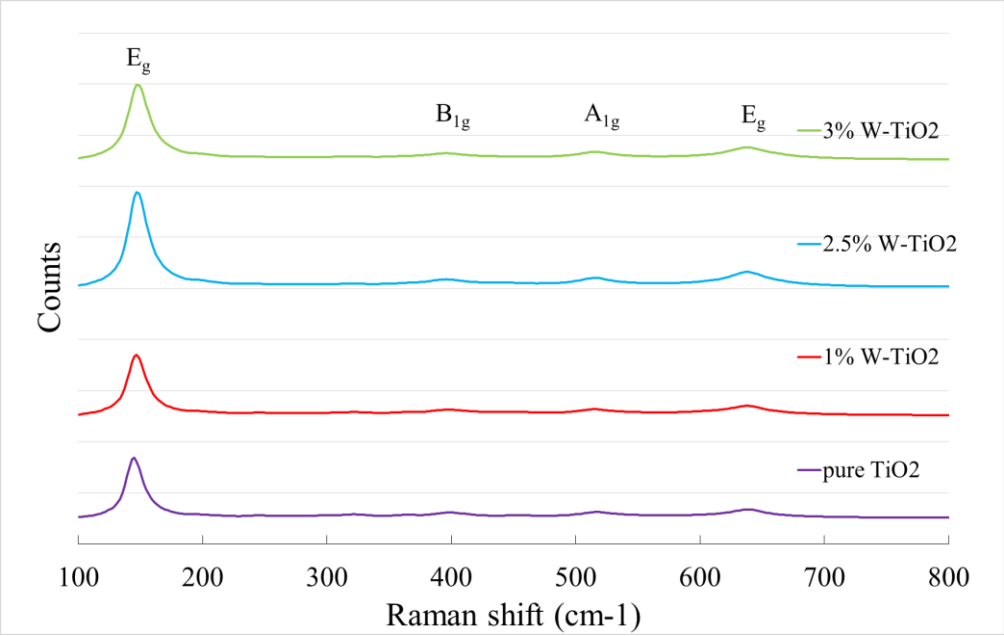

Figure 8-12 Raman spectra for pure TiO_2, 1%, 2.5% and 3% W doped TiO_2.

In all the specimens bands assigned to both the rutile and anatase phases are present. The presence of tungsten and its increasing concentration in the doped samples does not appear to affect the Raman spectra. The main anatase Raman band (E_g around 145 cm^{-1}) of all the synthesised samples was fitted with a Lorentz function and the full width at half maximum (FWHM) and centroid were obtained and reported in Table 8-3. Comparing

the FWHM and the centroid reported it is possible to obtain qualitative information about disorder as stated by Balaji et al [176].

Table 8-3 FWHM and centroid value for W-TiO_2

Sample	FWHM	Centroid position
1% W-TiO_2	17.8 ± 1	147.2
2.5% W-TiO_2	19 ± 1	148.1
3% W-TiO_2	19.9 ± 1	148.5

The Raman shifting of the centroid to higher values and the increase of the FWHM means that the dimension of the anatase is decreasing consistently with XRD results.

8.4 Diffuse reflectance spectroscopy (DRS) and BET surface analysis

Diffuse reflectance spectroscopy (DRS) results are shown in Table 8-4, and Figure 8-13 to Figure 8-15. All the spectra consist of one single absorption edge at around 390 nm, assignable to TiO_2.

The values of the optical E_g of the specimens, obtained from the Tauc plots as reported in chapter 3.4, are listed in Table 8-4. The indirect allowed model (Figure 8-15) fits well to this TiO_2 band structure because the E_g values obtained are consistent with the expected E_g for rutile (*i.e.* 3.0 eV, in agreement with other literature data [170]) . On the contrary, the direct allowed model (Figure 8-14) gave very large E_g values, which is not consistent with the TiO_2 band structure.

The BET surface area, S_{BET}, values in Table 8-4 are notably different for the three levels of tungsten doping suggesting different levels of agglomeration and perhaps particle size variation.

Table 8-4 Optical band gap and BET surface area of commercial and synthesised samples.

Sample	**Optical Eg (eV)**		**S_{BET} (m^2 g^{-1})**
	Direct allowed	Indirect allowed	
P25	3.68 [177]	3.26 [177]	79.6
1% W-TiO_2	3.29	2.96	68.9
2.5% W-TiO_2	3.39	3.03	110.9
3% W-TiO_2	3.33	2.99	99.0

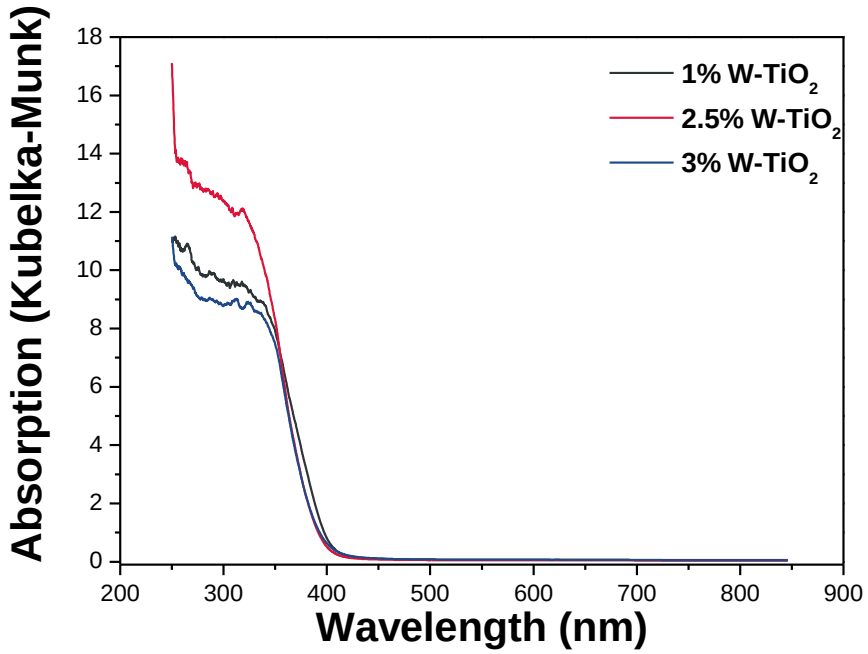

Figure 8-13 Diffuse reflectance spectroscopy (DRS) of the W-TiO_2 specimens.

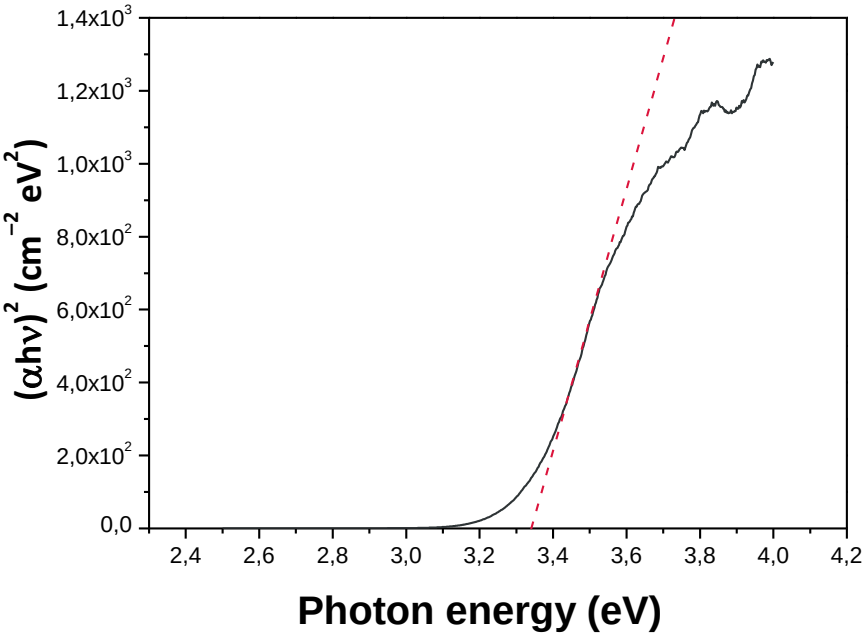

Figure 8-14 Kubelka–Munk elaboration versus photon energy (Tauc plot) according to the DIRECT E_g model on 1% W-TiO_2. The dashed red line represents the x-axis intercept of the line that is tangential to the inflexion point of the curve.

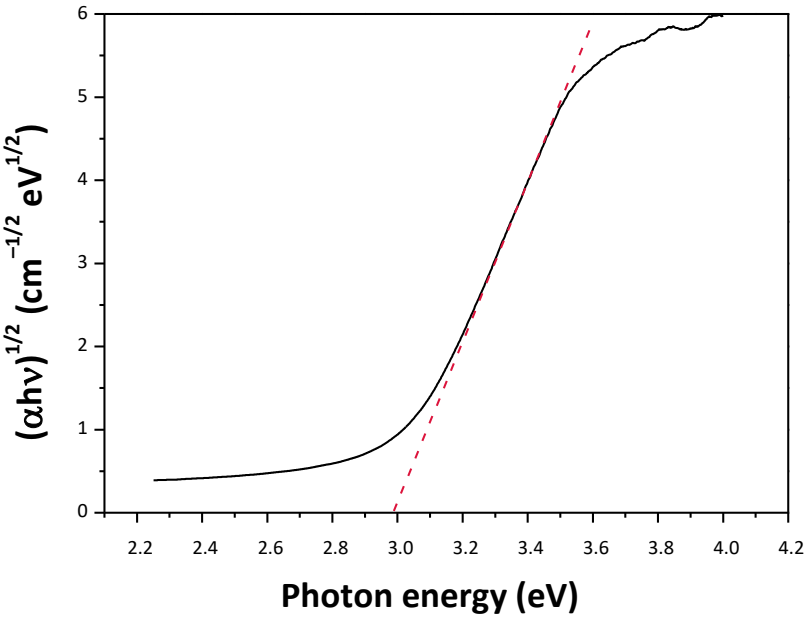

Figure 8-15 Kubelka–Munk elaboration versus photon energy (Tauc plot) according to the INDIRECT E_g model on 1% W-TiO_2. The dashed red line represents the x-axis intercept of the line that is tangential to the inflexion point of the curve.

8.5 Methylene Blue degradation test

The concentration of methylene blue versus the time of irradiation is presented in Figure 8-16 for UV light and Figure 8-17 for white LED light for commercially available P25 TiO_2 and 1, 2.5 and 3% tungsten doped TiO_2.

Photocatalytic degradation of methylene blue under UV irradiation (Figure 8-16) by the TiO_2 nanoparticles shows the expected reduction in normalised concentration shown as a downward trend. All the synthesised tungsten doped TiO_2 particles degrade MB by 10 to 20% more than the commercially available particles in the UV range.

The degradation experiment was continued by irradiating with white LED visible light commonly used indoors (Figure 8-17) and demonstrates that the amount of dye removed under UV light was greater in specimens where the anatase phase was more predominant, such as 3% as shown in Table 8-1.

All W-doped samples are superior to the commercial P25 particles so the application of W-doped based coatings inside buildings is expected to further improve IAQ.

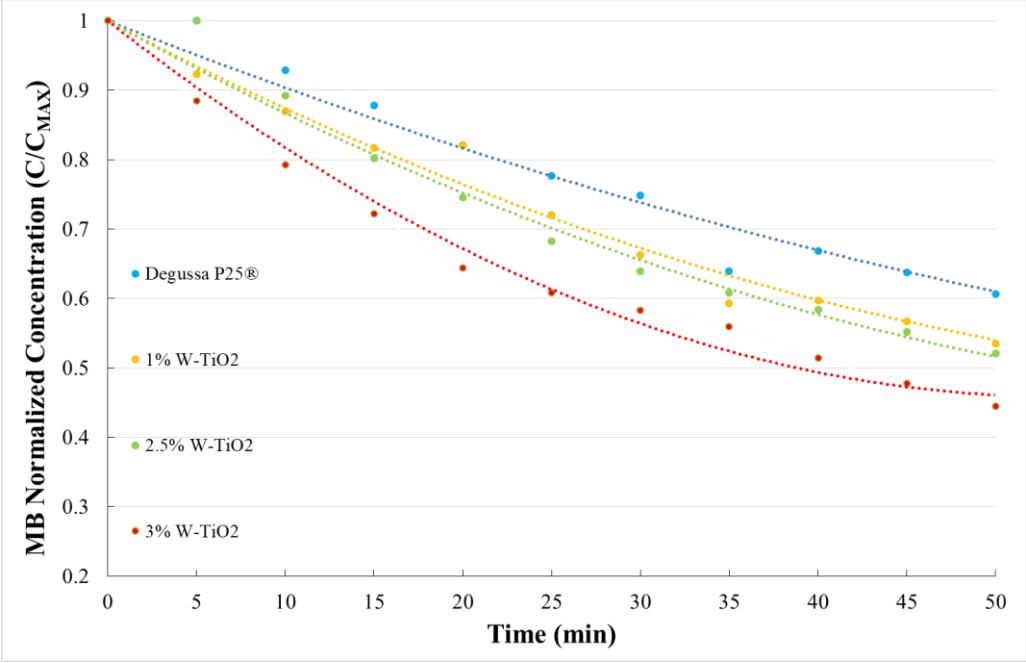

Figure 8-16 Methylene blued degradation tests of all the particles irradiated by UV light.

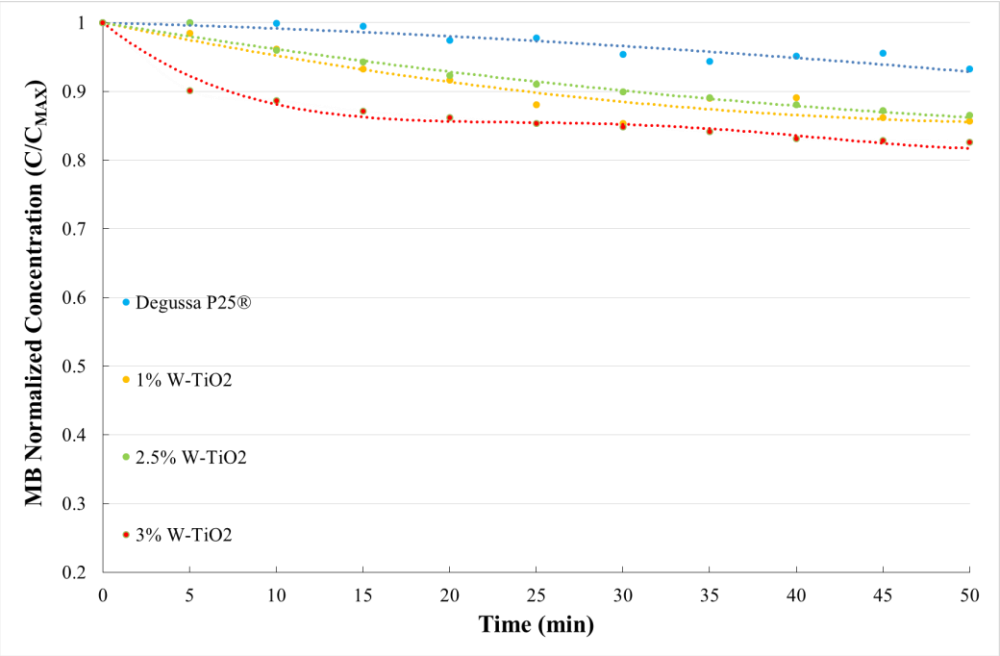

Figure 8-17 Methylene blued degradation tests of all the particles irradiated by white LED light.

8.6 NO_x degradation test

The conversion rate (%) of the initial NO_x concentration was plotted in Figure 8-18, the data plotted are an average over three consecutive recycling tests.

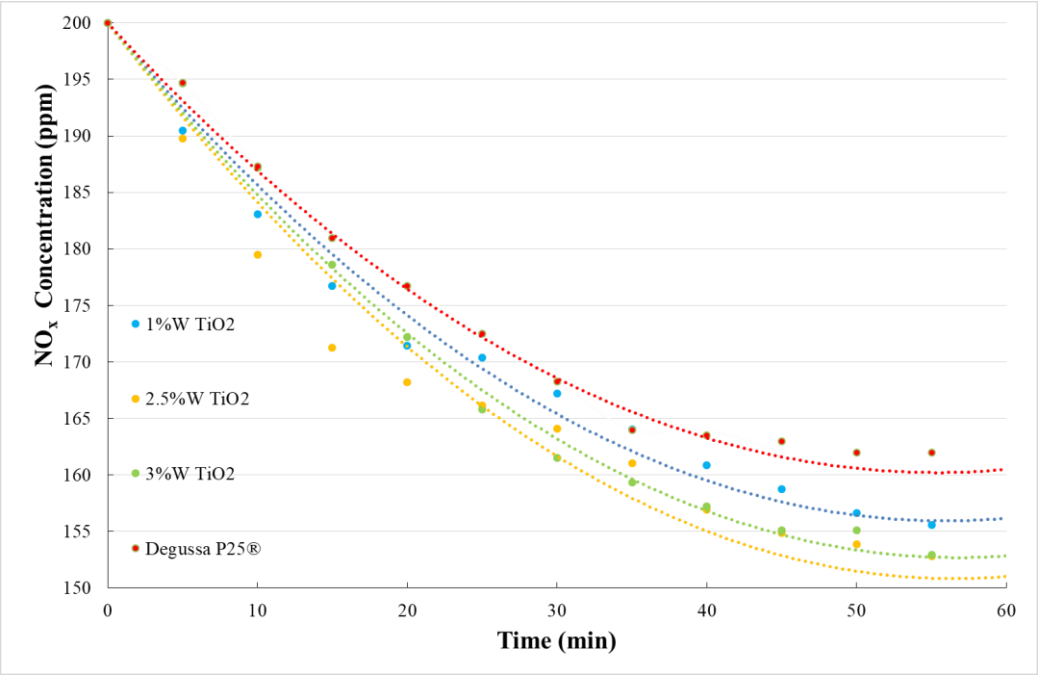

Figure 8-18 Decomposition of NOx by PC reaction of the nanoparticles irradiated with an Osram Solar lamp, dotted lines are generated with a polynomial fit.

All the trends in the reduction of NO_x concentration by photocatalytic activity for the four particles studied are similar but all the W-doped synthesised particles are circa 10% more effective than commercially available P25 making them suitable for application in an indoor environment. As seen in Figure 8-18, following an initial degradation, the pollutant concentration reached a plateau, and the samples could no longer continue decomposing nitrogen oxides which are particularly noticeable for P25. This deactivating behaviour of TiO_2 is well-known to be caused by the oxidation of NO_2 to HNO_3 [172]. The O_2^- and $OH^{\bullet}$ radicals formed during photocatalysis react with the pollutant gas, producing NO_2 and HNO_3. However, the HNO_3 formed is easily eluted into water [173].

To better compare the tested specimens, the experimental data of the first 20 minutes of NO_x degradation was further analysed according to a first-order kinetic law, so as to obtain the pseudo-first-order apparent rate constant (k'_{app}). Results are listed in Table 8-5.

Table 8-5 Initial (20 min) pseudo-first order kinetic constants, and relative correlation coefficients for the tested samples, for NO_x degradation in gas–solid phase, using the OSRAM solar lamp.

Sample	$k_{20} \times 10^3$ **(min^{-1})**	R^2
P25	6.36±0.14	0.997
1% W-TiO$_2$	8.08±0.25	0.995
2.5% W-TiO$_2$	9.51±0.46	0.988
3% W-TiO$_2$	7.32±0.23	0.995

The pseudo-first order kinetic constants of the initial first 20 min of reaction confirmed that the W-TiO_2 specimens are more photocatalytically active than the commercial sample P25. Among the W-TiO_2 samples, the 2.5% W-TiO_2 sample is the one showing higher activity, so this is the optimum doping level for this series. A possible explanation might be the reduced dimension of anatase crystalline domains (*i.e.* 8.8 nm, see Table 8-2), and their greater specific surface area, *i.e.* 110.9 $m^2\ g^{-1}$, Table 8-4.

8.7 Conclusions

The following conclusions can be drawn from this chapter:

- Sol-gel synthesis was successfully used to produce TiO_2 nanoparticles aggregates with various levels of tungsten doping in the crystal lattice.

- The proportion of anatase in the material increased with the increasing concentration of tungsten as shown from Rietveld agreement factors. Moreover, the Raman shifting of the centroid to higher values and the increase of the FWHM indicates the decreasing dimension of the anatase crystalline domains, which is in agreement with the XRD data.

- Methylene blue degradation under UV light of W TiO_2 and commercial particles confirms that tungsten doped samples are all more photocatalytically effective than P25 with 20% more methylene blue degraded in the case of the 3% W-TiO_2 sample.

- Degradation tests under visible light demonstrate that tungsten doped particles degraded circa 10% more methylene blue than the reference P25 material, supporting their use in visible light active PC coatings.

- NO_x degradation tests show that synthesised and commercial particles exhibit a similar trend to the methylene blue results with respect to the percentage of NO_x removed over the same time period when irradiated with visible light from an Osram bulb.

9 Graphene/TiO_2 hybrids and pure TiO_2

This chapter presents the characterization and analysis of sol-gel synthesised hybrid graphene/TiO_2 nanoparticle composites manufactured following two protocols. Data obtained from XRD, UV-Visible diffusive spectroscopy, Raman spectroscopy, He-beam microscopy, FESEM and TEM are presented. Comparisons are made between the composites and commercially available TiO_2 particles and pure sol-gel TiO_2. The photocatalytic performance was studied in the aqueous as well as gas phase, as previously described in Chapters 4, 5 and 6.

9.1 SEM, He beam microscopy and TEM

Images from SEM, Helium beam microscopy and TEM were acquired to investigate the micro and nanostructures of the nanoparticles and agglomerates.

Pure TiO_2

Pure TiO_2 aggregates have a rough surface as shown in Figure 9-1 a) and b) and consist of nanoparticles around 20 nm ± 5 nm in diameter measured using ImageJ. Nanoparticles were all aggregated and evenly distributed on the surface of the pure sample.

Higher magnification TEM images confirm that aggregation is present also in the smaller sized aggregates as shown in Figure 9-2 a). Pure TiO_2 nanoparticles do not present any preferred lattice direction as shown in Figure 9-2 b).

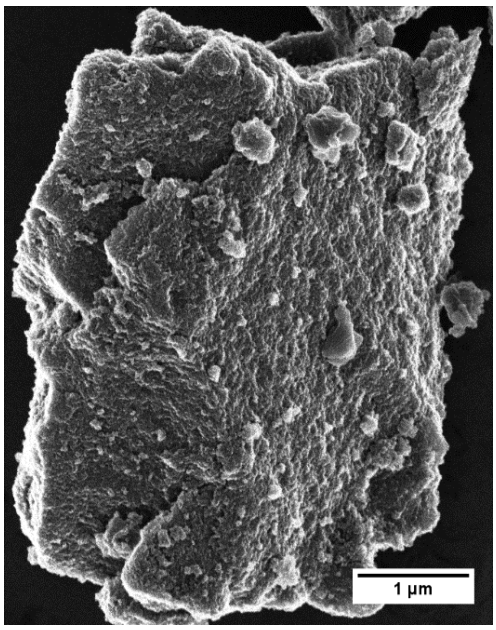

a)

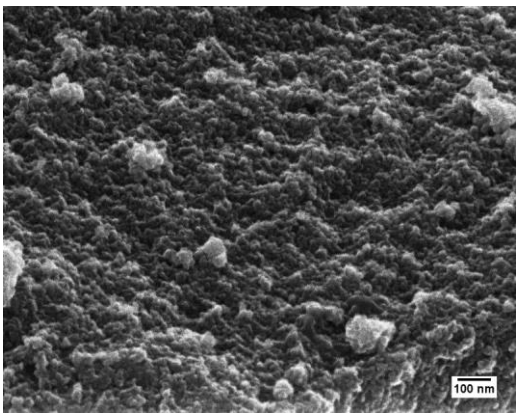

b)

Figure 9-1 a) He beam image of aggregate of pure TiO_2 nanoparticles, b) He beam image close up of the rough surface of pure TiO_2 with scale bar=100nm.

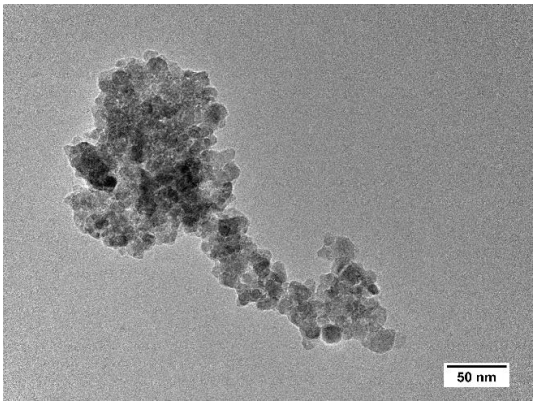

a)

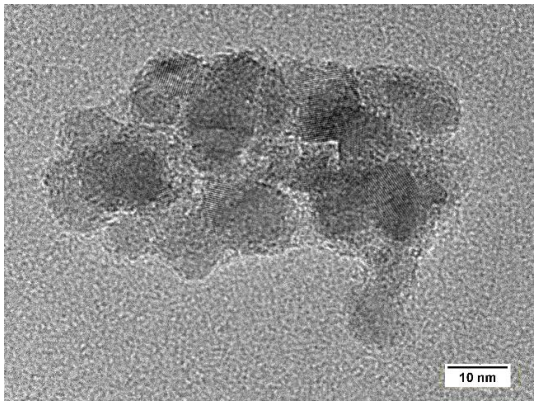

b)

Figure 9-2 a) TEM image of aggregate of TiO_2 nanoparticles in pure TiO_2 b) high magnification TEM picture of the surface of a small aggregate of pure TiO_2 nanoparticles.

Graphene/TiO_2 sol-gel sample ($GTiO_2S$)

The presence of Graphene in specimen $GTiO_2S$ appears to have modified the nucleation and growth of TiO_2 aggregates as shown in Figure 9-3 a). The surface becomes rougher

as shown in Figure 9-3 b) compared to pure TiO_2. The dimension of the particles measured in post processing does not change significantly when compared with pure TiO_2 in Figure 9-1 b). Figure 9-4 a) shows how graphene sheets behave as a nucleation point for the TiO_2. Figure 9-4 b) focuses on the interface between the graphene sheet and the TiO_2 nanoparticles.

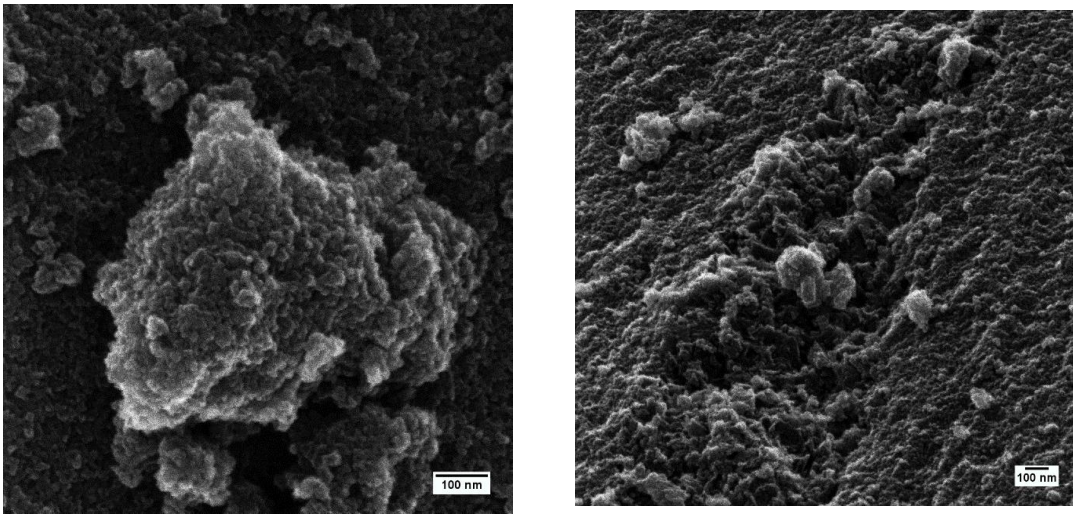

a) b)

Figure 9-3 a) He beam image of $GTiO_2S$ surface, b) He beam image close up of the rough surface of the $GTiO_2S$**.**

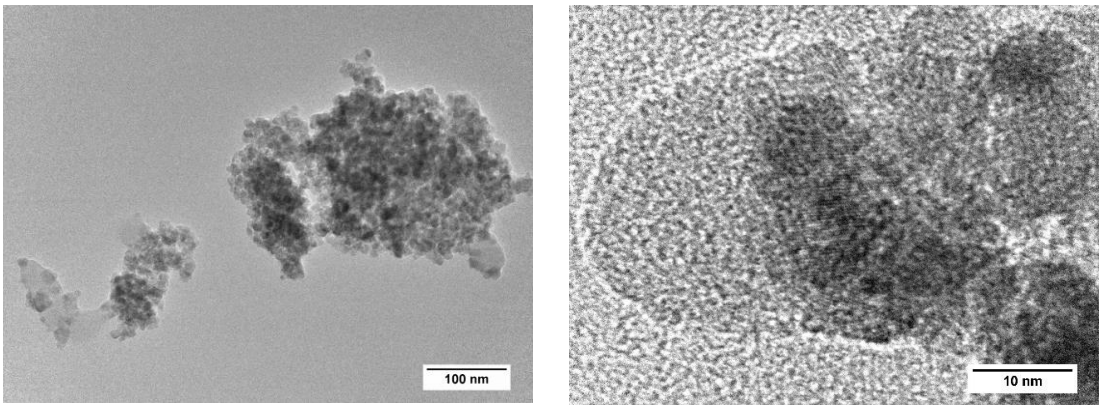

a) b)

Figure 9-4 a) TEM image of TiO_2 nanoparticle aggregates anchored to Graphene sheets decorated within the $GTiO_2S$ particle b) high magnification TEM picture of the interface of atomic planes of TiO_2/Graphene within the $GTiO_2S$ particle.

Graphene/TiO_2 mixed sample ($GTiO_2M$)

Figure 9-5 a) and b) show the intricate network of TiO_2 and graphene in the $GTiO_2M$ sample that was not observed in the $GTiO_2S$ sample. The presence of graphene modified the shape and the roughness of the specimen surface showing that graphene and TiO_2 are deeply embedded together. TEM images were in agreement with those obtained by He beam microscopy, Figure 9-6 a) highlights the intricate network of graphene and TiO_2 that is produced through the mixing of the two components in alcoholic solution. Figure 9-6 b) shows the interface between TiO_2, where atomic lattice plains are visible, and graphene, where atomic planes are visible.

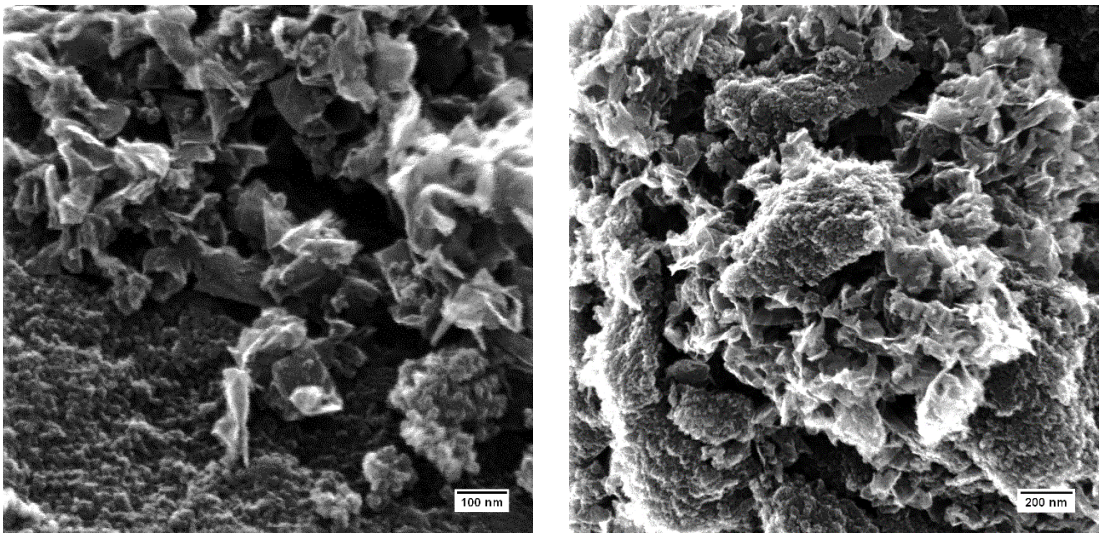

a) b)

Figure 9-5 a) Graphene sheets and TiO_2 nanoparticles in $GTiO_2M$ b) mixture of graphene and TiO_2 in $GTiO_2M$.

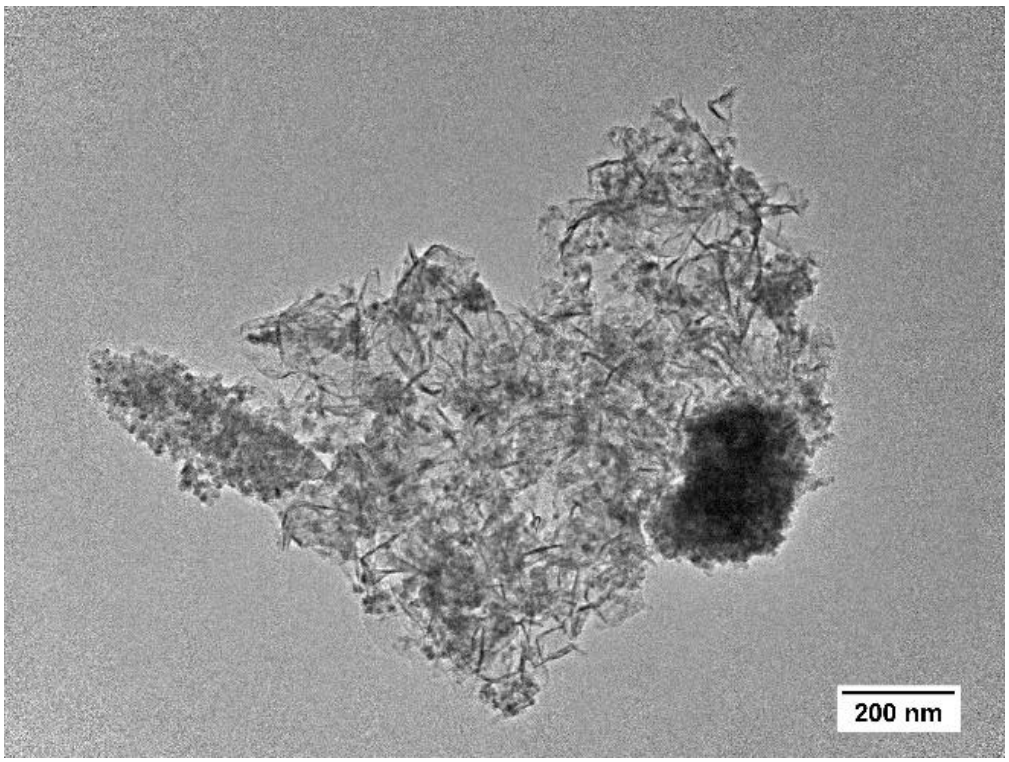

a)

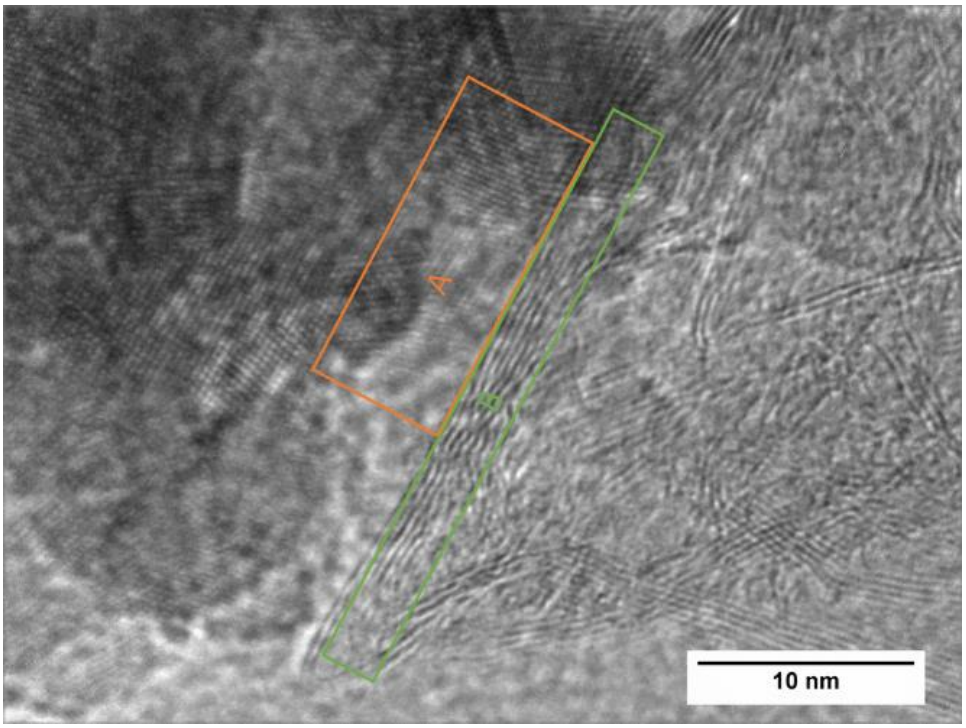

b)

Figure 9-6 a) TEM image of graphene sheets decorated with TiO_2 nanoparticles in $GTiO_2M$ b) high magnification TEM picture of the interface of atomic plans of TiO_2 shown in the A box and Graphene planes shown in B box in $GTiO_2M$ particle.

9.2 XRD and Rietveld refinement

XRD patterns of the samples are reported in Figure 9-7, while an example of the Rietveld refinement is depicted in Figure 9-8. The agreement factors of the Rietveld refinements are reported in Table 9-1 in addition to the semi-quantitative phase analyses (QPA). In these analyses, only the crystalline TiO_2 polymorphs were considered

The sol-gel synthesis of the unmodified TiO_2 specimen led to the formation of anatase (64.1 wt%), and brookite (35.9 wt%) TiO_2 polymorphs. This is in agreement with previous research as anatase is the thermodynamically stable TiO_2 polymorph at the nanoscale [166]; also, brookite formation can be attributed to the acidic conditions of the synthesis [178]. The specimen $GTiO_2M$, quite obviously, had virtually the same mineralogical composition as the unmodified TiO_2, *cf* Table 9-1. On the other hand, the specimen $GTiO_2S$ had slightly less anatase, 57.6 wt%, in favour of a higher amount of brookite, *i.e.* 42.4 wt%. This is believed to be due to increased acidity related to the graphene addition to the reacting system [179]..

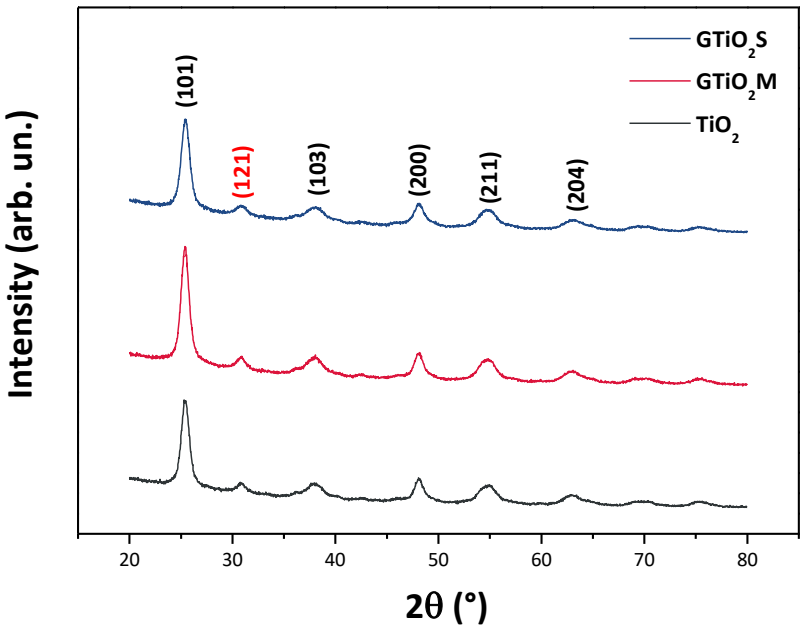

Figure 9-7 XRD patterns of $GTiO_2S$, $GTiO_2M$ and TiO_2.Miller indices in black belong to anatase reflections; that in red belongs to brookite.

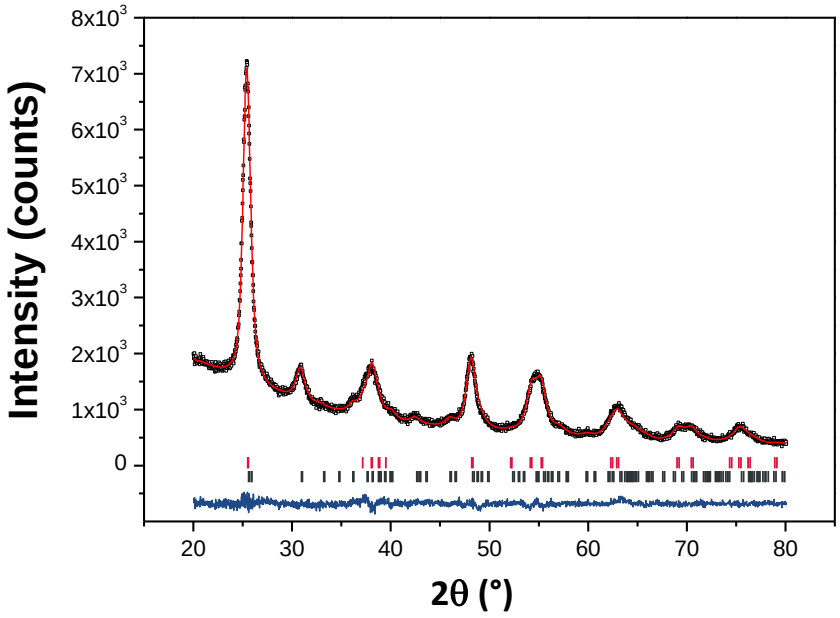

Figure 9-8 Graphic Rietveld refinement of the $GTiO_2M$ specimen. The continuous red line represents the calculated pattern, the black open squares represent the observed pattern, and the difference curve between observed and calculated profiles is plotted below as a continuous blue line. The position of reflections is indicated by the small vertical bars (red: anatase; black: brookite).

Table 9-1 Rietveld agreement factors and crystalline phase composition of the prepared specimens

Sample	**No. of variables**	**Agreement factors**			**Phase composition (wt%)**	
		R (F^2) (%)	R_{wp} (%)	χ^2	anatase	brookite
TiO_2	18	3.60	4.33	1.87	64.1	35.9
$GTiO_2S$	18	2.68	3.66	1.65	57.6	42.4
$GTiO_2M$	18	2.81	3.53	1.65	63.7	36.3

Microstructural information in the form of the size and size distribution of anatase and brookite nanoparticles in the specimens was determined using X-ray methods. A WPPM

(Whole Powder Pattern Modelling) graphical output of the specimen $GTiO_2M$ is shown in Figure 9-9. Quantitative figures are reported in Table 9-2 Table 9-3, and Figure 9-10 Figure 9-11.

Anatase unit cell parameters of TiO_2 and $GTiO_2M$ are virtually the same, as shown in Table 9-2; the change in the synthesis method (specimen $GTiO_2S$), led to a slight expansion of the anatase *c*-axis, although the unit cell volume is the same in all the three synthesised samples. As per the brookite unit cell parameters, these are, once again, virtually the same, within experimental error, for specimens TiO_2 and $GTiO_2M$. Addition and mixing of graphene into the sol also led, in this case, to a slight expansion of the brookite unit cell volume.

Similar observations can be made considering the average diameter of the anatase crystalline domains in specimens TiO_2 and $GTiO_2M$. They are virtually the same, within the experimental error, being 6.4 and 7.0 nm, respectively, see Table 9-3 and Figure 9-10. Similarly to observations for the unit cell parameters, $GTiO_2S$ had a bigger average diameter of 8.9 nm.

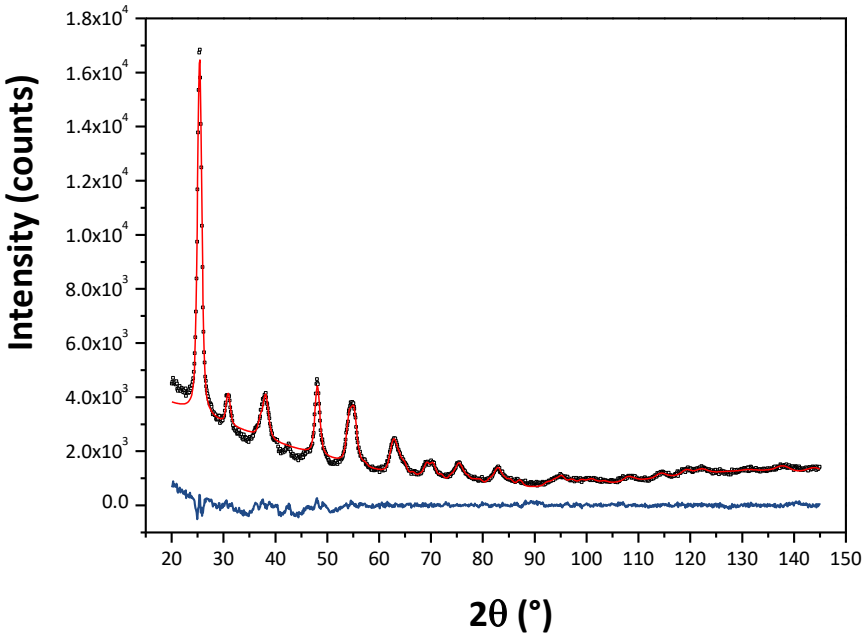

Figure 9-9 Graphical output of the WPPM modelling of $GTiO_2M$ (black open squares are observed data, red continuous line the calculated data, and the lower blue continuous line is the difference curve between observed and calculated profiles).

Table 9-2 WPPM agreement factors and unit cell parameters for the anatase and brookite phases in the synthesised samples

Sample	Agreement factors			Unit cell parameters						
				Anatase			Brookite			
	R_{wp} (%)	R_{exp} (%)	χ^2	*a=b* (nm)	*c* (nm)	V (nm^3)	*a* (nm)	*b* (nm)	c (nm)	V (nm^3)
TiO_2	6.29	2.45	2.57	0.378	0.946	0.136	0.550	0.911	0.513	0.258
$GTiO_2S$	6.05	2.48	2.43	0.378	0.949	0.136	0.554	0.916	0.514	0.262
$GTiO_2M$	6.32	2.36	2.68	0.378	0.947	0.136	0.552	0.910	0.514	0.259

Table 9-3 Mean crystalline domain size of anatase (ant) and brookite (brk) – defined as the mean of the lognormal size distributions; maximum values, and skewness of the lognormal size distributions.

Sample	Mean crystalline domain diameter		Mode of the size distribution		Skewness of the size distribution	
	$\langle D_{ant} \rangle$ (nm)	$\langle D_{brk} \rangle$ (nm)	Ant (nm)	Brk (nm)	Ant (nm)	Brk (nm)
TiO_2	6.4±0.2	7.2±0.4	5.2±0.2	6.4±0.3	1.2±0.1	0.9±0.1
$GTiO_2S$	8.9±0.5	6.2±0.2	7.8±0.5	5.7±0.2	0.9±0.1	0.8±0.1
$GTiO_2M$	7.0±0.5	8.8±0.3	6.1±0.5	8.0±0.2	0.9±0.1	0.8±0.1

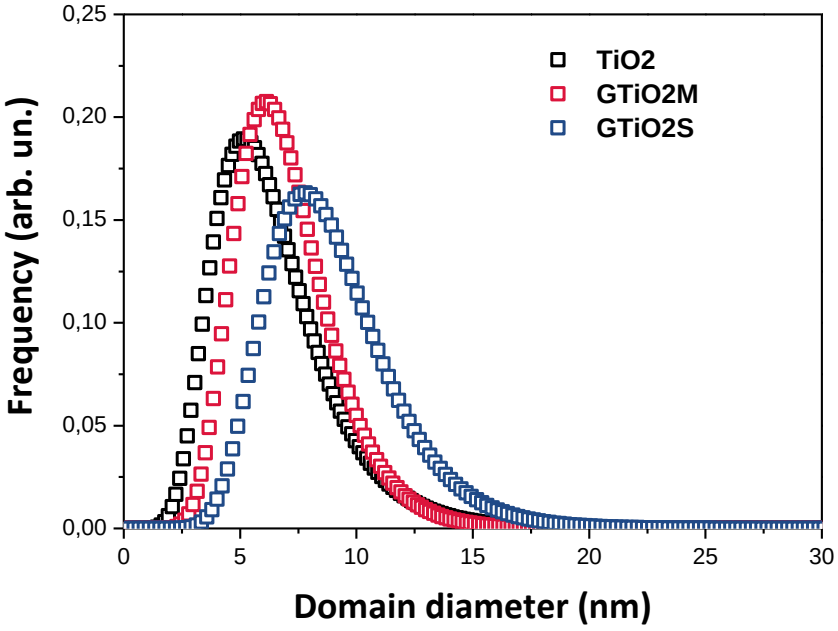

Figure 9-10 Crystalline domain size distribution for anatase in the synthesised specimens.

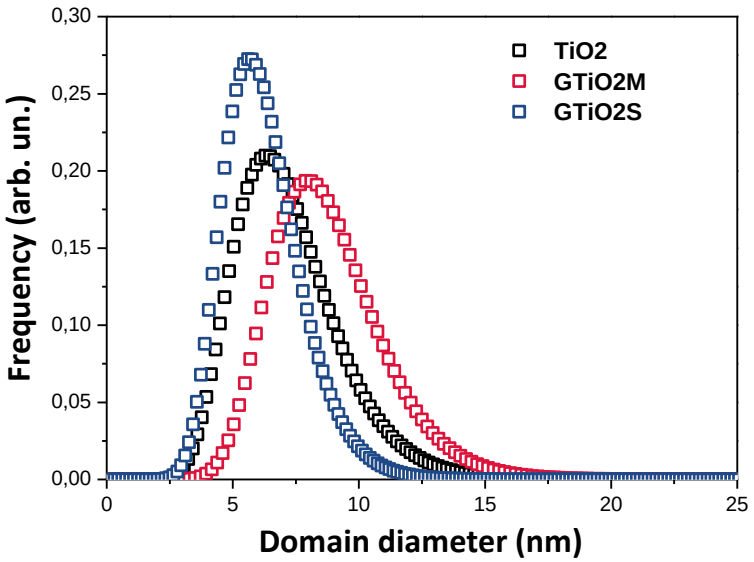

Figure 9-11 Crystalline domain size distribution for brookite in the synthesised specimens.

As per the brookite in the specimens, we cannot infer any particular trend, the average diameter of the crystalline domains being 7.2, 8.8, and 6.2 nm for the TiO_2, $GTiO_2M$, and

$GTiO_2S$ respectively. In addition, all the size distribution had a positive skewness, as shown in, Figure 9-11 and Table 9-3.

9.3 Diffuse Reflectance Spectroscopy (DSR) and BET surface area measurements

DRS spectra are depicted in Figure 9-12. All the spectra consisted of one single absorption edge, located at around 380 nm, assigned to TiO_2 [181]. The apparent optical band gap E_g of the specimens was calculated by means of the Tauc plot, assuming both a direct allowed and indirect allowed transitions – values listed in Table 9-4. The E_g values obtained assuming a direct allowed transition (*cf* Figure 9-13) agree well with the expected E_g of anatase (*i.e.* ~3.2 eV; ~388 nm) reported in the literature [182]. Thus the direct allowed model would seem more applicable for these specimens. Although anatase is commonly reported to be a semiconductor having an indirect allowed transition [183, 184], it has been shown by Serpone et al. that, for indirect band gap semiconductors, as anatase indeed is, a direct transition might appear, when in a colloidal nanomaterial form [185]. Furthermore, the presence of graphene did not change the apparent optical E_g, whereas an increase in the BET specific surface area of the samples was noted, as reported in Table 9-4 (3rd column).

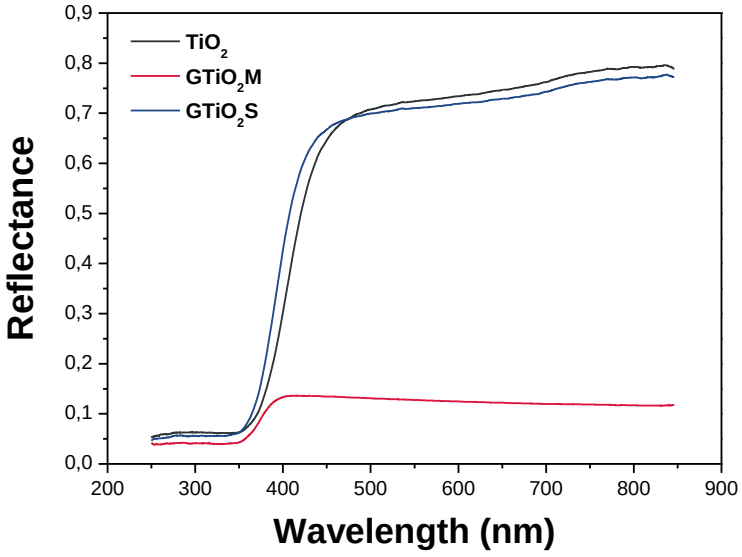

Figure 9-12 DRS spectra of the synthesised samples.

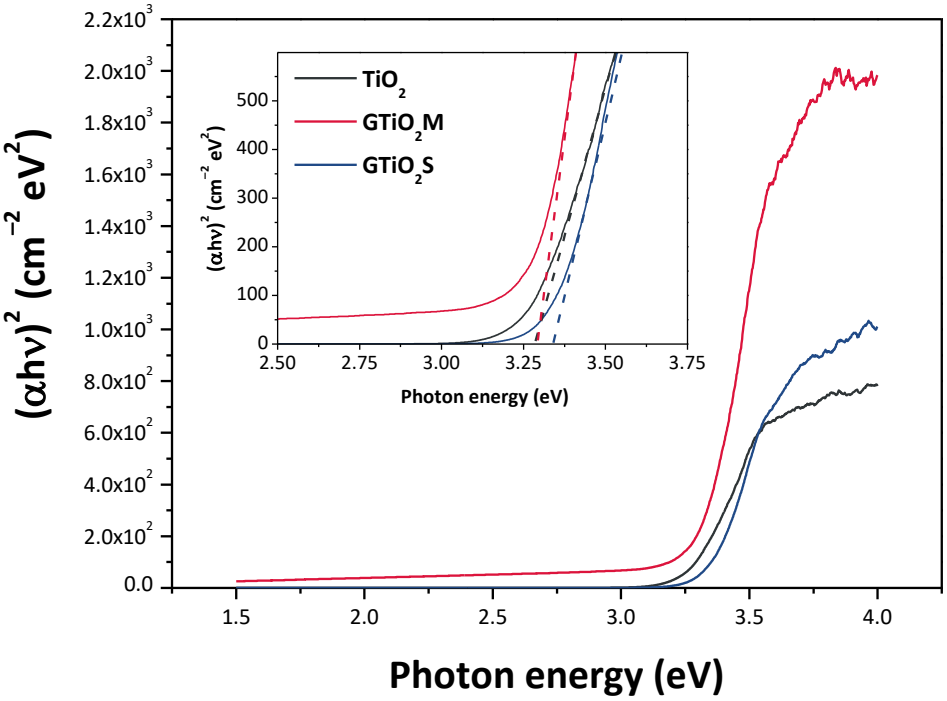

Figure 9-13 Kubelka–Munk analysis of the DRS data versus photon energy (Tauc plot) of the specimens to establish the optical E_g, calculated using the Tauc procedure. Inset: the dotted lines represent the *x*-axis intercept of the line tangent to the inflection point of the sample, *i.e.* the optical E_g according to the direct allowed E_g model – $(\alpha h\nu)^2$, γ = ½.

Table 9-4 Optical energy gap in eV calculated for DRS spectra using Tauc method and BET specific surface area of all the specimens.

Sample	Optical Eg (eV)		S_{BET} (m^2 g^{-1})
	Direct allowed	Indirect allowed	
TiO_2	3.31	2.95	79.6
$GTiO_2M$	3.31	2.96	87.9
$GTiO_2S$	3.35	3.06	100.3

Energy gaps measured were consistent with the amount of anatase in the samples. The presence of graphene did not change the energy gap whereas an increase the surface area of the samples was observed.

9.4 Raman spectra

Raman spectra were obtained to determine the crystalline phase of TiO_2 and allow a comparison with commercial particles, the results are compared with the literature

Figure 9-14 a) Raman spectrum of pure TiO2, b) Raman spectrum of Degussa P25. All three common polymorphs were identified in spectrum (a) corresponding to the pure synthesised TiO_2. The presence of crystalline anatase is indicated by the presence of characteristic bands at 145, 197, 399, 516 and 640 cm^{-1} as well in the commercial particles. Figure 9-14 shows that in the synthesised particles the presence of additional bands at 244 and 330 cm^{-1} are attributed to the rutile form and bands at 250 and 322 cm^{-1} are assigned to the brookite form.

Raman spectra of the hybrid samples containing Graphene are reported in Figure 9-15 a) and b). Both spectra contain the same bands found in the pure synthesised sample attributed to anatase, brookite and rutile. The two major bands assigned to graphene are both present in the samples but at different intensities and this could be due to partial degradation of graphene during the thermal treatment at the end of the synthesis process.

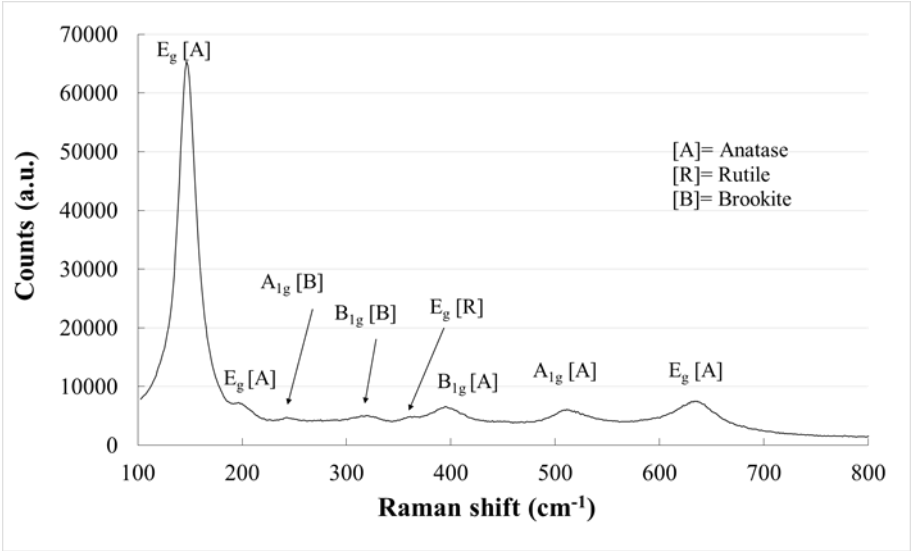

a)

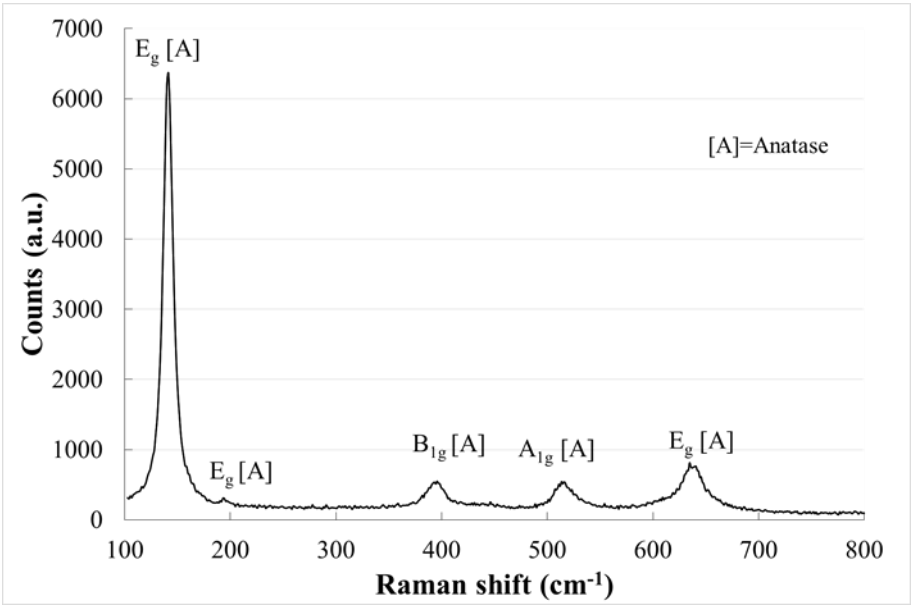

b)

Figure 9-14 a) Raman spectrum of pure TiO_2, b) Raman spectrum of Degussa P25.

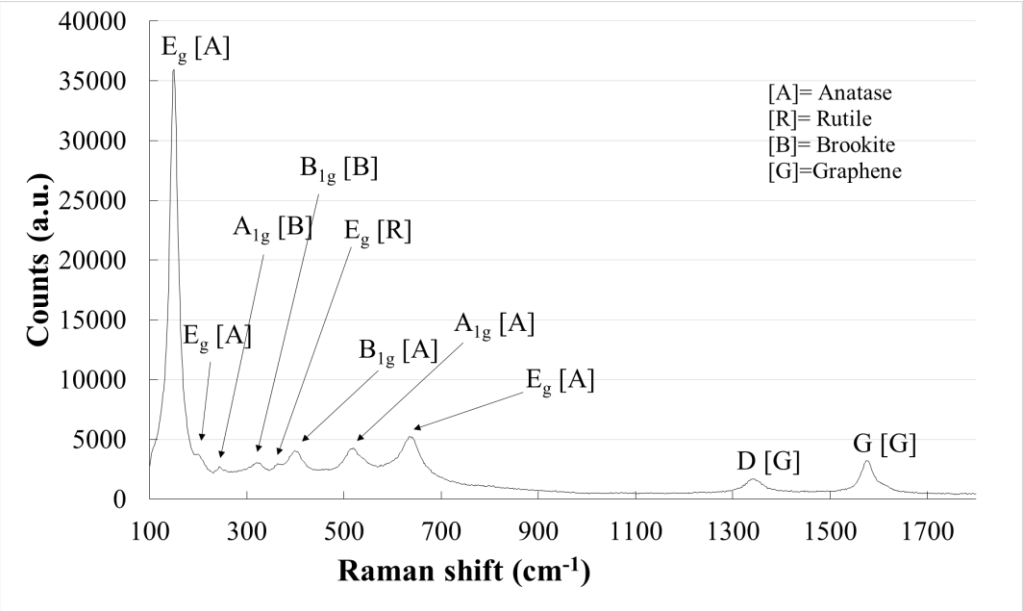

a)

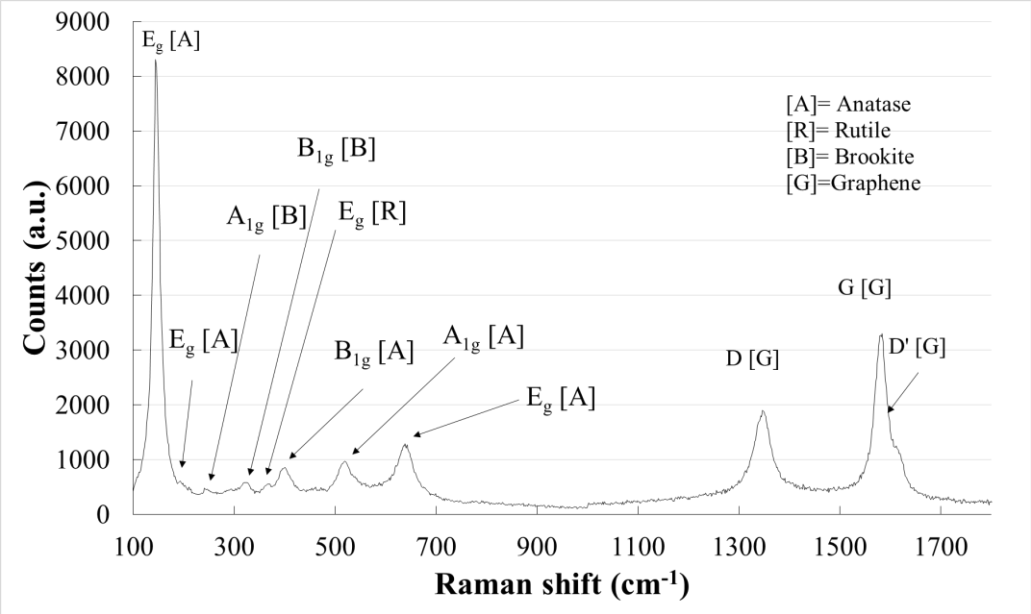

b)

Figure 9-15 a) Raman spectrum of $GTiO_2S$, b) Raman spectrum of $GTiO_2M$.

9.5 Methylene blue degradation test

The degradation of a solution of methylene blue was monitored to quantify and compare the photocatalytic activity of the particles. The reactions considered are at the liquid/solid interface between the TiO_2 particles and the methylene blue. Figure 9-16 reports the normalised concentration versus time in solutions irradiated with UV lights and white LED lights with different wavelength ranges.

Degradation under UV light irradiation plotted in Figure 9-16 a) demonstrates the fact that P25 is one of the most active particles when irradiated with UV light such that more than 70% of the methylene blue degraded in 1 hour. This can be considered in comparison to sample $GTiO_2S$ which has comparable performance with more than 50% of methylene blue degraded in the same amount of time. Broadening the spectrum of the irradiating light source by using visible light can increase the performance of both $GTiO_2M$ and $GTiO_2S$. This could be due to the possible carbon doping of TiO_2 during the annealing process which can improve the photocatalytic activity as observed in commercially available products such as K7000. The presence of carbon can create a mid-bandgap electronic state and improve the charge pair generation recombination as studied by Park et al. [186].

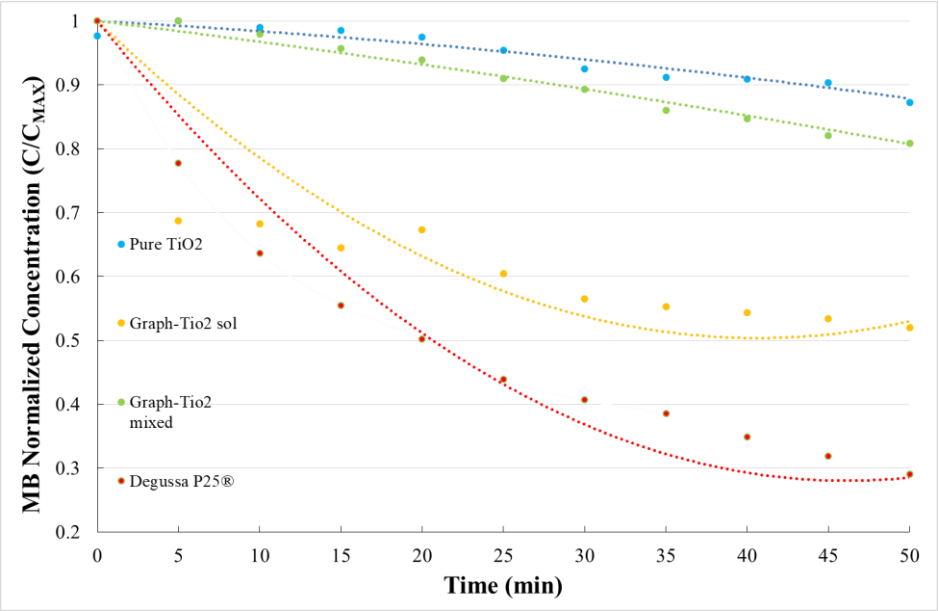

a)

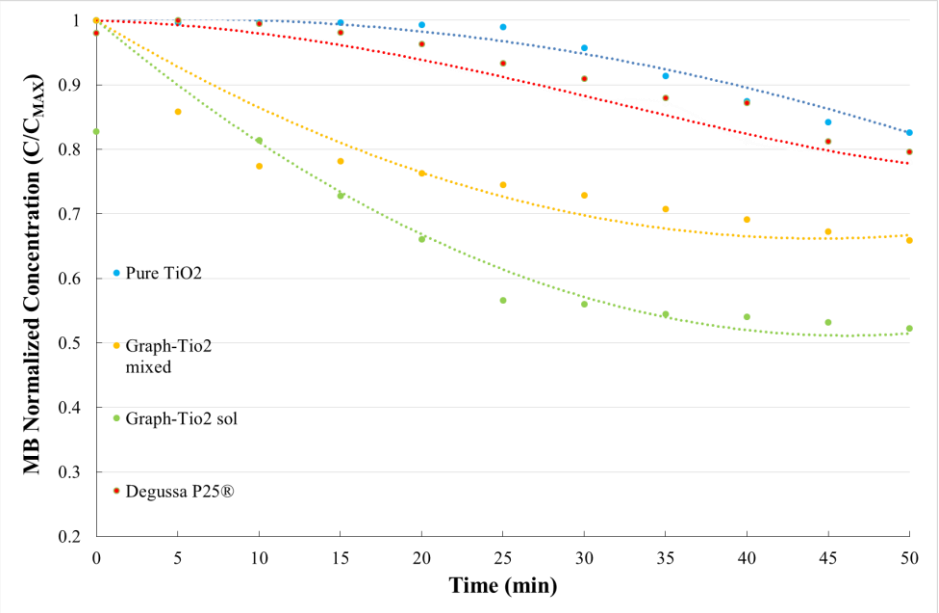

b)

Figure 9-16 a) Methylene blue degradation of samples irradiated with UV light b) Methylene blue degradation graph samples irradiated with LED white light (390 to 700 nm).

9.6 NO_x degradation test

NO_x degradation under visible light (OSRAM solar lamp) shown in Figure 9-17 is in agreement with the degradation of methylene blue and demonstrates that $GTiO_2M$ is superior in performance compared to the commercial particle. The difference between the performances is lower than in the liquid/solid experiment. This can be attributed to various factors such as the mechanisms involved in gas solid interactions and the spectral range of the lamps used.

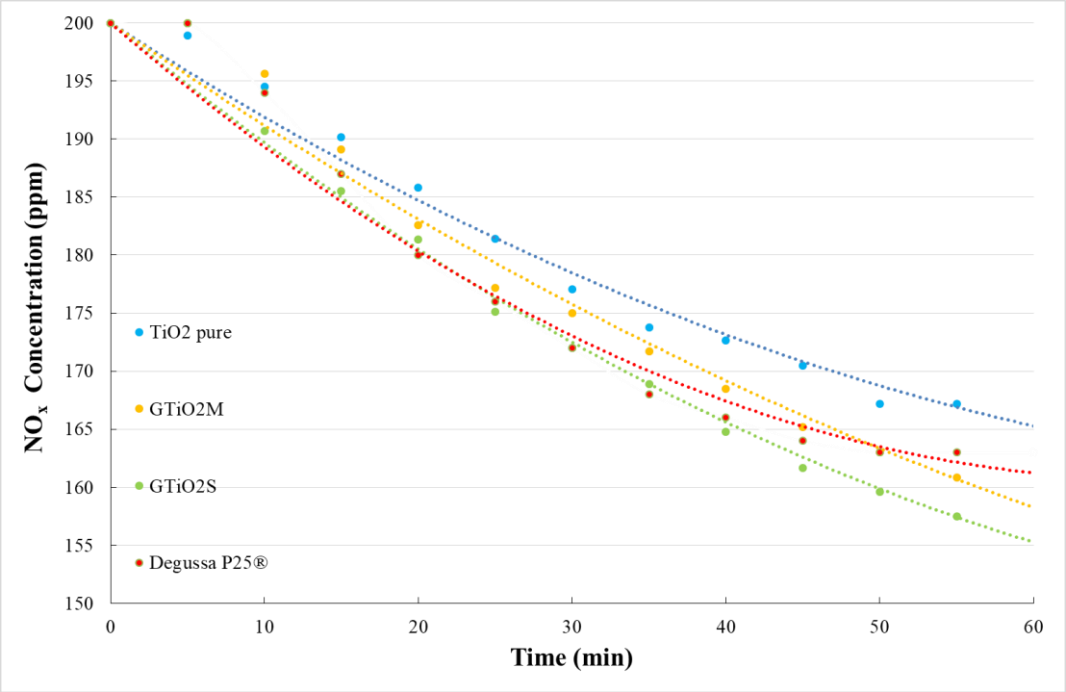

Figure 9-17 NO_x degradation graph of all the samples irradiated with an OSRAM solar lamp. Negative time indicates a period of stabilization of the chamber, positive time indicates that the light has been turned on starting the experiment.

9.7 Conclusions

The following conclusions can be drawn from this chapter:

- Sol-gel synthesis was successfully used to produce graphene/TiO_2 nanoparticle aggregates. The mixing protocol used to produce graphene/TiO_2 was successfully used to synthesize an intricate network of graphene and TiO_2.

- The proportion of anatase and brookite in GTiO_2S and Pure TiO_2 are similar as shown by Rietveld agreement factors. GTiO_2M has a smaller amount of anatase and a major presence of Graphene as shown by Raman spectroscopy and electron and helium ion microscopy techniques.

- Methylene blue degradation, under UV light, of the synthesised sample and commercial particles confirms that GTiO_2S has comparable performance to P25 whereas GTiO_2M and pure TiO_2 have a lower performance.

- Degradation testing under visible light has an opposite trend to that under UV. Both the hybrids shows better performance compared to pure TiO_2 and commercial P25. GTiO_2S and GTiO_2M degrade 30% and 20% more methylene blue, respectively, compared to the reference P25. This supports the use in visible light of active PC coatings.

- NO_x degradation tests highlighted similar trends to methylene blue degradation. Synthesised and commercial particles showed a similar trend. Both graphene hybrids removed a higher % of NO_x in the same amount of time when irradiated with an Osram visible light than commercial or pure TiO_2.

10 TiO_2 based coatings for application onto medium density fibreboard (MDF)

The aim of this chapter is to characterise and compare TiO_2 based coatings for application onto MDF substrates. Raman spectroscopy, SEM and EDX were used to characterize the composition of the coatings manufactured from commercially available TiO_2 particles and sol-gel TiO_2. The photocatalytic performance of the coatings was studied as described in Chapter 6.

10.1 SEM, EDX, Raman spectroscopy and optical microscopy

SEM, EDX Raman spectroscopy and optical microscopy were applied to investigate the micro and nanostructures of the MDF substrate surface.

Figure 10-1 shows a detailed cross section of the interface between the medium density fibreboard (MDF) and melamine urea formaldehyde (MUF) resin impregnated paper. Numerous air bubbles are visible in the MUF resin impregnated paper.

Figure 10-2 shows the uncoated MDF surface where the darker background, grey area, is attributed to the paper coating. The energy dispersive X-ray map shown in Figure 10-3 highlights the location of titanium. The pattern of titanium resembles that of the fibres, suggesting the fibres have become covered in the TiO_2 particles. Large clusters of TiO_2 are also evident, similar to those observed in the untreated paper. Titanium dioxide particles are added to the paper as a whitening pigment and also to improve the mechanical properties. These TiO_2 particles are rutile in structure and they are not photocatalytic.

Figure 10-4 a) shows the surface of MDF coated with sol-gel cobalt doped TiO_2 on the surface of MDF coexisting with the already present rutile. In Figure 10-4 b) peaks corresponding to carbon, oxygen and titanium are visible with the titanium signal originating from the rutile pigment. Figure 10-4 b) reports that analysis of the cobalt doped TiO_2 gives a similar spectrum. Due to the sensitivity of the EDX analysis and also the relatively low cobalt doping concentration, 1%, peaks corresponding to cobalt are not evident within the spectrum of a single point but a larger area was scanned to obtain the peaks of interest.

Figure 10-5 a) shows the surface of a typical sol-gel 3% tungsten doped TiO_2 based MDF coating over the pre-existing rutile on the surface. The presence of doping and commercial TiO_2 are shown in Figure 10-5 b) and c) with peaks from carbon, oxygen, titanium and tungsten identified.

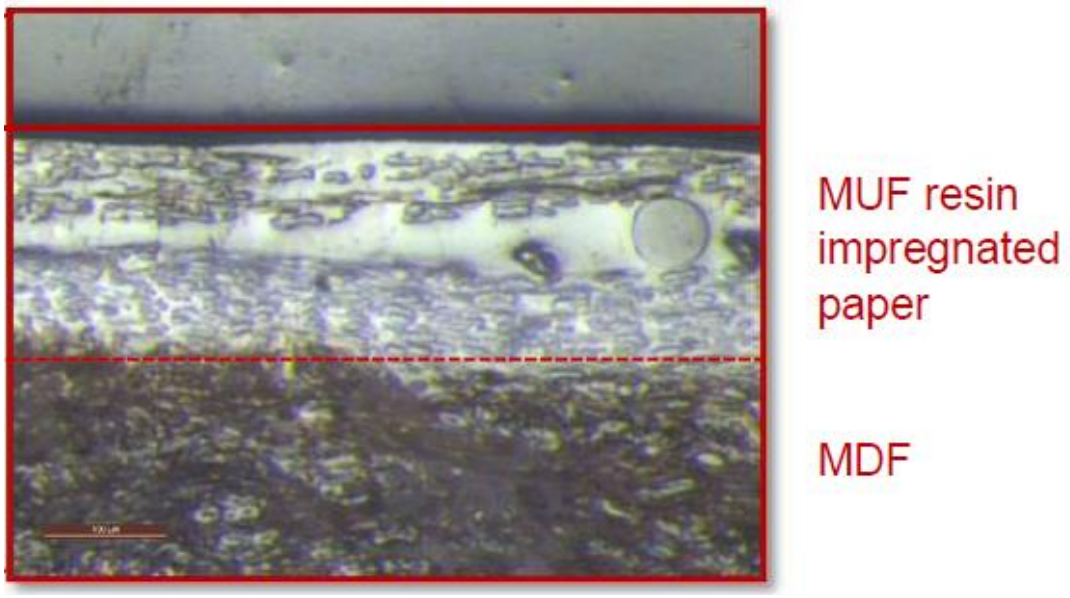

Figure 10-1 Section through MDF substrate and décor finish (scale bar = 100μm).

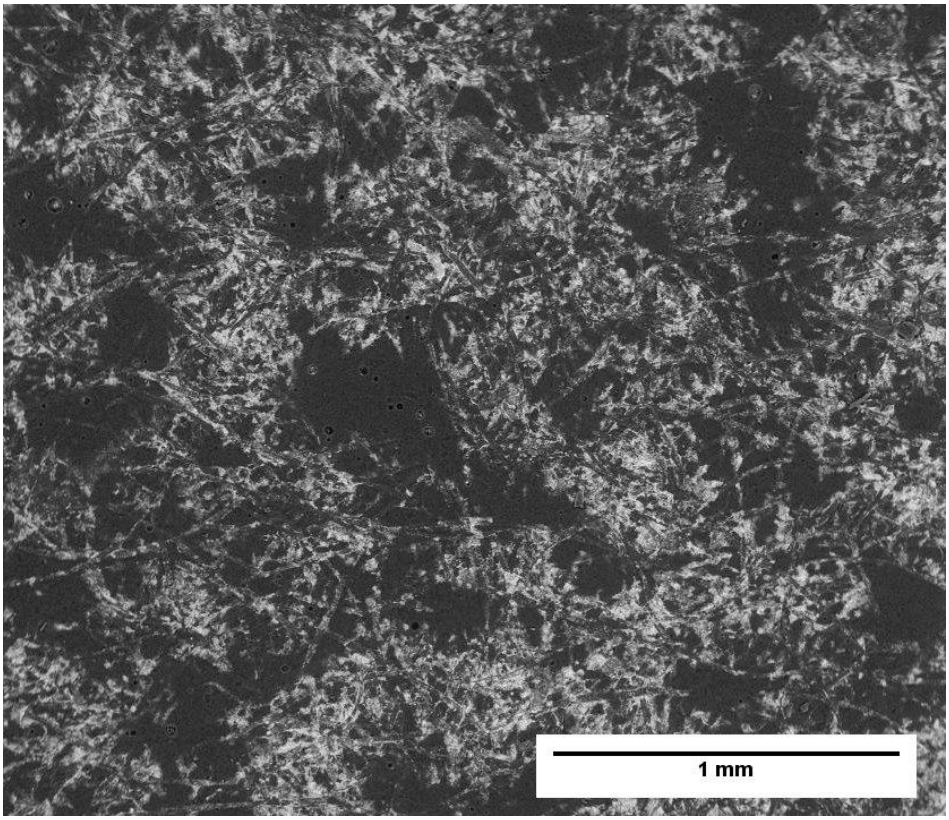

Figure 10-2 SEM image showing the general appearance of the uncoated MF-MDF surface. Dark melamine is crossed by randomly orientated flattened softwood fibres.

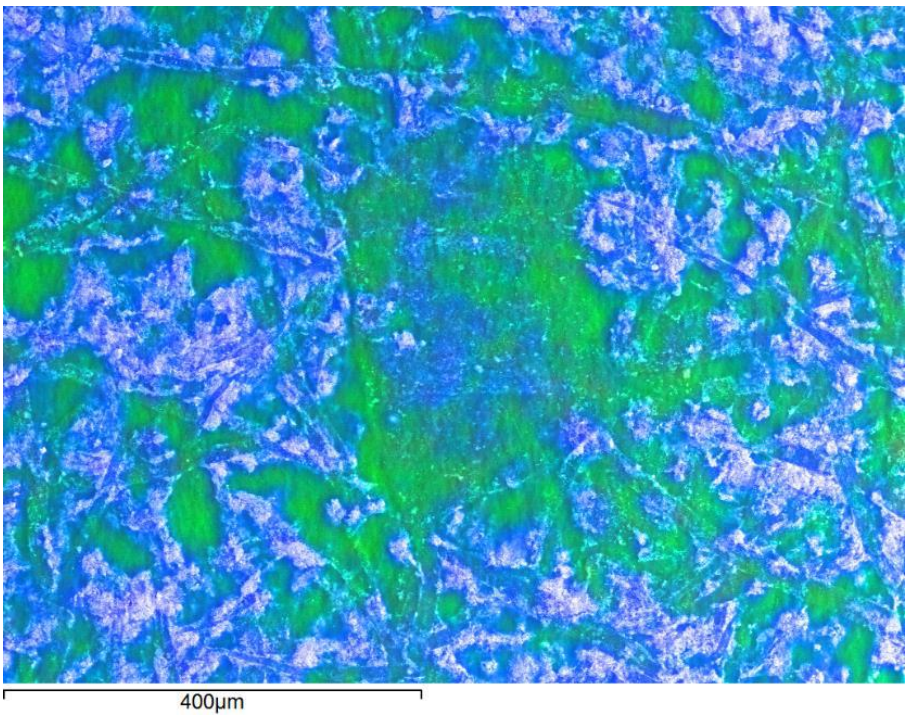

Figure 10-3 EDX map of the MUF-impregnated décor finish showing pre-existing TiO_2 (blue) forming large clusters amongst the MUF resin (green).

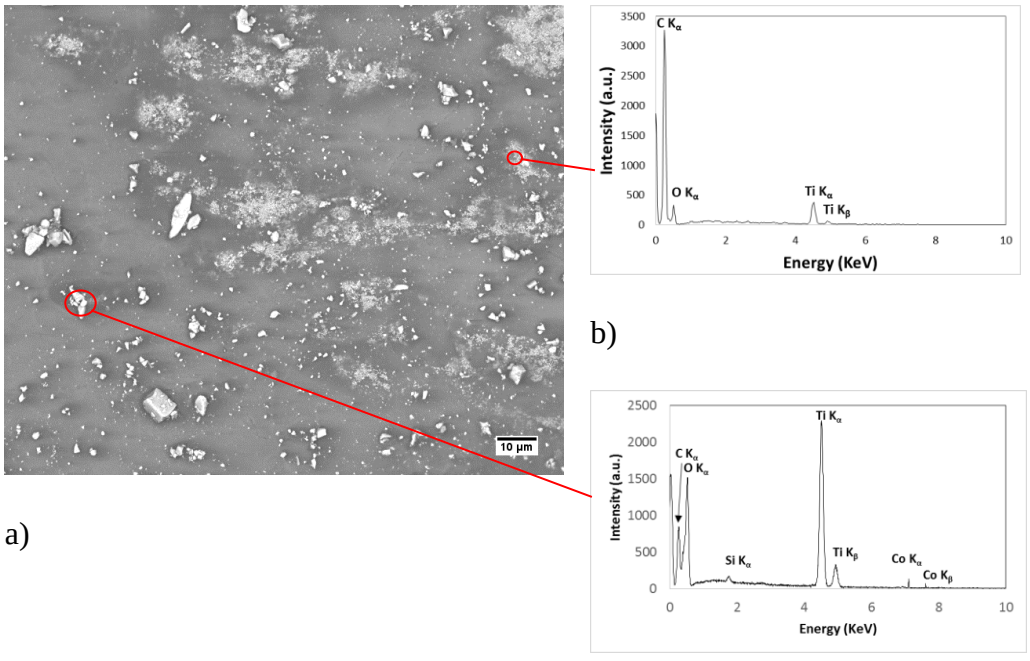

a)

b)

c)

Figure 10-4 a) SEM image of MDF coated with cobalt doped TiO_2 b) EDX spectra on MUF resin (containing rutile-TiO_2 pigment) c) EDX of TiO_2 aggregate surface.

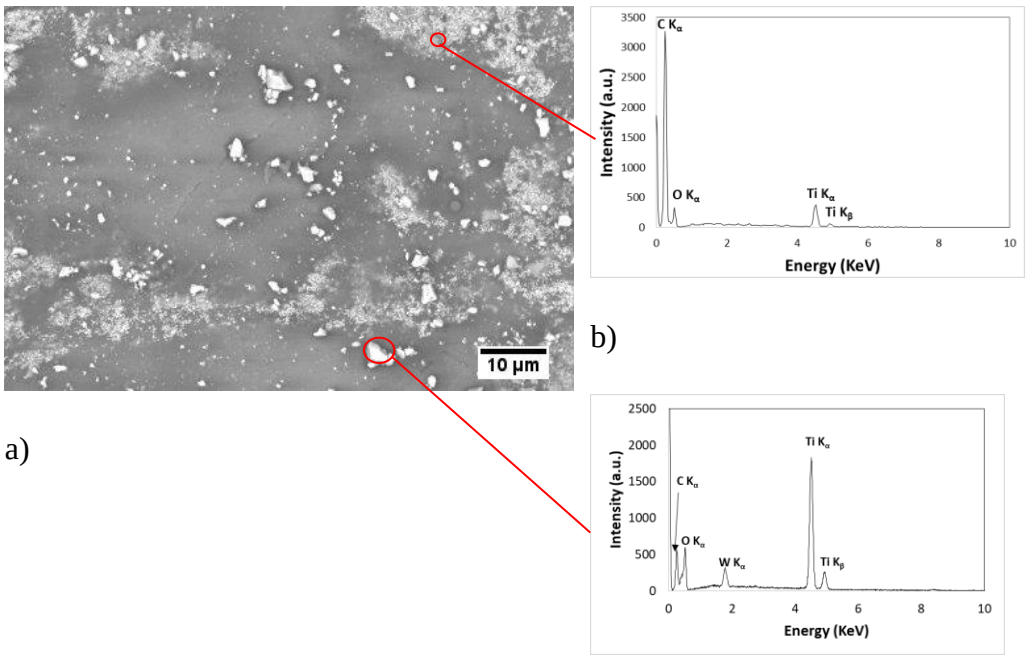

Figure 10-5 a) Typical SEM image of MDF coated with 3% tungsten doped TiO_2 b) EDX spectra on MUF resin (containing rutile-TiO_2 pigment) c) EDX of 3% tungsten doped TiO_2 on aggregate surface.

10.2 Evaluation of Photocatalytic activity using Ink Intelligent inks

Figure 10-6 presents typical results from uncoated MDF, used as a standard, and three different coatings incorporating K7000, Co-doped TiO_2 and pure TiO_2 photocatalytic particles. The indicator stripes on the left and right hand sides are BB66 and Rz respectively. The presence of the coating on the surface modified the surface energy of the substrate which is apparent from the poor wetting (high contact angle) of the Rz based ink. The bottom half of the substrates (below the dashed line) was shielded with a metal plate. The photocatalytic activity was correlated with the change in colour from blue to pink and then to transparent in the BB66 based ink, and from blue to transparent in the Rz based ink. The synthesised cobalt doped material displays a more intense reaction with the inks showing a faster degradation compared to undoped and commercial particles. In all cases, the degradation began 5 minutes after the initial irradiation.

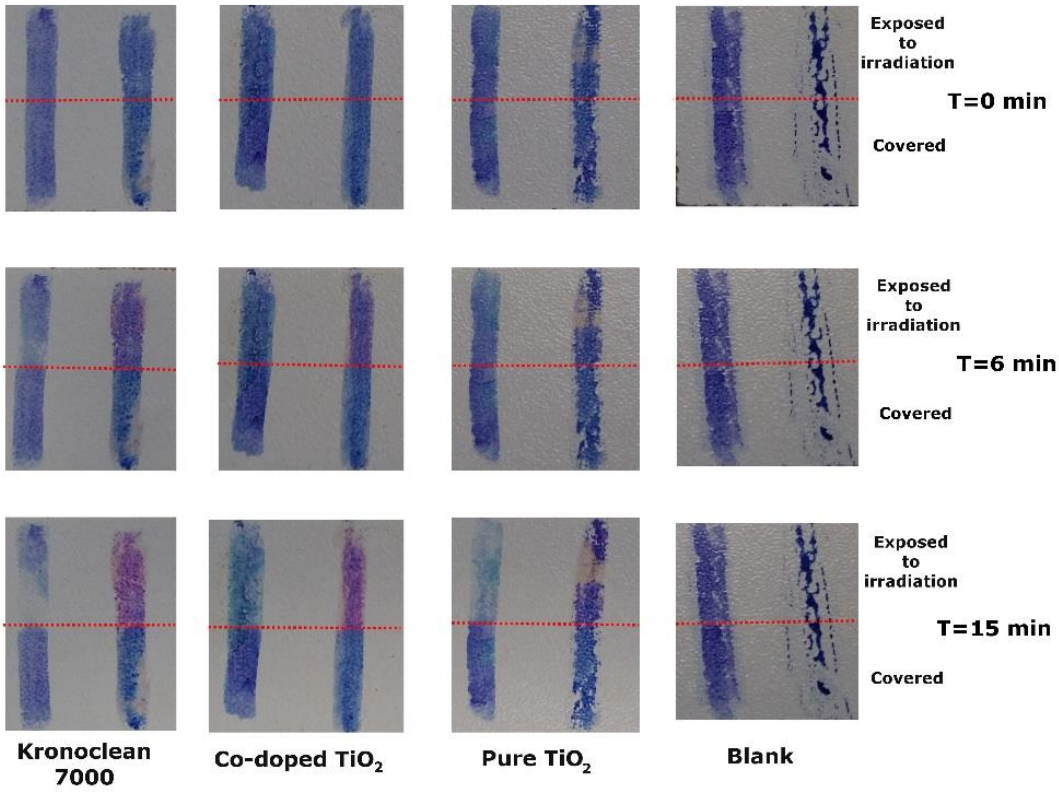

Figure 10-6 Ink Intelligent photocatalytic test on MDF samples coated with K7000, Co-doped TiO_2 pure TiO_2 based coatings and blank irradiated with UV light. A clear change in colour from blue to colourless of the BB66 based ink applied on the left side of the MDF samples is visible. Rz dye on the right side changes colour from blue to pink.

Figure 10-7 presents typical results from four different coatings based on, 1%W-doped TiO_2, 3%W-doped TiO_2, pure TiO_2 and P25. All the coupons have the indicator stripes applied in the sequence of BB66 on the left side and Rz on the right side. The presence of the coating on the surface did not show evidence of modifying the wettability of the substrate. The top half of the substrates (below the dashed line) were shielded with a metal plate. The photocatalytic activity was correlated with the change in colour from blue to pink and then transparent in the BB66 based ink, and from blue to transparent in the Rz based ink. The synthesised cobalt doped material displays a more intense reaction with the inks showing a faster degradation compared to undoped and commercial particles. In all cases, the degradation begins 5 minutes after the initial irradiation.

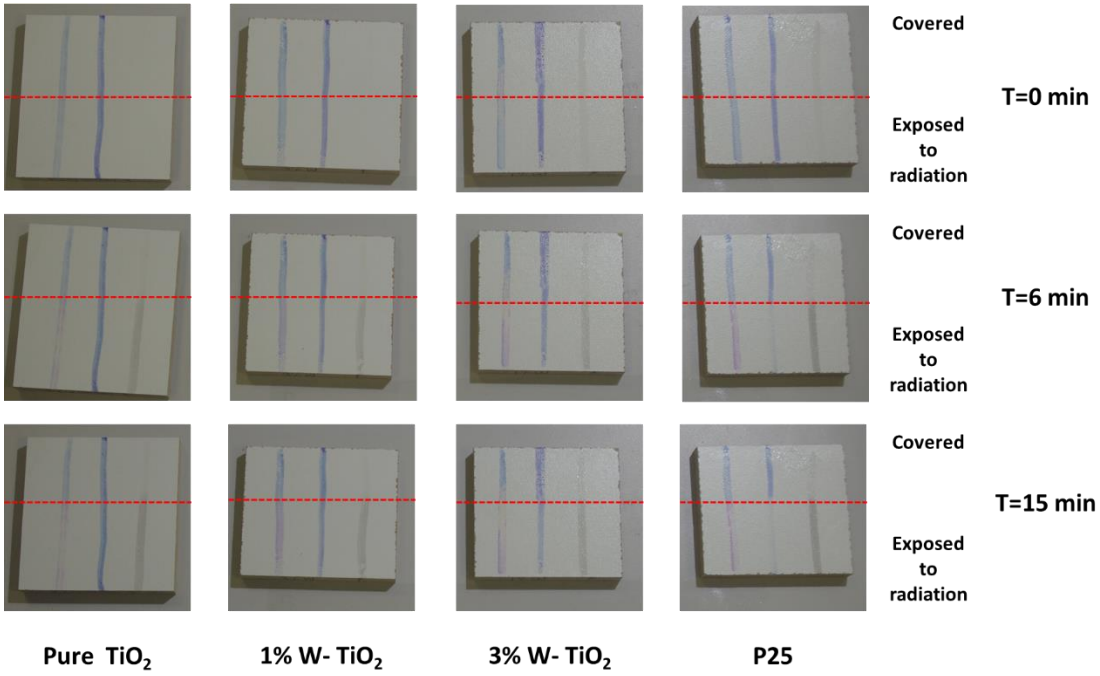

Figure 10-7 Ink Intelligent photocatalytic test on MDF samples coated with pure TiO_2, 1% W-doped TiO_2, 3% W-doped TiO_2, and P25 irradiated with UV light. BB66 based ink applied on the left side of the MDF samples changes colour from blue to colourless and Rz on the right side changes colour from blue to pink.

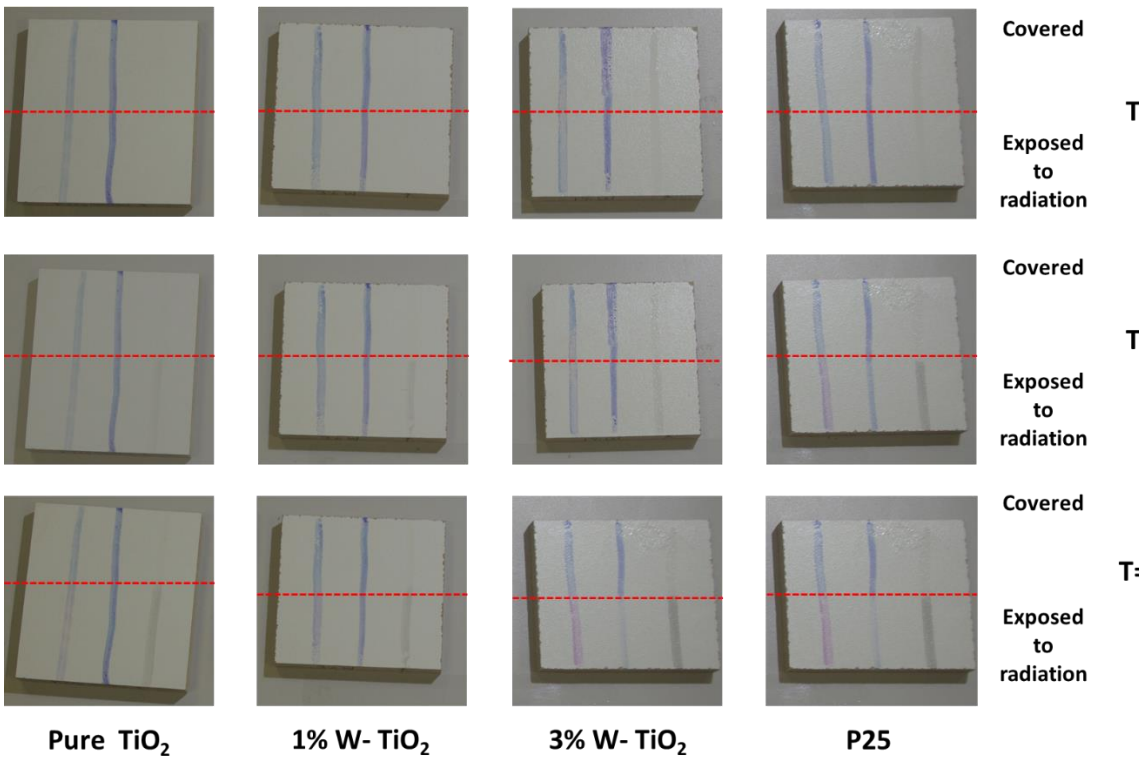

Figure 10-8 Ink Intelligent photocatalytic test on pure TiO_2, 1% W-doped TiO_2, 3% W-doped TiO_2, and P25 irradiated with LED white light. Rz on the left side changes colour from blue to pink. BB66 based ink applied on the middle of the MDF samples changes colour from blue to colourless and Validator (patent protected ink) applied on the right side change from colourless to brown.

Density of the wet coating based on the K7000 and pure TiO_2 nano-formulation

The coating formulation based on anatase powder, which is comprised of clusters of TiO_2 anatase nanoparticles is presented below by weight.

- K7000 (0.5%)
- IPA (25%)
- Water (72.5%)
- Polyurethane/acrylic resin (2.0%). The average density of coating is calculated in Table 10-1

Table 10-1 Estimation of density of wet PC coating.

Component	Composition (wt. %)	Density (g/cm^3)	Density contribution (g/cm^3)
TiO_2	0.5	3.9	0.0195
IPA	25.0	0.786	0.1965
Water	72.5	1.00	0.725
PU/A	2.0	1.20	0.024
		Average density =	**0.97**

Gravimetric determination of wet coating thickness when applied to a glass microscope slide

The thickness of the wet coating just after the application was determined gravimetrically using the method described below. Firstly a glass microscope slide (2.6 cm by 7.6 cm) was weighed. The coating was then brushed onto one face of the slide and the slide was weighed. By subtraction, the wet mass per unit area was calculated to be 22.1 g/m^2. Assuming a coating density of 0.97g/cm^3 the wet thickness was calculated to be 22.7 microns (22,700 nm).

Gravimetric determination of dry coating thickness when applied to a glass microscope slide

The wet coating was dried in a fume cabinet and the mass per unit area fell to ~0.2 g/m^2 following evaporation of the water and IPA. The proportion of TiO_2 to PU/A was 1:4 by weight. Hence the average density of the dry coating, 1.74 g/cm^3 was calculated from Table 10-2.

Table 10-2 Estimation of density of dry PC coating.

Component	**Composition (wt. %)**	**Density (g/cm^3)**	**Density (g/cm^3)**	**contribution**
TiO_2	20	3.9	0.78	
PU/A	80	1.20	0.96	
		Average density =	**1.74**	

Assuming that the nanoparticles in the PU/A polymer coating are uniformly distributed, the dry thickness was 0.1066 microns or 107 nm, calculated from the average density and mass per unit area. In practice, the dried coating is non-uniform because the particle size of some of the clustered TiO_2 nanoparticles exceeds 107 nm. The dry coating thickness is of the order of 200 times less than the wet thickness.

10.3 Conclusions

- The coated samples have a similar appearance to the uncoated 'control' specimen at macroscopic and microscopic scales.
- None of the coatings applied were noticeable through examination with the naked eye in terms of either the colour or surface gloss.
- The presence of rutile particles distributed throughout the impregnated paper was confirmed by SEM. Further SEM analysis following the application of the coating was able to identify the sol-gel particles.
- The use of Ink Intelligent dyes to assess the photocatalytic activity of the Co doped TiO_2 and pure TiO_2 showed promising results when compared to the commercially available TiO_2 particles tested. All the coatings were active to some extent under UV irradiation promoting degradation of the inks after a few minutes.
- Photocatalytic behaviour of tungsten doped and pure TiO_2 based coatings were similar with both UV and visible irradiation. The particles containing 3% W doped TiO_2 showed a greater photocatalytic activity compared to the 1% tungsten doped particles. Degradation of the dyes in all cases demonstrated the ability of the coatings developed to be used in the built environment.
- The wet thickness of a coating (based on k7000) on glass slide substrate was calculated to be 20 micrometers.
- The dry thickness of a TiO_2 coating on glass slide substrate was estimated to be 0.1 micrometers.
- It should be noted that the wet and dry thicknesses may be influenced by the smoothness of the substrate (e.g. flat glass plate or décor finish).

11 Evaluation of photocatalytic lime formulations

This chapter presents the characterization and evaluation of photocatalytic lime formulations. Data obtained from colour variation, XRD, Mercury intrusion porosimetry, BET SEM and EDX are presented. Comparisons are made between blank plaster containing no photocatalyst and plasters containing various percentage of K7000. The photocatalytic performance was studied following formaldehyde degradation as previously described in Chapters 5 and 6.

11.1 Macro pictures and colour variation

The colour variation of the test specimens was evaluated. Macro pictures of the photocatalytic samples ETDK2, ETDK3 and ETDK5 are compared to the blank sample ETD in Figure 11-1.

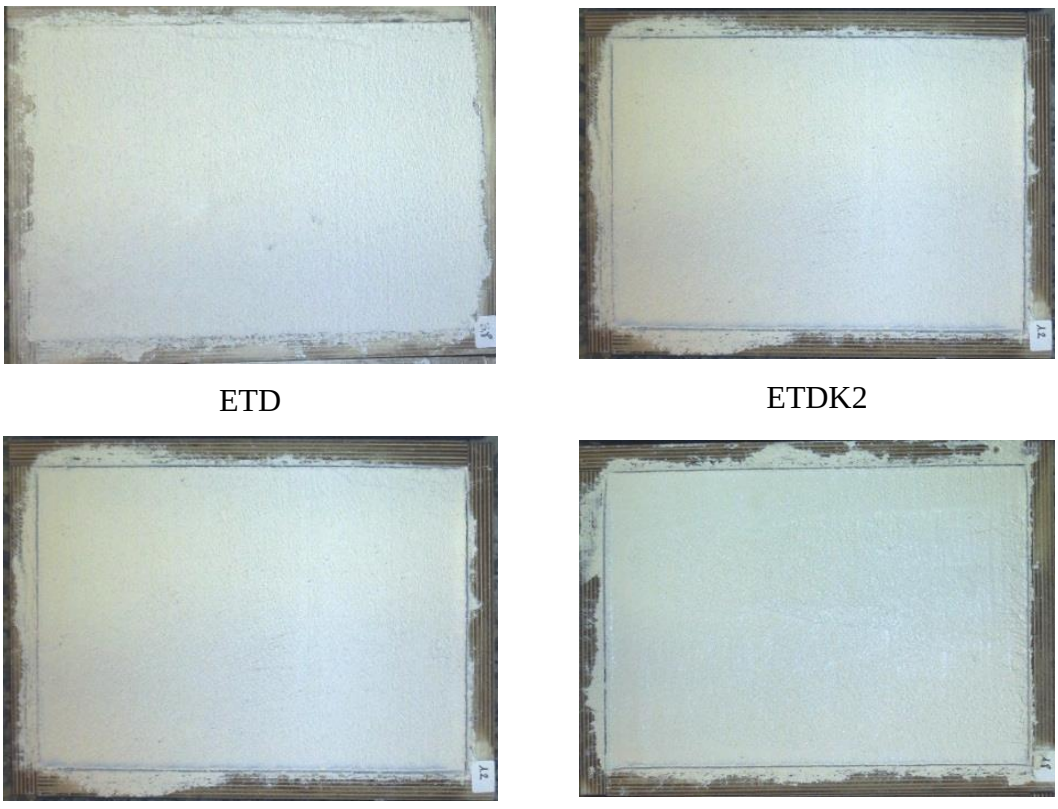

Figure 11-1 Macro pictures of the three photocatalytic samples and the ETD blank.

Colour variation is defined using the CIELAB [187] colour space described by three values: a*, b*, L* that represent components of a vector. The difference in colour is achieved by comparison of the sample values (**L_2^*, a_2^*** and **b_2^*)** with a blank (**L_1^*, a_1^*** and **b_1^*)**, which in this case is ETD. ΔE^* (E stands for Empfindung; German for "sensation") can be calculated using equation 11.1 [188] as reported by Sharma et al. After looking at the difference of the sample values (**L_2^*, a_2^*** and **b_2^*)** with a blank, and being sure that the difference in the components are not noticeable we can assume that if the value of ΔE^* is over 2.3 it corresponds to a noticeable difference. The data from Table 11-1 implies that the colour change attributed to the presence of K7000 nanoparticles inside and on the surface of the photocatalytic plaster is not significant enough to be noticeable to the naked eye.

$$\Delta \mathbf{E}^* = \sqrt{(\boldsymbol{L_2^*} - \boldsymbol{L_1^*})^2 + (\boldsymbol{a_2^*} - \boldsymbol{a_1^*})^2 + (\boldsymbol{b_2^*} - \boldsymbol{b_1^*})^2} \qquad (11\text{-}1)$$

Table 11-1 Colour CIELAB parameters (ΔE* values over 2.3 correspond to a noticeable difference).

Plaster	**L^***	**a^***	**b^***	**ΔE^***	**ΔL^***	**Δa^***	**Δb^***
ETD	90.07	0.14	4.37	0			
ETDK2	91.16	0.11	4.17	1.11	1.09	-0.3	-0.2
ETDK3	91.51	0.18	4.03	1.48	1.44	0.04	-0.34
ETDK5	90.81	0.26	4.46	0.76	0.74	0.12	0.09

11.2 Mineralogy

XRD analyses showed that the cured Tradical Décor lime plaster (ETD) is composed mainly of quartz (SiO_2) accompanied by calcite ($CaCO_3$). Minor amounts of portlandite ($Ca(OH)_2$), vaterite ($CaCO_3$), aragonite ($CaCO_3$) and rutile (TiO_2) were also detected as seen in Figure 11-2. The addition of K7000 nanoparticles to the plasters (ETD2, ETDK3 and ETDK5) did not lead to significant changes. Similarly to the reference plaster (ETD), these plasters were composed of mainly quartz (SiO_2) accompanied by calcite ($CaCO_3$). Minor amounts of portlandite ($Ca(OH)_2$), vaterite ($CaCO_3$), occasional aragonite ($CaCO_3$) and rutile were also detected. The presence of Portlandite implies that the mortar was not fully carbonated when analysis was performed after 28 days. This is quite common in lime mortars where carbonation takes between a few weeks and several years [189]. The rutile TiO_2 detected in the XRD spectra originates from the Tradical Décor (ETD) mortar and is present in the material. Additionally, the diffractograms contain a low intensity peak at a 2θ value of 25.5° attributed to the anatase present in K7000. The intensity of the diffraction peak increased with the amount of K7000 added.

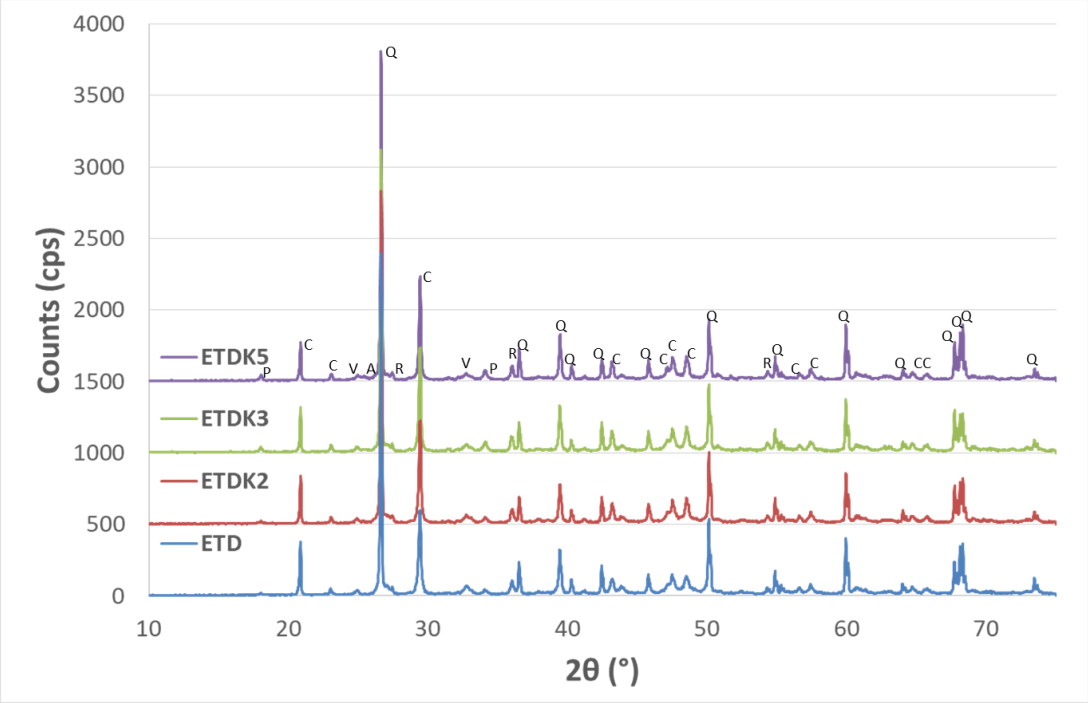

Figure 11-2 XRD spectrum of ETD, ETDK2, ETDK3, and ETDK5, Zoomed XRD spectrum of ETD, ETDK2, ETDK3, and ETDK5 in the region where anatase is detected.

Labels: A –Anatase; C – Calcite; P – Portlandite; Q – Quartz; R – Rutile, V - Vaterite

11.3 SEM inspection of lab-scale formulated plaster coatings

The cured Tradical Décor lime plaster (ETD) has a nodulous smooth surface (Figure 11-3 a) when examined by SEM. At greater magnification, it can be seen that this surface is actually rough because of the abundant irregular pores that are present. EDX analysis (Figure 11-3 c) shows that this plaster contains mainly Ca, Si, O, C and Ti. Other minor elements (K, S, Al and Na) are also found. This composition agrees with the mineralogical analysis. Figure 11-3 b shows that Ti is already present in the commercial Tradical Décor product and is uniformly distributed throughout the plaster sample.

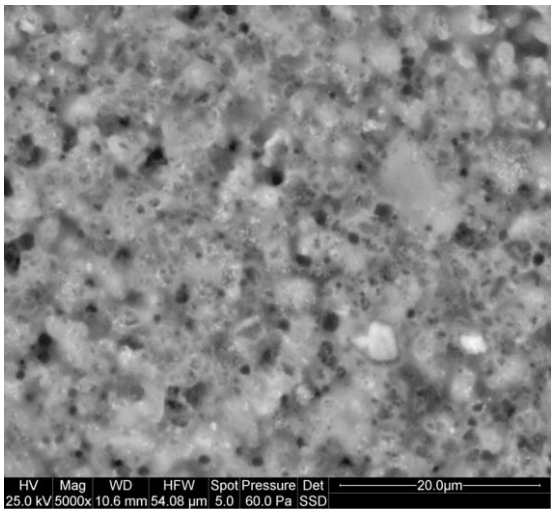

a)

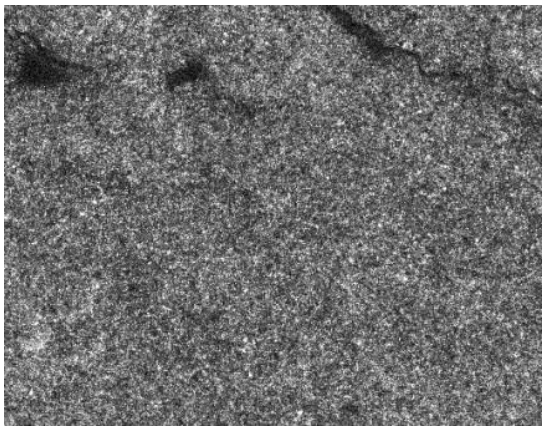

b)

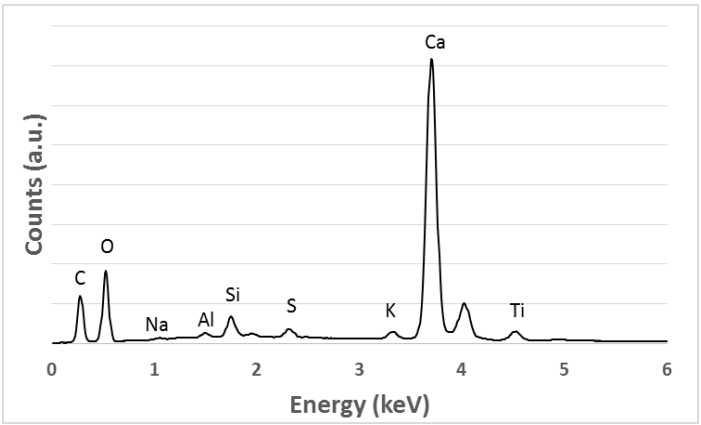

c)

Figure 11-3 a) SEM image showing Tradical decor plaster surface, b) EDX map identifying the titanium distribution in the sample, c) EDX spectrum of the surface.

SEM inspection of the three Tradical Décor lime plasters with added K7000 nanoparticles (ETDK2, ETDK3 and ETDK5) shows that the original microstructure of the reference lime plaster (ETD) is preserved. Accordingly, the surface of these plasters is nodulous and smooth Figure 11-3 a) and Figure 11-4 a), with numerous irregular pores that add micro-roughness. These plasters also contain mainly Ca, Si, O and C (and Ti, K, S, Al and Na as minor elements). This composition agrees with the mineralogical results. EDX analysis shows that the titanium present in all these plasters has a uniform distribution. It is not possible to distinguish the distribution of the added TiO_2 (K7000) because its XRF signal is identical to that of the titanium in the Tradical Décor plaster (Figure 11-3 b and Figure 11-4 b). However, from EDX analysis, it can be seen that the intensity of the Ti peak grows as the amount of K7000 is increased (Figure 11-3 c and Figure 11-4 c).

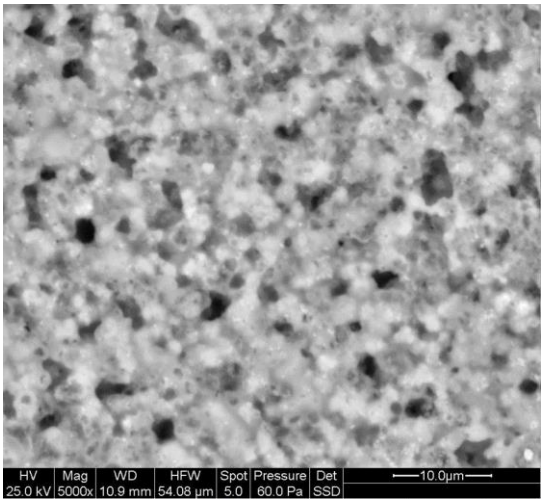

a)

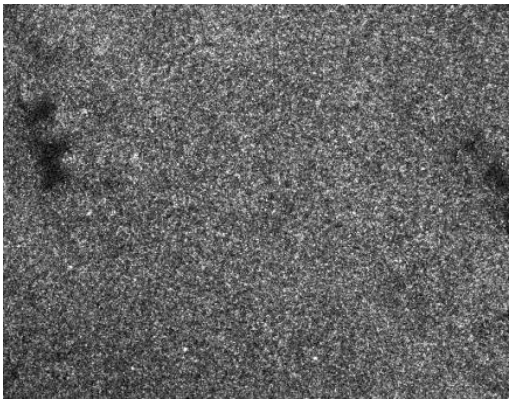

b)

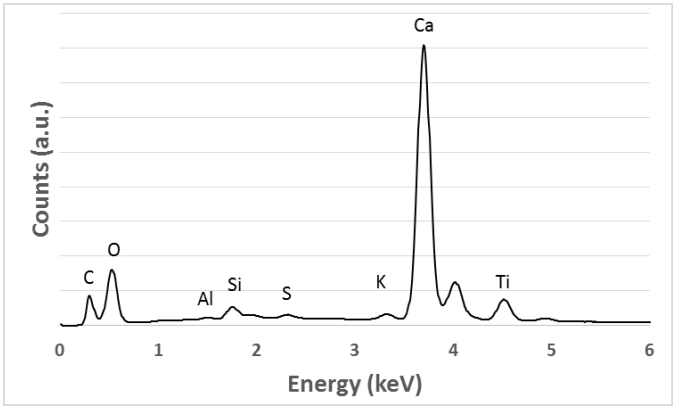

c)

Figure 11-4 a) SEM image showing Tradical decor plaster with 3% K7000 on the surface, b) EDX map reporting titanium distribution in the sample, c) EDX spectrum of the surface.

11.4 Mercury intrusion porosimetry of lab-scale formulated plaster coatings.

The porosity, density, average pore size and pores distribution of the four Tradical Décor based plaster coatings was measured by mercury intrusion porosimetry, results of which are presented in Table 11-2.

Table 11-2 Formulated Lime plaster coatings: Mercury porosimetry analyses results.

Coating	Porosity %	Skeletal g/cm^3	Bulk g/cm^3	Average pore Ø (µm)
ETD	29	2.5	1.8	1.0
ETDK2	30	2.5	1.7	0.9
ETDK3	30	2.5	1.7	0.9
ETDK5	33	2.5	1.7	0.8

The reference plaster (ETD) has a porosity of 29% and an average pore size of 1.04 µm. The K7000 plasters have different porosity values. In the case of ETDK2 and ETDK3 (2 and 3 wt% K7000), the porosity is barely changed with respect to the blank sample (ETD), but in the case of ETDK5 (5 wt% K7000), an increase in porosity from 29% to 33% is observed. This porosity increment is coupled with a reduction of the average pore size (from 1.04 µm for ETD to 0.82 µm for ETDK5), as can be seen in Table 11-2 and Figure 11-5 below.

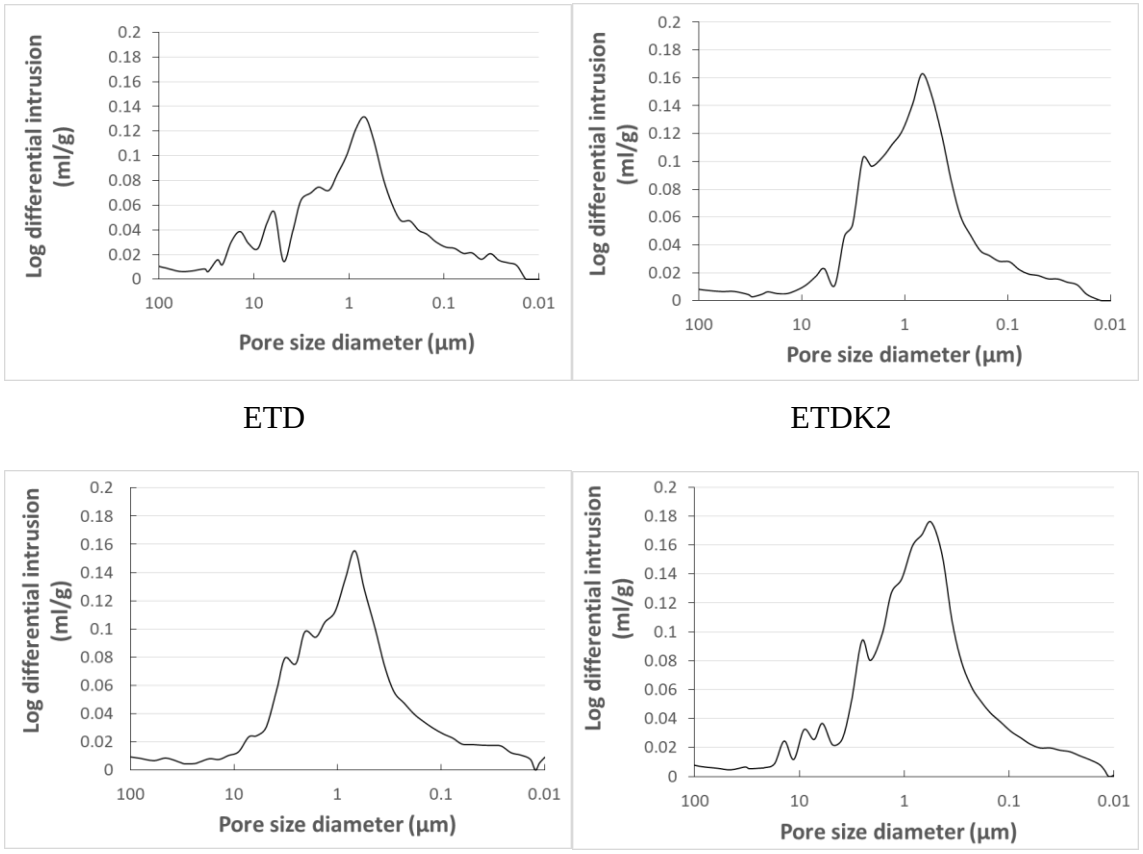

Figure 11-5. Pore size distribution of ETD, ETDK2, ETDK3 and ETDK5.

11.5 BET surface area results

To measure the surface area, the amount of adsorbed nitrogen required to cover the material surface is determined. The amount of gas adsorbed by the mass of material being tested is dependent on the relative pressure and temperature. In this case, all the measurements are isothermal [190]. In Figure 11-6 a) the BET adsorption/desorption isotherms of the reference and the three photocatalytic plasters are presented. An isotherm represents the relationship between the amount of nitrogen adsorbed by a unit of mass of material and the equilibrium pressure at known temperature following the BET equation (presented in paragraph 3.5) [190]. A change in the nitrogen adsorption/desorption isotherms is observed for the different amounts of TiO_2 added to the lime plasters which, led to different surface areas. The specific surface area values and respective standard deviation bars are presented in Figure 11-6 b). The reference plaster, ETD, showed the lowest surface area, 1.6 m^2/g. The addition of 5 % of K7000 nanoparticles led to an increase of 65 % in the surface area.

BET results are inversely correlated with the average pore size measured by mercury intrusion porosimetry, where a reduction of the pore size was observed in the samples with higher content of nanoparticles. These results demonstrate that the addition of K7000 nanoparticles refines the pore structure, by being allocated between the lime particles (pores) leading to smaller pores in the final product.

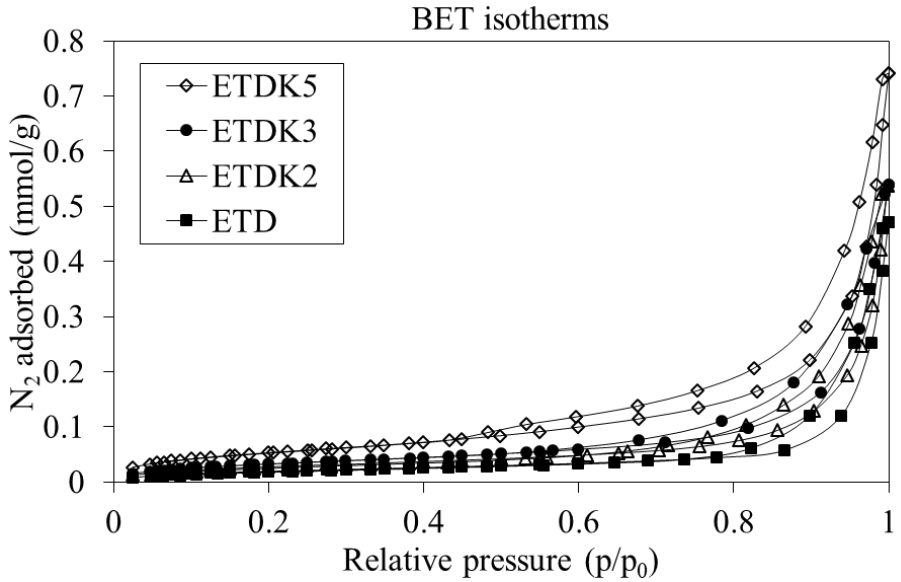

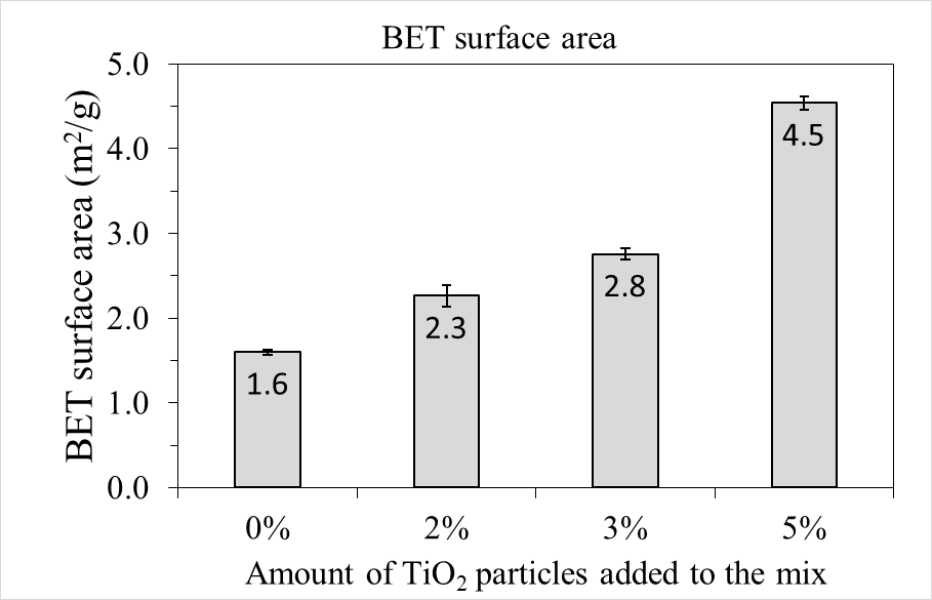

Figure 11-6 a) Nitrogen adsorption/desorption isotherms and b) specific surface area both data [191].

11.6 Photocatalytic degradation of formaldehyde

In the course of the test (carried out in Fraunhofer facilities), reported in Paragraph 6.4, for photocatalytic degradation of formaldehyde under visible light, four different phases were studied. In Phase 1, the chamber was flushed with neutral air. Here the intrinsic emissions from the specimen in absence of light can be detected. In Phase 2, the chamber was flushed with neutral air and the lamps (visible light) were turned on irradiating the specimen surface. This was done in order to examine the light-induced emission of formaldehyde from the samples. In Phase 3, additional gas with an airflow of 1,65 l/min and a concentration of formaldehyde of approx. 90 ppb a total of 12.2 µg/h of formaldehyde flowed over the surface of each sample with the lamps still turned on. Thus, at this stage, the photocatalytic degradation of formaldehyde by the sample could be detected. In Phase 4, the lights were switched off and the addition of the formaldehyde was continued. Thus, the adsorption of formaldehyde by the sample could be determined at this stage. All phases were maintained until a stable formaldehyde concentration status was reached for all samples. For these samples, a total of 839 hours were required to carry out all phases of the test. An example of a formaldehyde degradation test profile is shown in Figure 11-7.

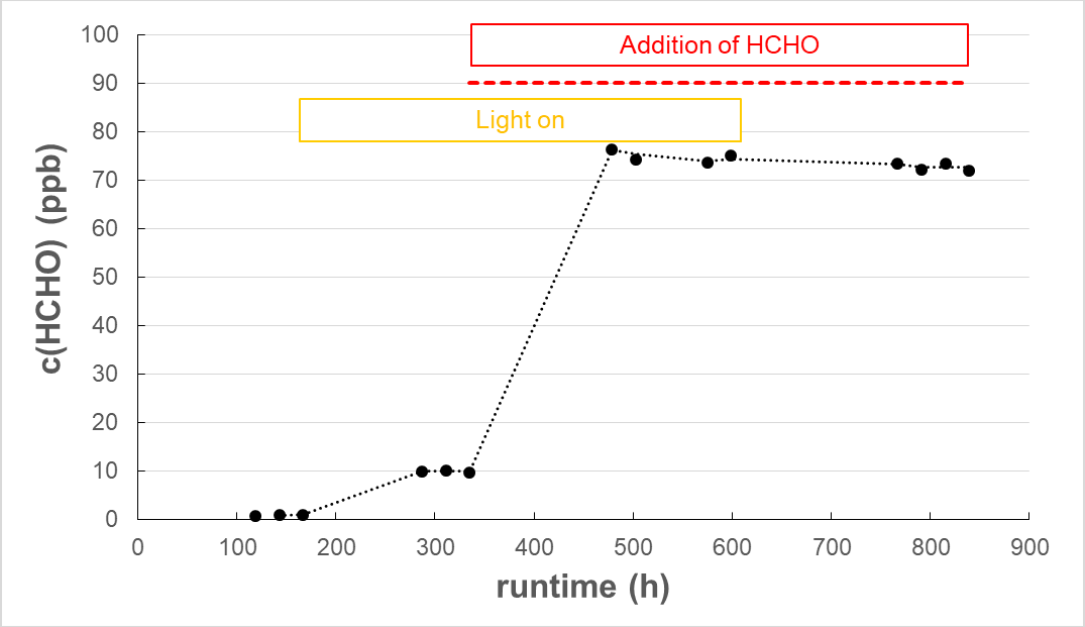

Figure 11-7 Typical photocatalytic degradation of formaldehyde test profiles for ETDK2. The red dashed line represents the incoming concentration of formaldehyde during phases 3 (p3) and 4 (p4).

From the equilibration formaldehyde concentrations in the different test phases, the desired variables are defined as shown below. For every phase, the resulting formaldehyde concentration can be calculated by equation (11-2) reported in chapter 6.5:

$$cRes = cin + cProdO + cProdL – cRedL - cRedA \quad (11\text{-}2)$$

where

cRes = resulting formaldehyde concentration

cin = formaldehyde concentration measured in empty reference chamber

cProdO = formaldehyde concentration from own emission of the specimen

cProdL = formaldehyde concentration from sample emission caused by radiation

cRedL = reduction of formaldehyde concentration caused by radiation

cRedA = reduction of formaldehyde concentration caused by adsorption

The equilibrium formaldehyde concentrations at the end of the experimental phases for all samples are listed in Table 11-3.

Table 11-3 Formaldehyde equilibrium concentrations

Plaster	cRes Phase 1	cRes Phase 2	cRes Phase 3	cRes Phase 4
	own emission without light [ppb]	own emission with light [ppb]	own emission with light + addition of formaldehyde [ppb]	own emission without light + addition of formaldehyde [ppb]
ETD	1	6	76	75
ETDK2	1	10	75	73
ETDK3	1	11	75	73
ETDK5	1	11	75	72

Based on the equilibrium concentrations, the reduction rates of formaldehyde (either caused by photocatalytic reactions or by adsorption) can be calculated and are listed in Table 11-3 for the different samples. Equations 7 and 9 were used and a normalisation in relation with the incoming air (89.9 ppb) was carried out to allow comparison of the results. The reduction of formaldehyde by photocatalysis was significantly enhanced by a factor of two when K7000 was added to the plaster. Additionally, it can be seen that increasing the K7000 concentration above 3 wt% did not lead to a significant increase in photocatalytic performance as shown in Table 11-4. Therefore ETDK3 was shown to be the best option in terms of cost versus photocatalytic activity.

Table 11-4 Reduction of formaldehyde by photocatalysis and by adsorption

Plaster	Reduction by photocatalysis [%]	Standard deviation [%]	Reduction by adsorption [%]	Standard deviation [%]
ETD	5.4	2.7	16.3	2.4
ETDK2	9.9	2.5	18.6	2.5
ETDK3	11.0	3.5	19.0	2.9
ETDK5	11.1	2.5	19.0	2.4

Preparation of photocatalytic plasters by the addition of TiO_2 nanoparticles does not differ significantly compared to the preparation of the normal plaster. Furthermore, the macrostructure together with colour is not affected significantly by the presence of TiO_2 nanoparticles. EDX spectroscopy did not show any noticeable difference in elemental constitution. In contrast, porosimetry studies showed that there is an increase in porosity, bulk porosity and a reduction in the average pore size in the ETDK5 sample due to larger amounts of K7000 in the sample.

Photocatalytic performance in degrading formaldehyde increases with larger quantities of a photocatalyst in the plasters, however the difference in performance between the 3% and 5% samples is negligible but the difference in cost is relevant.

11.7 Conclusions

- The photocatalytic plaster was prepared by mixing commercial lime based plaster (in dry form) with different quantities of K7000, i.e. TiO_2 nanoparticles which are photocatalytically active under visible light conditions.

- It was found that the physical properties of the plasters were not noticeably affected by the addition of the nanoparticles. Furthermore, mineralogical and EDX analysis results showed few significant changes between the traditional and photocatalytic lime plasters, due to the addition of the anatase TiO_2 nanoparticles.

- In addition, porosimetry studies showed that there were no measurable differences between the samples, except when K7000 nanoparticles were present at 5wt % (ETDK5). When an increase of 65 % in surface area was observed with respect to the blank plaster (ETD).

- The photocatalytic degradation of formaldehyde under visible light was found to be in the range of 9.9 to 11.1% (for all three levels of dosage). ETDK3 was shown to be the best sample in terms of cost versus the ability to photocatalytically degrade formaldehyde.

- It has been demonstrated that photocatalytic lime plasters are a technically viable solution for air quality improvement in indoor environments where visible light predominates. This research demonstrates that photocatalytic particles can be used indoors, incorporated into a low carbon plaster.

- Further research is now in progress to address the scale-up of the preparation of these photocatalytic materials and their application in real life conditions The coatings have been investigated in experimental outdoor buildings (test cells) at the HIVE near Swindon, UK, and at Acciona in Madrid.

12 General discussion

In the previous chapters, analytical and experimental techniques were described and results were presented and analysed. Chapter three explained in detail all the analytical technique used to characterize the samples. Chapter four and five focused on experimental techniques employed to synthesize and prepare various nanoparticles and coatings. Chapter six described the methods used to assess the photocatalytic activity of nanoparticles and coatings. Chapters seven, eight and nine characterized the particles and assessed photocatalytic activity. Chapters ten and eleven characterized and evaluated the photocatalytic activity of coatings designed for lime and MDF based substrates. This chapter brings together the experimental results from chapters seven, eight, nine, ten and eleven and discusses their overall impact.

The sol-gel technique has proved to be an ideal way to produce and modify TiO_2 nanoparticles in accord with the literature [82, 192-195]. Throughout chapters seven and eight various successful doping procedures have been described. All the particles produced, pure or doped, are formed as nanoparticle aggregates with nucleation and aggregation acting as the driving force during their synthesis. All the microscopy techniques including SEM, FESEM, TEM and He-beam microscopy show that the structure of the surface of all samples, pure or doped, consists of nanoparticles of various dimensions and is not greatly influenced by the type and amount of dopant when comparing pure, cobalt doped and tungsten doped samples.

It is noticeable how an increasing amount of tungsten in the lattice increases the anatase phase and decreases the brookite phase in contrast with cobalt that seems to have the opposite effect as confirmed by Rietveld agreement factors in accord with Tobaldi et al. [174]. This could be related to the ionic radius of tungsten being closer to titanium compared to cobalt.

The photocatalytic performance of the synthesised particles was compared with Degussa P25 and K7000 by assessing the degradation of methylene blue under UV light. While cobalt doped and pure sol-gel TiO_2 did not exhibit a high activity active under UV light, the tungsten doped samples demonstrated superior performances with almost 20% more methylene blue degraded when compared to P25.

The photocatalytic performance of the synthesised particles was compared with Degussa P25 by following methylene blue degradation under visible light. Dye degradation rates were lower than under UV irradiation. Cobalt doped sol-gel TiO_2 degraded 15% more than P25 under white light. The same trend was observed in all the tungsten doped materials with better performance than the commercial particles confirming the successful tuning of band gap described by numerous research [89, 196]

NO_x removal was also used as a measure of photocatalytic performances for the nanoparticles. Cobalt-doped and pure TiO_2 were slightly less effective than P25 in reducing NO_x following 50 minutes of irradiation by an Osram solar lamp. All the tungsten-doped samples achieved higher degradation rates when compared with commercial TiO_2. It should be noted that reactions in the gas phase have lower probabilities of collision between molecules than in the aqueous phase due to the fewer number of molecules.

As a result of the positive photocatalytic performance of cobalt and tungsten doped TiO_2 in both liquid and gas phases, they were all selected to be coated onto a medium density fibreboard (MDF) substrate.

12.1 Photocatalytic activity and performance of graphene-TiO_2 nanoparticles

Sol-gel synthesis of graphene-TiO_2 nanoparticles has been proved to be a viable production route for modified TiO_2 particles and is preferable to the preparation protocol described in chapter nine which involves mixing under heat. Graphene acts as a nucleation point and driving force for the synthesis of nanoparticles in the same way that the dopant atoms act for doped nanoparticles described.

Imaging microscopy shows the main difference in surface structure between the two protocols of sol-gel synthesis or thermal mixing. $GTiO_2S$ (sample prepared through sol-gel) comprise nanoparticle aggregates of various dimension but with a small amount of graphene in the samples. $GTiO_2M$ (prepared through mixing under heat) has instead a much more intricate network of TiO_2 nanoparticles (spheres) and graphene sheets.

It is noticeable how the presence of graphene during the sol-gel synthesis decreases the anatase phase and increases the brookite phase, determined by Rietveld agreement factors, following the trend seen with cobalt doping. This is in accord with Raman data that also shows a minor amount of graphene in the sol-gel sample.

The photocatalytic performance of the graphene synthesised nanoparticles was compared with Degussa P25 and pure sol-gel TiO_2 by assessing methylene blue degradation under UV light. While $GTiO_2M$ and pure sol-gel TiO_2 did not exhibit a high activity under UV light, $GTiO_2S$ has a similar performance to P25. The photocatalytic performance under visible light reveals that degradation rates of the dye by the hybrid materials was higher than both sol-gel pure TiO_2 and P25 with $GTiO_2S$ degrading almost 50% of MB in 30 minutes compared with 10% of the MB by P25 supporting previous research on graphene TiO_2 hybrids [106] confirming the ability of graphene coupled with TiO2 to extend charge recombination times. The amount of graphene in the sample was supposed to decrease the PC activity following Zhang et al.[107]

NO_x removal was also used as a photocatalytic performance test for the particles. The performance of both types of graphene/TiO_2 was slightly better than P25 under Osram solar lamp irradiation.[107]

12.2 Assessment of TiO_2 based coatings

TiO_2 hydro/alcoholic based coatings were applied on MUF impregnated paper-coated MDF boards. SEM and EDX showed that the boards already contained TiO_2 (rutile form) to enhance whitening and mechanical properties. SEM and EDX were also used to image the distribution of sol-gel TiO_2 on the surface of the paper coating and proved that doped samples successfully adhered to the MDF board. An estimation of the wet and dry coating thickness was calculated from the density of all the components of the liquid coating.

Ink Intelligent inks were used as a preliminary qualitative method to prove the PC activity of the coatings. All the pure and doped TiO_2 based coatings were shown to be active under both UV and visible light by observing colour changes of the inks on the irradiated surfaces.

A plaster/TiO_2 mixture was applied to the lime based substrates creating a 3mm thick photocatalytic plaster. The presence of K7000 in the plaster did not modify colour but did increase the amount of water required to produce a workable plaster mix. The workability was found to be a function of the increasing amount of TiO_2. BET results were inversely correlated with the average pore size measured by mercury intrusion porosimetry. A

reduction of the pore size was observed in the samples with higher a content of nanoparticles.

A standardized formaldehyde degradation test was employed to measure the photocatalytic activity of the plaster coating when compared with a blank. Formaldehyde degradation under visible light was found to be in the range of 10 to 11% (for all three dosages). Confirming a possible application in an indoor environment using visible light where most of the research examines at the use of UV lights [125-127].

The research presented in this thesis has focused on the production and characterization of TiO_2 based photocatalysts for application to MDF and lime based substrates. These were applied in the form of coatings specifically engineered for pollution remediation in the indoor environment.

For this purpose, the preparation of all the pure, doped and hybrid TiO_2 based samples was described in **Chapter four**. The production and characterization (Raman spectroscopy, XRD, band gap characterization, BET and surface morphology analysis) of photocatalytic particles which were active under visible light was the aim of the first stage of the thesis. Comparison of the prepared materials with commercially available anatase powders demonstrated that:

- Sol-gel is a viable and simple way to produce TiO_2 nanoparticles aggregates which are pure, doped or coupled to another substrate (graphene in this case).
- All the samples produced showed strong aggregation irrespective of the presence (or not) of dopants in the lattice.

In **Chapter five** TiO_2 based coatings were produced for lime and MDF substrates using both commercially available anatase powders and sol-gel produced TiO_2. Water/alcohol based solutions containing 0.5% (w.t.) of TiO_2 were successfully applied to the surface of the MDF producing a thin almost invisible layer.

Photocatalytic plaster containing 2, 3 and 5% of K7000 was prepared and applied to a lime substrate without modifying the aesthetic of the plaster.

Both coatings were fully characterized using optical and electron microscopy, EDX, Raman and XRD (for the lime sample) and then tested for photocatalytic activity. Optical and electron microscopy successfully confirmed the presence and distribution of TiO_2

particles on the surface as well as the microstructure of the substrate itself. Raman and EDX confirmed the presence of a dopant in the nanoparticles and the presence of nanoparticles in the coatings.

The final stage of the thesis assessed the photocatalytic activity of particles and coatings. Four techniques were employed and reported in **Chapter six**. The photocatalytic activity of nanoparticle aggregates was estimated by examining the degradation of methylene blue in the liquid phase and NO_x reduction in the gas phase. Photocatalytic activity of MDF coatings was studied by identifying colour changes in commercially available Ink Intelligent inks. All the prepared samples showed PC activity within five minutes of irradiation. The PC activity of lime coatings was studied by following formaldehyde degradation and 10% of the pollutant was degraded by the coatings containing photocatalyst.

13 Conclusions

- Increasing the alcohol content, and decreasing both mixing rate and temperature during the sol-gel synthesis of TiO_2 using titanium tetraisopropoxide increased the yield of crystalline anatase, however aggregation of the nanoparticles formed was observed.
- The crystalline phase composition of sol-gel TiO_2 was highly dependent on the annealing temperature. Annealing at 550 °C produced a higher proportion of rutile when compared to material annealed at 450 °C.
- Cobalt doped TiO_2 nanoparticles degraded 25% more methylene blue in a solid/liquid system under visible light compared to that of commercially available P25 under identical conditions.
- Photocatalytic degradation of NO_x under visible light at the gas/solid interface highlighted similar behaviour between cobalt doped TiO_2 and commercially available P25 and K7000 photo catalytic particles.
- An increasing concentration of tungsten in the lattice of TiO_2 prepared via a sol-gel route increased the proportion of anatase in the microstructure. Rietveld agreement factors from XRD data and the blue shift of the main Raman band at 145 cm^{-1} indicated a decreasing dimension of the anatase crystalline domains.
- Doping of sol-gel TiO_2 with tungsten successfully improved the photocatalytic activity at the liquid/solid interface. Tungsten doped particles degraded circa 10% more methylene blue compared to commercially available P25 under visible light irradiation.
- Tungsten doped particles exhibited a slightly higher photocatalytic activity compared to commercially available P25 when degrading NO_x in the solid/gas phase under irradiation with visible light.
- Routes employed to produce graphene/TiO_2 hybrid particles involving both in-situ reaction during sol-gel synthesis and mixing after reaction both resulted in similar crystalline structures. However the Graphene/TiO_2 ratio in the nanoparticles formed was observed to vary. The particles produced using the mixing methodology showed a higher proportion of the anatase crystalline phase and larger quantity of residual graphene incorporated into the structure.

- Degradation of methylene blue under visible light confirmed superior performances of both Graphene/TiO_2 hybrids with up to 30% more dye oxidised compared to commercially available P25.
- Degradation of NO_x confirmed a superior performance of the Graphene/TiO_2 hybrids at the gas/solid interface under illumination with visible light when compared with P25
- Pure and doped TiO_2 nanoparticles produced via a sol-gel synthesis route, in addition to commercially available P25 and K7000, were successfully incorporated into the surface coating of Kronospan MDF boards. This was achieved without unacceptably modifying the surface appearence. Degradation of Ink Intelligent dyes applied to the coating surfaces confirmed their photocatalytic properties under both visible and UV light.
- The incorporation of K7000 TiO_2 nanoparticles into the surface of lime based coatings did not modify the appearance at both macroscopic and microscopic scales. Examination of the coatings with both the naked eye, and also using a colorimeter, did not indicate a difference in terms of either the colour or surface gloss.
- The photocatalytic degradation of formaldehyde under visible light was found to be in the range of 9.9 to 11.1% for particle concentrations between 2 and 5%. A TiO_2 concentration of 3% was shown to be the best compromise in terms of cost versus the ability to degrade formaldehyde photocatalytically.
- It has been demonstrated that photocatalytic lime plasters and MDF coatings are a technically viable solution for air quality improvement in the indoor environment where visible light predominates and UV levels are extremely low.

14 Further work

In the present work, the production of sol-gel doped TiO_2 and TiO_2 based coatings to reduce indoor pollution by photocatalytic activation with visible light was evaluated.

Growing awareness of indoor air quality is promoting research to discover solutions which either reduce the release of VOCs and pollutants from indoor building materials or to introduce PC coatings that will reduce the concentration of harmful molecules. Future work could involve looking at how the application of PC on items in the indoor environment influence the emission of harmful molecule by examining the real-life behaviour of coatings under real-life illumination:

Concerns raised over the safety of nanoparticles are leading to the introduction of more safety measures which restrict their use. Thus, the potential application of TiO_2 nanoparticles as photocatalysts is at risk. Future work should look at TiO_2 loss of particles from the coatings by abrasion or chemical reaction from the MDF and lime coatings produced in this work. The study of the effect of the particles loss to the performances of the coatings is mandatory for real life applications.

More accurate protocols and in-depth studies on the formulation and testing of PC coatings are necessary for real-world applications. A more precise study of the durability and long-term performance of the coatings is mandatory as well as a better understand of incorporation of the coatings in real life environment.

W doped TiO_2 particles and graphene/TiO_2 hybrids studied in this work shows good performances under visible light. Future work should be a focus on the incorporation of particles in the substrates previously described. Photocatalytic performance of this coating, as well as the one prepared in this work, should be studied for gas/solid interface reactions.

Bibliography

1. EPA., U.S., *U.S. EPA. Air Quality Criteria for Lead (Final Report, 2006). U.S. Environmental Protection Agency, Washington, DC, EPA/600/R-05/144aF-bF, 2006.* 2006, EPA: U.S. Environmental Protection Agency, Washington, DC, USA.
2. WHO, *WHO guidelines for indoor air quality: selected pollutants*. 2010, WHO Regional Office for Europe WHO Regional Office for Europe Scherfigsvej 8 DK-2100 Copenhagen Ø, Denmark.
3. Crump, D., A. Dengel and M. Swainson, *Indoor air quality in highly energy efficient homes–a review.* United Kingdom: NHBC Foundation, 2009.
4. Jones, A.P., *Indoor air quality and health.* Atmospheric Environment 1999. **33**: p. 4535-4564.
5. Wargocki, P., D.P. Wyon, J.A.N. Sundell, G.E.O. Clausen and P.O. Fanger, *The Effects of Outdoor Air Supply Rate in an Office on Perceived Air Quality, Sick Building Syndrome (SBS) Symptoms and Productivity.* Indoor Air, 2000. **10**(4): p. 222-236.
6. Dengel, A., *The very air we breathe.* RICS PROPERTY Journal, 2014.
7. Mauzerall, D.L., B. Sultan, N. Kim and D.F. Bradford, *NOx emissions from large point sources: variability in ozone production, resulting health damages and economic costs.* Atmospheric Environment, 2005. **39**(16): p. 2851-2866.
8. Alevantis, L.E. and C.D.o.H. Services, *Reducing Occupant Exposure to Volatile Organic Compounds (VOCs) from Office Building Construction Materials: Non-binding Guidelines*. 1996: California Depart. of Health Services.
9. Guo, H., F. Murray and S. Lee, *The development of low volatile organic compound emission house—a case study.* Building and environment, 2003. **38**(12): p. 1413-1422.
10. Son, Y.-S., B.-A. Lim, H.-J. Park and J.-C. Kim, *Characteristics of volatile organic compounds (VOCs) emitted from building materials to improve indoor air quality: focused on natural VOCs.* Air quality, atmosphere & health, 2013. **6**(4): p. 737-746.
11. Ferreira Pinto Da Silva, C., C. Rana, D. Maskell, A. Dengel, P. Ansell and R.J. Ball, *Influence of eco-materials on indoor air quality.* Green Materials, 2016. **4**(2): p. 72-80.

12. Maskell, D., C.F. da Silva, K. Mower, R. Cheta, A. Dengel, R. Ball, M. Ansell, P. Walker and A. Shea, *Properties of bio-based insulation materials and their potential impact on indoor air quality.* 2015.
13. Yao, N. and K.L. Yeung, *Investigation of the performance of TiO 2 photocatalytic coatings.* Chemical engineering journal, 2011. **167**(1): p. 13-21.
14. Kamegawa, T., Y. Shimizu and H. Yamashita, *Superhydrophobic surfaces with photocatalytic self-cleaning properties by nanocomposite coating of TiO(2) and polytetrafluoroethylene.* Adv Mater, 2012. **24**(27): p. 3697-700.
15. Sotelo-Vazquez, C., N. Noor, A. Kafizas, R. Quesada-Cabrera, D.O. Scanlon, A. Taylor, J.R. Durrant and I.P. Parkin, *Multifunctional P-Doped TiO2Films: A New Approach to Self-Cleaning, Transparent Conducting Oxide Materials.* Chemistry of Materials, 2015. **27**(9): p. 3234-3242.
16. Leyland, N.S., J. Podporska-Carroll, J. Browne, S.J. Hinder, B. Quilty and S.C. Pillai, *Highly Efficient F, Cu doped TiO2 anti-bacterial visible light active photocatalytic coatings to combat hospital-acquired infections.* Scientific reports, 2016. **6**.
17. Khanchandani, S., S. Kumar and A.K. Ganguli, *Comparative study of TiO2/CuS core/shell and composite nanostructures for efficient visible light photocatalysis.* ACS Sustainable Chemistry & Engineering, 2016. **4**(3): p. 1487-1499.
18. Charles-Kittel, *Introduction to Solid State Physics 8th Edition*. 2004: Wiley.
19. *Diagram showing the combinations of the atomic orbitals of titanium and oxygen*. Available from: http://www.techwomen.co/wiring/diagrams/ti-orbital-diagrams-for-4.html.
20. Catherine E. Housecroft, A.G.S., *Inorganic Chemistry, 2nd Ed*. 2005: Pearson.
21. W. D. Callister, J., *Materials Science and Engineering*. 2007: John Wiley & Sons, Inc.
22. Murray, J. and H. Wriedt, *The O− Ti (oxygen-titanium) system.* Journal of Phase Equilibria, 1987. **8**(2): p. 148-165.
23. Reyes-Coronado, D., G. Rodriguez-Gattorno, M.E. Espinosa-Pesqueira, C. Cab, R. de Coss and G. Oskam, *Phase-pure TiO_2 nanoparticles: anatase, brookite and rutile.* Nanotechnology, 2008. **19**(14): p. 145605.
24. Banfield, H.Z.J.F., *Thermodynamic analysis of phase stability of nanocrystalline titania.* Journal of Materials Chemistry 1998. **8**: p. 2073-2076.
25. Meinhold, G., *Rutile and its applications in earth sciences.* Earth-Science Reviews, 2010. **102**(1): p. 1-28.

26. Mo, S.-D. and W.Y. Ching, *Electronic and optical properties of three phases of titanium dioxide: Rutile, anatase, and brookite.* Physical Review B, 1995. **51**(19): p. 13023-13032.
27. Colorado, U.o. *Mineral Structure_TiO_2 Group*. Available from: http://ruby.colorado.edu/~smyth/min/tio2.html.
28. *Rutile structure showing the atomic structure* Available from: http://metadise.org/w/Lesson_1.
29. Hanaor, D.A.H. and C.C. Sorrell, *Review of the anatase to rutile phase transformation.* Journal of Materials Science, 2010. **46**(4): p. 855-874.
30. K. Nagaveni, M.S.H., N. Ravishankar, G. N. Subbanna, Giridhar Madras, *Synthesis and Structure of Nanocrystalline TiO2 with Lower Band Gap Showing High Photocatalytic Activity.* Langmuir 2004, 2004. **20**: p. 2900-2907.
31. Yin, W.-J., S. Chen, J.-H. Yang, X.-G. Gong, Y. Yan and S.-H. Wei, *Effective band gap narrowing of anatase TiO[sub 2] by strain along a soft crystal direction.* Applied Physics Letters, 2010. **96**(22): p. 221901.
32. Tanemura, S., L. Miao, P. Jin, K. Kaneko, A. Terai and N. Nabatova-Gabain, *Optical properties of polycrystalline and epitaxial anatase and rutile TiO2 thin films by rf magnetron sputtering.* Applied Surface Science, 2003. **212-213**: p. 654-660.
33. Lin, H., C. Huang, W. Li, C. Ni, S. Shah and Y. Tseng, *Size dependency of nanocrystalline TiO2 on its optical property and photocatalytic reactivity exemplified by 2-chlorophenol.* Applied Catalysis B: Environmental, 2006. **68**(1-2): p. 1-11.
34. A. Fujishima, X. Zhang and D.A. Trykc, *TiO_2 photocatalysis and related surface phenomena.* Surface Science Reports, 2008. **63**(12): p. 515-582.
35. Tompsett, G., G. Bowmaker, R. Cooney, J. Metson, K. Rodgers and J. Seakins, *The Raman spectrum of brookite, TiO2 (PBCA, Z= 8).* Journal of Raman Spectroscopy, 1995. **26**(1): p. 57-62.
36. Landmann, M., E. Rauls and W.G. Schmidt, *The electronic structure and optical response of rutile, anatase and brookite TiO 2.* Journal of Physics: Condensed Matter, 2012. **24**(19): p. 195503.
37. Ohtani, B., J.-i. Handa, S.-i. Nishimoto and T. Kagiya, *Highly active semiconductor photocatalyst: Extra-fine crystallite of brookite TiO2 for redox reaction in aqueous propan-2-ol and / or silver sulfate solution.* Chemical Physics Letters, 1985. **120**(3): p. 292-294.

38. Nakaso, K., K. Okuyama, M. Shimada and S.E. Pratsinis, *Effect of reaction temperature on CVD-made TiO 2 primary particle diameter.* Chemical Engineering Science, 2003. **58**(15): p. 3327-3335.
39. Li, W., S.I. Shah, C.-P. Huang, O. Jung and C. Ni, *Metallorganic chemical vapor deposition and characterization of TiO 2 nanoparticles.* Materials Science and Engineering: B, 2002. **96**(3): p. 247-253.
40. Xie, H., G. Gao, Z. Tian, N. Bing and L. Wang, *Synthesis of TiO 2 nanoparticles by propane/air turbulent flame CVD process.* Particuology, 2009. **7**(3): p. 204-210.
41. Eslava, S., A. Reynal, V.G. Rocha, S. Barg and E. Saiz, *Using graphene oxide as a sacrificial support of polyoxotitanium clusters to replicate its two-dimensionality on pure titania photocatalysts.* Journal of Materials Chemistry A, 2016. **4**(19): p. 7200-7206.
42. Lim, K.T., H.S. Hwang, W. Ryoo and K.P. Johnston, *Synthesis of TiO2 nanoparticles utilizing hydrated reverse micelles in CO2.* Langmuir, 2004. **20**(6): p. 2466-2471.
43. Noh, J., M. Yi, S. Hwang, K.M. Im, T. Yu and J. Kim, *A facile synthesis of rutile-rich titanium oxide nanoparticles using reverse micelle method and their photocatalytic applications.* Journal of Industrial and Engineering Chemistry, 2016. **33**: p. 369-373.
44. Boutonnet, M. and M. Sanchez-Dominguez, *Microemulsion droplets to catalytically active nanoparticles. How the application of colloidal tools in catalysis aims to well designed and efficient catalysts.* Catalysis Today, 2017. **285**: p. 89-103.
45. Tanaka, Y. and M. Suganuma, *Effects of heat treatment on photocatalytic property of sol-gel derived polycrystalline TiO2.* Journal of sol-gel science and technology, 2001. **22**(1-2): p. 83-89.
46. *The Electromagnetic Spectrum.*
47. A. Fujishima, A. Honda and K. Iwata, *Electrochemical Photolysis of Water at a Semiconductor Electrode*. Nature, 1972. **238**.
48. Paz, Y., *Application of TiO_2 photocatalysis for air treatment: Patents' overview.* Applied Catalysis B: Environmental, 2010. **99**(3-4): p. 448-460.
49. Taranto, J., D. Frochot and P. Pichat, *Photocatalytic treatment of air: comparison of various TiO2, coating methods, and supports using methanol or n-octane as*

test pollutant. Industrial & Engineering Chemistry Research, 2009. **48**(13): p. 6229-6236.

50. Lee, S.-A., K.-H. Choo, C.-H. Lee, H.-I. Lee, T. Hyeon, W. Choi and H.-H. Kwon, *Use of ultrafiltration membranes for the separation of TiO2 photocatalysts in drinking water treatment.* Industrial & engineering chemistry research, 2001. **40**(7): p. 1712-1719.
51. Kotani, Y., A. Matsuda, M. Tatsumisago, T. Minami, T. Umezawa and T. Kogure, *Formation of anatase nanocrystals in sol-gel derived TiO2-SiO2 thin films with hot water treatment.* Journal of Sol-Gel Science and Technology, 2000. **19**(1-3): p. 585-588.
52. Choi, H., E. Stathatos and D.D. Dionysiou, *Photocatalytic TiO2 films and membranes for the development of efficient wastewater treatment and reuse systems.* Desalination, 2007. **202**(1): p. 199-206.
53. Y. Paz, Z.L., L. Rabenberg, A. Heller, *Photooxidative self-cleaning transparent titanium dioxide films on glass.* J. Mater. Res, Nov 1995. **Vol. 10**(No. 11).
54. Li, Z., Y. Hou, B. Ma, X. Wu, Z. Xing and K. Li, *Super-hydrophilic porous TiO2-ZnO composite thin films without light irradiation.* Environmental Progress & Sustainable Energy, 2016.
55. Ryo Baba, Seiichiro Nakabayashi, Akira Fujishima and K. Honda, *Investlgatlon of the Mechanlrm of Hydrogen Evolution during Photocatalytic Water Decomposltion on MetaCLoaded Semiconductor Powders.* j. phys. Chem, 1985. **89**: p. 1902-1905.
56. Carp, O., C.L. Huisman and A. Reller, *Photoinduced reactivity of titanium dioxide.* Progress in solid state chemistry, 2004. **32**(1): p. 33-177.
57. Liu, X., G. Dong, S. Li, G. Lu and Y. Bi, *Direct Observation of Charge Separation on Anatase TiO2 Crystals with Selectively Etched {001} Facets.* Journal of the American Chemical Society, 2016. **138**(9): p. 2917-2920.
58. Yoshihara, T., R. Katoh, A. Furube, Y. Tamaki, M. Murai, K. Hara, S. Murata, H. Arakawa and M. Tachiya, *Identification of reactive species in photoexcited nanocrystalline TiO2 films by wide-wavelength-range (400-2500 nm) transient absorption spectroscopy.* The Journal of Physical Chemistry B, 2004. **108**(12): p. 3817-3823.
59. Peiró, A.M., C. Colombo, G. Doyle, J. Nelson, A. Mills and J.R. Durrant, *Photochemical reduction of oxygen adsorbed to nanocrystalline TiO2 films: A*

transient absorption and oxygen scavenging study of different TiO2 preparations. The Journal of Physical Chemistry B, 2006. **110**(46): p. 23255-23263.

60. Tamaki, Y., K. Hara, R. Katoh, M. Tachiya and A. Furube, *Femtosecond Visible-to-IR Spectroscopy of TiO2 Nanocrystalline Films: Elucidation of the Electron Mobility before Deep Trapping†.* The Journal of Physical Chemistry C, 2009. **113**(27): p. 11741-11746.
61. Tamaki, Y., A. Furube, M. Murai, K. Hara, R. Katoh and M. Tachiya, *Dynamics of efficient electron–hole separation in TiO 2 nanoparticles revealed by femtosecond transient absorption spectroscopy under the weak-excitation condition.* Physical Chemistry Chemical Physics, 2007. **9**(12): p. 1453-1460.
62. Daimon, T., T. Hirakawa, M. Kitazawa, J. Suetake and Y. Nosaka, *Formation of singlet molecular oxygen associated with the formation of superoxide radicals in aqueous suspensions of TiO2 photocatalysts.* Applied Catalysis A: General, 2008. **340**(2): p. 169-175.
63. Egerton, T.A. and J.A. Mattinson, *The influence of platinum on UV and 'visible'photocatalysis by rutile and Degussa P25.* Journal of Photochemistry and Photobiology A: Chemistry, 2008. **194**(2): p. 283-289.
64. Heller, A., *Chemistry and applications of photocatalytic oxidation of thin organic films.* Accounts of Chemical Research, 1995. **28**(12): p. 503-508.
65. Hoffmann, M.R., S.T. Martin, W. Choi and D.W. Bahnemann, *Environmental Applications of Semiconductor Photocatalysis.* Chemical Reviews, 1995. **95**(1): p. 69-96.
66. Watanabe, T., A. Nakajima, R. Wang, M. Minabe, S. Koizumi, A. Fujishima and K. Hashimoto, *Photocatalytic activity and photoinduced hydrophilicity of titanium dioxide coated glass.* Thin Solid Films, 1999. **351**(1): p. 260-263.
67. Kazuhito, H., I. Hiroshi and F. Akira, *TiO 2 Photocatalysis: A Historical Overview and Future Prospects.* Japanese Journal of Applied Physics, 2005. **44**(12R): p. 8269.
68. Devahasdin, S., C. Fan, K. Li and D.H. Chen, *TiO2 photocatalytic oxidation of nitric oxide: transient behavior and reaction kinetics.* Journal of Photochemistry and Photobiology A: Chemistry, 2003. **156**(1): p. 161-170.
69. Yu, Y.-H., Y.-T. Pan, Y.-T. Wu, J. Lasek and J.C.S. Wu, *Photocatalytic NO reduction with C3H8 using a monolith photoreactor.* Catalysis Today, 2011. **174**(1): p. 141-147.

70. Zhaoliang, Z., M. Jun and Y. Xiyao, *Separate/simultaneous catalytic reduction of sulfur dioxide and/or nitric oxide by carbon monoxide over TiO2-promoted cobalt sulfides.* Journal of Molecular Catalysis A: Chemical, 2003. **195**(1): p. 189-200.
71. Zhaoliang, Z., M. Jun and Y. Xiyao, *Separate/simultaneous catalytic reduction of sulfur dioxide and/or nitric oxide by carbon monoxide over titanium–tin solid solution catalysts.* Chemical Engineering Journal, 2003. **95**(1): p. 15-24.
72. Inoue, H., T. Matsuyama, B.-J. Liu, T. Sakata, H. Mori and H. Yoneyama, *Photocatalytic activities for carbon dioxide reduction of TiO2 microcrystals prepared in SiO2 matrices using a sol–gel method.* Chemistry letters, 1994. **23**(3): p. 653-656.
73. Yamashita, H., H. Nishiguchi, N. Kamada, M. Anpo, Y. Teraoka, H. Hatano, S. Ehara, K. Kikui, L. Palmisano, A. Sclafani, M. Schiavello and M.A. Fox, *Photocatalytic reduction of CO2 with H2O on TiO2 and Cu/TiO2 catalysts.* Research on Chemical Intermediates, 1994. **20**(8): p. 815-823.
74. Srinivas, B., B. Shubhamangala, K. Lalitha, P. Anil Kumar Reddy, V. Durga Kumari, M. Subrahmanyam and B.R. De, *Photocatalytic Reduction of CO2 over Cu-TiO2/Molecular Sieve 5A Composite.* Photochemistry and photobiology, 2011. **87**(5): p. 995-1001.
75. Halmann, M., V. Katzir, E. Borgarello and J. Kiwi, *Photoassisted carbon dioxide reduction on aqueous suspensions of titanium dioxide.* Solar Energy Materials, 1984. **10**(1): p. 85-91.
76. Anpo, M., H. Yamashita, Y. Ichihashi and S. Ehara, *Photocatalytic reduction of CO2 with H2O on various titanium oxide catalysts.* Journal of Electroanalytical Chemistry, 1995. **396**(1-2): p. 21-26.
77. Anpo, M., H. Yamashita, K. Ikeue, Y. Fujii, S.G. Zhang, Y. Ichihashi, D.R. Park, Y. Suzuki, K. Koyano and T. Tatsumi, *Photocatalytic reduction of CO 2 with H 2 O on Ti-MCM-41 and Ti-MCM-48 mesoporous zeolite catalysts.* Catalysis Today, 1998. **44**(1): p. 327-332.
78. 206, T.C.I.T., *Fine ceramics (advanced ceramics, advanced technical ceramics) -- Determination of photocatalytic activity of surfaces in an aqueous medium by degradation of methylene blue (2010).* 2010.
79. Dunlea, E.J., S.C. Herndon, D.D. Nelson, R.M. Volkamer, F. San Martini, P.M. Sheehy, M.S. Zahniser, J.H. Shorter, J.C. Wormhoudt, B.K. Lamb, E.J. Allwine, J.S. Gaffney, N.A. Marley, M. Grutter, C. Marquez, S. Blanco, B. Cardenas, A. Retama, C.R. Ramos Villegas, C.E. Kolb, L.T. Molina and M.J. Molina,

Evaluation of nitrogen dioxide chemiluminescence monitors in a polluted urban environment. Atmos. Chem. Phys., 2007. **7**(10): p. 2691-2704.

80. Mills, A., C. Hill and P.K.J. Robertson, *Overview of the current ISO tests for photocatalytic materials.* Journal of Photochemistry and Photobiology A: Chemistry, 2012. **237**: p. 7-23.
81. Gole, J.L., J.D. Stout, C. Burda, Y. Lou and X. Chen, *Highly Efficient Formation of Visible Light Tunable TiO2-xNx Photocatalysts and Their Transformation at the Nanoscale.* The Journal of Physical Chemistry B, 2004. **108**(4): p. 1230-1240.
82. Giampiccolo, A., M.P. Ansell, D. M.Tobaldi and R.J. Ball, *Synthesis of Co–TiO2 nanostructured photocatalytic coatings for MDF substrates.* Green Materials, 2016. **4**(4): p. 140-149.
83. Long, R. and N.J. English, *First-principles calculation of nitrogen-tungsten codoping effects on the band structure of anatase-titania.* Applied physics letters, 2009. **94**(13): p. 132102.
84. Zhang, L., X. Li, Z. Chang and D. Li, *Preparation, characterization and photoactivity of hollow N, Co co-doped TiO 2/SiO 2 microspheres.* Materials Science in Semiconductor Processing, 2011. **14**(1): p. 52-57.
85. Navío, J.A., G. Colón, M.a. Trillas, J. Peral, X. Domènech, J.J. Testa, J. Padrón, D. Rodríguez and M.I. Litter, *Heterogeneous photocatalytic reactions of nitrite oxidation and Cr(VI) reduction on iron-doped titania prepared by the wet impregnation method.* Applied Catalysis B: Environmental, 1998. **16**(2): p. 187-196.
86. Borlaf, M., M.T. Colomer, F. Cabello, R. Serna and R. Moreno, *Electrophoretic Deposition of TiO2/Er3+ Nanoparticulate Sols.* The Journal of Physical Chemistry B, 2013. **117**(6): p. 1556-1562.
87. Diesen, V., C.W. Dunnill, E. Osterberg, I.P. Parkin and M. Jonsson, *Silver enhanced TiO2 thin films: photocatalytic characterization using aqueous solutions of tris(hydroxymethyl)aminomethane.* Dalton Transactions, 2014. **43**(1): p. 344-351.
88. Bloh, J.Z., A. Folli and D.E. Macphee, *Adjusting Nitrogen Doping Level in Titanium Dioxide by Codoping with Tungsten: Properties and Band Structure of the Resulting Materials.* The Journal of Physical Chemistry C, 2014. **118**(36): p. 21281-21292.

89. Long, R. and N.J. English, *New insights into the band-gap narrowing of (N, P)-codoped TiO_2 from hybrid density functional theory calculations.* Chemphyschem, 2011. **12**(14): p. 2604-8.
90. Mohapatra, S.K., K.S. Raja, V.K. Mahajan and M. Misra, *Efficient Photoelectrolysis of Water using TiO2 Nanotube Arrays by Minimizing Recombination Losses with Organic Additives.* The Journal of Physical Chemistry C, 2008. **112**(29): p. 11007-11012.
91. Zhong, J., F. Chen and J. Zhang, *Carbon-Deposited TiO2: Synthesis, Characterization, and Visible Photocatalytic Performance.* The Journal of Physical Chemistry C, 2010. **114**(2): p. 933-939.
92. Pei, J., W. Ma, R. Li, Y. Li and H. Du, *Preparation and Photocatalytic Properties of TiO2-Al2O3 Composite Loaded Catalysts.* Journal of Chemistry, 2015. **2015**: p. 7.
93. Soylu, A.M., M. Polat, D.A. Erdogan, Z. Say, C. Yıldırım, Ö. Birer and E. Ozensoy, *TiO2–Al2O3 binary mixed oxide surfaces for photocatalytic NOx abatement.* Applied Surface Science, 2014. **318**: p. 142-149.
94. Ahmed, M.A. and M.F. Abdel-Messih, *Structural and nano-composite features of TiO2–Al2O3 powders prepared by sol–gel method.* Journal of Alloys and Compounds, 2011. **509**(5): p. 2154-2159.
95. Arun Kumar, D., J. Merline Shyla and F.P. Xavier, *Synthesis and characterization of TiO2/SiO2 nano composites for solar cell applications.* Applied Nanoscience, 2012. **2**(4): p. 429-436.
96. Anderson, C. and A.J. Bard, *An Improved Photocatalyst of TiO2/SiO2 Prepared by a Sol-Gel Synthesis.* The Journal of Physical Chemistry, 1995. **99**(24): p. 9882-9885.
97. Kwon, C.H., J.H. Kim, I.S. Jung, H. Shin and K.H. Yoon, *Preparation and characterization of TiO2–SiO2 nano-composite thin films.* Ceramics International, 2003. **29**(8): p. 851-856.
98. Kamegawa, T., R. Kido, D. Yamahana and H. Yamashita, *Design of TiO_2-zeolite composites with enhanced photocatalytic performances under irradiation of UV and visible light.* Microporous and Mesoporous Materials, 2013. **165**: p. 142-147.
99. Castañeda-Contreras, J., V.F. Marañón-Ruiz, R. Chiu-Zárate, H. Pérez-Ladrón de Guevara, R. Rodriguez and C. Michel-Uribe, *Photocatalytic activity of erbium-doped TiO_2 nanoparticles immobilized in macro-porous silica films.* Materials Research Bulletin, 2012. **47**(2): p. 290-295.

100. Anpo, M., H. Yamashita, Y. Ichihashi, Y. Fujii and M. Honda, *Photocatalytic Reduction of CO_2 with H_2O on Titanium Oxides Anchored within Micropores of Zeolites: Effects of the Structure of the Active Sites and the Addition of Pt.* J. Phys. Chem. B, 1997. **101**: p. 2632-2636.
101. Jansson, I., S. Suárez, F.J. Garcia-Garcia and B. Sánchez, *Zeolite–TiO_2 hybrid composites for pollutant degradation in gas phase.* Applied Catalysis B: Environmental, 2014.
102. Y. Xu, Y. Zhuang and X. Fu, *New Insight for Enhanced Photocatalytic Activity of TiO2 by Doping Carbon Nanotubes A Case Study on Degradation of Benzene and Methyl Orange.* J. Phys. Chem. C, 2010. **114**: p. 2669–2676
103. Y. YAO, G. LI, S. CISTON, R. M. LUEPTOW and K.A. GRAY, *Photoreactive TiO2_Carbon Nanotube Composites Synthesis and Reactivity.* Environ. Sci. Technol., 2008. **42**: p. 4952-4957.
104. <*Hierarchically Ordered Macro.pdf*>.
105. Liu, J., H. Bai, Y. Wang, Z. Liu, X. Zhang and D.D. Sun, *Self-Assembling TiO2 Nanorods on Large Graphene Oxide Sheets at a Two-Phase Interface and Their Anti-Recombination in Photocatalytic Applications.* Advanced Functional Materials, 2010. **20**(23): p. 4175-4181.
106. Liang, Y., H. Wang, H. Sanchez Casalongue, Z. Chen and H. Dai, *TiO2 nanocrystals grown on graphene as advanced photocatalytic hybrid materials.* Nano Research, 2010. **3**(10): p. 701-705.
107. Y. Zhang, Z. Tang, X. Fu and Y. Xu, *TiO2□Graphene Nanocomposites for Gas-Phase Photocatalytic Degradation of Volatile Aromatic Pollutant: Is TiO2□Graphene Truly Different from Other TiO2□Carbon Composite Materials.* ACSNano. **4**(12): p. 7303-7314.
108. Tersoff, J., *Theory of semiconductor heterojunctions: The role of quantum dipoles.* Physical Review B, 1984. **30**(8): p. 4874-4877.
109. Tersoff, J., *Band lineups at II-VI heterojunctions: failure of the common-anion rule.* Physical review letters, 1986. **56**(25): p. 2755.
110. Ramakrishnan, V., H. Kim, J. Park and B. Yang, *Cobalt oxide nanoparticles on TiO 2 nanorod/FTO as a photoanode with enhanced visible light sensitization.* RSC Advances, 2016. **6**(12): p. 9789-9795.

111. *Tungsten trioxide/titanium dioxide nano heterojunction thin film and preparation and application thereof*. 2016, Google Patents.
112. Tryba, B., P. Homa, R.J. Wróbel and A.W. Morawski, *Photocatalytic decomposition of benzo-[a]-pyrene on the surface of acrylic, latex and mineral paints. Influence of paint composition.* Journal of Photochemistry and Photobiology A: Chemistry, 2014. **286**: p. 10-15.
113. Maggos, T., J. Bartzis, M. Liakou and C. Gobin, *Photocatalytic degradation of NO x gases using TiO 2-containing paint: a real scale study.* Journal of hazardous materials, 2007. **146**(3): p. 668-673.
114. Geng, Q., X. Wang and S.-F. Tang, *Heterogeneous Photocatalytic Degradation Kinetic of Gaseous Ammonia Over Nano-Tio~ 2 Supported on Latex Paint Film.* Biomedical and Environmental Sciences, 2008. **21**(2): p. 118.
115. Hochmannova, L. and J. Vytrasova, *Photocatalytic and antimicrobial effects of interior paints.* Progress in organic coatings, 2010. **67**(1): p. 1-5.
116. Chen, J. and C.-s. Poon, *Photocatalytic construction and building materials: From fundamentals to applications.* Building and Environment, 2009. **44**(9): p. 1899-1906.
117. Cannavale, A., F. Fiorito, M. Manca, G. Tortorici, R. Cingolani and G. Gigli, *Multifunctional bioinspired sol-gel coatings for architectural glasses.* Building and Environment, 2010. **45**(5): p. 1233-1243.
118. Yu, J., X. Zhao, J. Du and W. Chen, *Preparation, microstructure and photocatalytic activity of the porous TiO2 anatase coating by sol-gel processing.* Journal of sol-gel Science and Technology, 2000. **17**(2): p. 163-171.
119. Hench, L.L. and J.K. West, *The sol-gel process.* Chemical reviews, 1990. **90**(1): p. 33-72.
120. Rausch, N. and E. Burte, *Thin TiO2 films prepared by low pressure chemical vapor deposition.* Journal of The Electrochemical Society, 1993. **140**(1): p. 145-149.
121. Lee, H., M.Y. Song, J. Jurng and Y.-K. Park, *The synthesis and coating process of TiO 2 nanoparticles using CVD process.* Powder technology, 2011. **214**(1): p. 64-68.
122. Piszczek, P., Ż. Muchewicz, A. Radtke, M. Gryglas, H. Dahm and H. Różycki, *CVD of TiO 2 and TiO 2/Ag antimicrobial layers: Deposition from the hexanuclear μ-oxo Ti (IV) complex as a precursor, and the characterization.* Surface and Coatings Technology, 2013. **222**: p. 38-43.

123. Maggos, T., A. Plassais, J.G. Bartzis, C. Vasilakos, N. Moussiopoulos and L. Bonafous, *Photocatalytic degradation of NOx in a pilot street canyon configuration using TiO2-mortar panels.* Environmental Monitoring and Assessment, 2008. **136**(1): p. 35-44.

124. Diamanti, M.V., M. Ormellese and M. Pedeferri, *Characterization of photocatalytic and superhydrophilic properties of mortars containing titanium dioxide.* Cement and Concrete Research, 2008. **38**(11): p. 1349-1353.

125. Park, S.M., L. Chekli, J.B. Kim, M. Shahid, H.K. Shon, P.S. Kim, W.-S. Lee, W.E. Lee and J.-H. Kim, *NOx removal of mortar mixed with titania produced from Ti-salt flocculated sludge.* Journal of Industrial and Engineering Chemistry, 2014. **20**(5): p. 3851-3856.

126. Vieira, J., L. Senff, H. Gonçalves, L. Silva, V.M. Ferreira and J.A. Labrincha, *Functionalization of mortars for controlling the indoor ambient of buildings.* Energy and Buildings, 2014. **70**: p. 224-236.

127. Lucas, S.S., V.M. Ferreira and J.L.B. de Aguiar, *Incorporation of titanium dioxide nanoparticles in mortars — Influence of microstructure in the hardened state properties and photocatalytic activity.* Cement and Concrete Research, 2013. **43**: p. 112-120.

128. Vulic, T., M. Hadnadjev-Kostic, O. Rudic, M. Radeka, R. Marinkovic-Neducin and J. Ranogajec, *Improvement of cement-based mortars by application of photocatalytic active Ti–Zn–Al nanocomposites.* Cement and Concrete Composites, 2013. **36**: p. 121-127.

129. Hashimoto, K., H. Irie and A. Fujishima, *TiO2 photocatalysis: a historical overview and future prospects.* Japanese journal of applied physics, 2005. **44**(12R): p. 8269.

130. Shifu, C., Z. Sujuan, L. Wei and Z. Wei, *Preparation and activity evaluation of p–n junction photocatalyst NiO/TiO 2.* Journal of Hazardous Materials, 2008. **155**(1): p. 320-326.

131. Hüsken, G., M. Hunger and H. Brouwers, *Experimental study of photocatalytic concrete products for air purification.* Building and environment, 2009. **44**(12): p. 2463-2474.

132. Ballari, M.M., M. Hunger, G. Hüsken and H. Brouwers, *NO x photocatalytic degradation employing concrete pavement containing titanium dioxide.* Applied Catalysis B: Environmental, 2010. **95**(3): p. 245-254.

133. Ameen, M.M. and G.B. Raupp, *Reversible catalyst deactivation in the photocatalytic oxidation of diluteo-xylene in air*. Journal of Catalysis, 1999. **184**(1): p. 112-122.
134. G. Han , K.U., M. Zhang, T. Honda, S. Kawai, *Development of high-performance UF-bonded reed and wheat straw medium-density fiberboard.* J Wood Sci, 2001. **47**(5): p. 350-355.
135. Woodson, G.E., *Effects of bark, density profile, and resin content on medium-density fiberboards from southern hardwoods.* Forest Products Journal, 1976. **26**(2): p. 39-42.
136. X. P. Ye, J. Julson, M. Kuo, A. Womac and D. Myers, *Properties of medium density fiberboards made from renewable biomass.* Bioresour Technol, 2007. **98**(5): p. 1077-84.
137. M. G. D. Baumann, L.F.L., S. A. Batterman, G. Zhang, *Aldehyde emissions from particleboard and medium density fiberboard products.* Forest Products Journal 2000. **50**(9): p. 75-82.
138. Ansell, M.P., *Multi-functional nano-materials for timber in construction.* Proceedings of the Institution of Civil Engineers-Construction Materials, 2013. **166**(4): p. 248-256.
139. Suryanarayana, C. and M.G. Norton, *X-ray diffraction: a practical approach*. 2013: Springer Science & Business Media.
140. Murphy, B.E., *The physico-chemical properties of fullerenes and porphyrin derivatives deposited on conducting surfaces*. 2014, Trinity College Dublin.
141. Langford, J.I. and A. Wilson, *Scherrer after sixty years: a survey and some new results in the determination of crystallite size.* Journal of Applied Crystallography, 1978. **11**(2): p. 102-113.
142. Burton, A.W., K. Ong, T. Rea and I.Y. Chan, *On the estimation of average crystallite size of zeolites from the Scherrer equation: a critical evaluation of its application to zeolites with one-dimensional pore systems.* Microporous and Mesoporous Materials, 2009. **117**(1): p. 75-90.
143. Larson, A.C. and R.B. Von Dreele, *Gsas*. General Structure Analysis System. LANSCE, MS-H805, Los Alamos, New Mexico, 1994.
144. Toby, B.H., *EXPGUI, a graphical user interface for GSAS.* J. Appl. Crystallogr. , 2001. **34**: p. 210–213.
145. M. Leoni, T.C., P. Scardi, *PM2K: a flexible program implementing Whole Powder Pattern Modelling.* Z. Kristallogr. Suppl., 2006. **23**: p. 249-254.

146. E. J. Mittemeijer, P.S., *Diffraction Analysis of the Microstructure of Materials*. Vol. 2004th edn. 2004: Springer.
147. Egerton, R.F., *Physical principles of electron microscopy: an introduction to TEM, SEM, and AEM*. 2016: Springer.
148. *Scanning Electron Microscopy (SEM/EDS)*. Available from: https://sites.ualberta.ca/~ccwj/teaching/microscopy/.
149. McCreery, R.L., *Raman spectroscopy for chemical analysis*. Vol. 225. 2005: John Wiley & Sons.
150. Standardization, I.O.f., *Determination of the specific surface area of solids by gas adsorption -- BET method*. 2016.
151. Giesche, H., *Mercury porosimetry: a general (practical) overview*. Particle & particle systems characterization, 2006. **23**(1): p. 9-19.
152. Giampiccolo, A., M.P. Ansell, D.M. Tobaldi and R.J. Ball, *Synthesis of Co–TiO2 nanostructured photocatalytic coatings for MDF substrates.* Green Materials, 2016. **4**(4): p. 140-149.
153. Tobaldi, D.M., A. Sever Škapin, R.C. Pullar, M.P. Seabra and J.A. Labrincha, *Titanium dioxide modified with transition metals and rare earth elements: Phase composition, optical properties, and photocatalytic activity.* Ceramics International, 2013. **39**(3): p. 2619-2629.
154. A. Sclafani and J.M. Herrmann, *Comparison of the Photoelectronic and Photocatalytic Activities of Various Anatase and Rutile Forms of Titania in Pure Liquid Organic Phases and in Aqueous Solutions.* J. Phys. Chem., 1996. **100,**(32): p. 13655-13661.
155. Regonini, D., A. Jaroenworaluck, R. Stevens and C.R. Bowen, *Effect of heat treatment on the properties and structure of TiO_2 nanotubes: phase composition and chemical composition.* Surface and Interface Analysis, 2010. **42**(3): p. 139-144.
156. Tobaldi, D.M., R.C. Pullar, M. Leoni, M.P. Seabra and J.A. Labrincha, *Nanosized titania modified with tungsten and silver: Microstructural characterisation of a multifunctional material.* Applied Surface Science, 2013. **287**: p. 276-281.
157. BCB, *Tradical® Décor Enduit mince chaux aérienne pour dressement et finition intérieurs, 80 teintes*. 2014.
158. Tobaldi, D.M., M.P. Seabra, G. Otero-Irurueta, Y.R. de Miguel, R.J. Ball, M.K. Singh, R.C. Pullar and J.A. Labrincha, *Quantitative XRD characterisation and gas-phase photocatalytic activity testing for visible-light (indoor applications) of*

KRONOClean 7000[registered sign]. RSC Advances, 2015. **5**(124): p. 102911-102918.

159. BSI, *Methods of testing cement. Determination of strength*. 2016, BSI.

160. Gaya, U.I. and A.H. Abdullah, *Heterogeneous photocatalytic degradation of organic contaminants over titanium dioxide: A review of fundamentals, progress and problems.* Journal of Photochemistry and Photobiology C: Photochemistry Reviews, 2008. **9**(1): p. 1-12.

161. Toma, F.L., G. Bertrand, D. Klein and C. Coddet, *Photocatalytic removal of nitrogen oxides via titanium dioxide.* Environmental Chemistry Letters, 2004. **2**(3): p. 117-121.

162. A. Mills, J. Hepburn, D. Hazafy, C. O'Rourke, J. Krysa, M. Baudys, M. Zlamal, H. Bartkova, C. E. Hill, K. R. Winn, M. E. Simonsen, E. G. Søgaard, S. C. Pillai, N. S. Leyland, R. Fagan, F. Neumann, C. Lampe and T. Graumann, *A simple, inexpensive method for the rapid testing of the photocatalytic activity of self-cleaning surfaces.* Journal of Photochemistry and Photobiology A: Chemistry, 2013. **272**: p. 18-20.

163. A. Mills and M. McGrady, *A study of new photocatalyst indicator inks.* Journal of Photochemistry and Photobiology A: Chemistry, 2008. **193**(2-3): p. 228-236.

164. Standardization, I.O.f., *Fine ceramics (advanced ceramics, advanced technical ceramics) -- Test method for air-purification performance of semiconducting photocatalytic materials by test chamber method under indoor lighting environment -- Part 1: Removal of formaldehyde*. 2014.

165. Kheamrutai Thamaphat, Pichet Limsuwan and B. Ngotawornchai, *Phase Characterization of TiO_2 Powder by XRD and TEM.* Kasetsart J.(Nat. Sci.), 2008. **42**: p. 357-361.

166. Hu, Y., H.L. Tsai and C.L. Huang, *Effect of brookite phase on the anatase–rutile transition in titania nanoparticles.* Journal of the European Ceramic Society, 2003. **23**(5): p. 691-696.

167. Choi, H.C., Y.M. Jung and S.B. Kim, *Size effects in the Raman spectra of TiO_2 nanoparticles.* Vibrational Spectroscopy, 2005. **37**(1): p. 33-38.

168. Fang, D., K.L. Huang, S.Q. Liu and J.H. Huang, *Fabrication and photoluminiscent properties of titanium oxide nanotube arrays.* Journal of the Brazilian Chemical Society, 2008. **19**(6): p. 1059-1064.

169. Danick Gallant, Michel Pézolet and S. Simard, *Optical and Physical Properties of Cobalt Oxide Films Electrogenerated in Bicarbonate Aqueous Media.* J. Phys. Chem. B, 2006. **110**: p. 6817-6880.

170. Chinedu, E.E. and B. Diola, *Ab-initio Electronic and Structural Properties of Rutile Titanium Dioxide.* Japanese Journal of Applied Physics, 2011. **50**(10R): p. 101103.

171. López, R. and R. Gómez, *Band-gap energy estimation from diffuse reflectance measurements on sol–gel and commercial TiO_2: a comparative study.* Journal of Sol-Gel Science and Technology, 2011. **61**(1): p. 1-7.

172. Zouzelka, R. and J. Rathousky, *Photocatalytic abatement of NOx pollutants in the air using commercial functional coating with porous morphology.* Applied Catalysis B: Environmental, 2017. **217**: p. 466-476.

173. Tobaldi, D., L. Graziani, M. Seabra, L. Hennetier, P. Ferreira, E. Quagliarini and J. Labrincha, *Functionalised exposed building materials: Self-cleaning, photocatalytic and biofouling abilities.* Ceramics International, 2017. **43**(13): p. 10316-10325.

174. Tobaldi, D.M., R.C. Pullar, A.F. Gualtieri, M.P. Seabra and J.A. Labrincha, *Phase composition, crystal structure and microstructure of silver and tungsten doped TiO_2 nanopowders with tuneable photochromic behaviour.* Acta Materialia, 2013. **61**(15): p. 5571-5585.

175. Shannon, R.t., *Revised effective ionic radii and systematic studies of interatomic distances in halides and chalcogenides.* Acta crystallographica section A: crystal physics, diffraction, theoretical and general crystallography, 1976. **32**(5): p. 751-767.

176. Balaji, S., Y. Djaoued and J. Robichaud, *Phonon confinement studies in nanocrystalline anatase-TiO2 thin films by micro Raman spectroscopy.* Journal of Raman spectroscopy, 2006. **37**(12): p. 1416-1422.

177. López, R. and R. Gómez, *Band-gap energy estimation from diffuse reflectance measurements on sol–gel and commercial TiO 2: a comparative study.* Journal of sol-gel science and technology, 2012. **61**(1): p. 1-7.

178. Pottier, A., C. Chaneac, E. Tronc, L. Mazerolles and J.-P. Jolivet, *Synthesis of brookite TiO nanoparticles by thermolysis of TiCl in strongly acidic aqueous media.* Journal of Materials Chemistry, 2001. **11**(4): p. 1116-1121.

179. Dimiev, A.M., L.B. Alemany and J.M. Tour, *Graphene Oxide. Origin of Acidity, Its Instability in Water, and a New Dynamic Structural Model.* ACS Nano, 2013. **7**(1): p. 576-588.
180. Tobaldi, D.M., R.C. Pullar, M.P. Seabra and J.A. Labrincha, *Fully Quantitative X-ray Characterisation of Evonik Aeroxide TiO2 P25.* Materials Letters, 2014. **122**: p. 345-347.
181. A.S. Marfunin, *Physics of Minerals and Inorganic Materials. An Introduction,*, ed. B. Springer-Verlag. 1979.
182. Luttrell, T., S. Halpegamage, J. Tao, A. Kramer, E. Sutter and M. Batzill, *Why is anatase a better photocatalyst than rutile? - Model studies on epitaxial TiO2 films.* Scientific Reports, 2014. **4**: p. 4043.
183. Uddin, M.T., Y. Nicolas, C. Olivier, T. Toupance, M.M. Müller, H.-J. Kleebe, K. Rachut, J. Ziegler, A. Klein and W. Jaegermann, *Preparation of RuO2/TiO2 Mesoporous Heterostructures and Rationalization of Their Enhanced Photocatalytic Properties by Band Alignment Investigations.* The Journal of Physical Chemistry C, 2013. **117**(42): p. 22098-22110.
184. Tobaldi, D.M., R.C. Pullar, L. Duraes, T. Matias, M.P. Seabra and J.A. Labrincha, *Truncated tetragonal bipyramidal anatase nanocrystals formed without use of capping agents from the supercritical drying of a TiO2 sol.* CrystEngComm, 2016. **18**(1): p. 164-176.
185. Serpone, N., D. Lawless and R. Khairutdinov, *Size Effects on the Photophysical Properties of Colloidal Anatase TiO2 Particles: Size Quantization versus Direct Transitions in This Indirect Semiconductor?* The Journal of Physical Chemistry, 1995. **99**(45): p. 16646-16654.
186. Park, Y., W. Kim, H. Park, T. Tachikawa, T. Majima and W. Choi, *Carbon-doped TiO2 photocatalyst synthesized without using an external carbon precursor and the visible light activity.* Applied Catalysis B: Environmental, 2009. **91**(1–2): p. 355-361.
187. Gaurav Sharma, R.B., *Digital Color Imaging Handbook*. Electrical Engineering & Applied Signal Processing Series, ed. G. Sharma. Vol. 1. 2002: CRC PRESS. 816.
188. Gaurav Sharma, R.B., *Digital Color Imaging Handbook*. Electrical Engineering & Applied Signal Processing Series, ed. G. Sharma. Vol. 1. 2002: CRC PRESS. 816.

189. Despotou, E., A. Shtiza, T. Schlegel and F. Verhelst, *Literature study on the rate and mechanism of carbonation of lime in mortars/Literaturstudie über Mechanismus und Grad der Karbonatisierung von Kalkhydrat im Mörtel.* Mauerwerk, 2016. **20**(2): p. 124-137.
190. Rouquerol, J., F. Rouquerol, P. Llewellyn, G. Maurin and K. Sin, *Adsorption by Powders and Porous Solids 2nd Edition Principles, Methodology and Applications*. Vol. 1. 2013: Elsevier. 646.
191. Silva, C.F.F.P.D., *Interactions between volatile organic compounds and natural building materials*, in *Architecture and Civil engineering* 2017, University of Bath.
192. Behnajady, M.A., H. Eskandarloo, N. Modirshahla and M. Shokri, *Investigation of the effect of sol–gel synthesis variables on structural and photocatalytic properties of TiO_2 nanoparticles.* Desalination, 2011. **278**(1-3): p. 10-17.
193. A. Giampiccolo, R. J. Ball and M.P. Ansell. *Synthesis of Co-doped TiO_2 nanostructures for novel photo-catalytic coatings*. in *Energy forum on Advanced Building skins*. 2014. Bressanone, Italy.
194. Tobaldi, D.M., M. Hortigüela Gallo, G. Otero-Irurueta, M.K. Singh, R.C. Pullar, M.P. Seabra and J.A. Labrincha, *Purely Visible-Light-Induced Photochromism in Ag–TiO2 Nanoheterostructures.* Langmuir, 2017. **33**(20): p. 4890-4902.
195. Tobaldi, D.M., C. Piccirillo, R.C. Pullar, A.F. Gualtieri, M.P. Seabra, P.M.L. Castro and J.A. Labrincha, *Silver-Modified Nano-titania as an Antibacterial Agent and Photocatalyst.* The Journal of Physical Chemistry C, 2014. **118**(9): p. 4751-4766.
196. Giampiccolo, A., M.P. Ansell, D.M. Tobaldi and R.J. Ball, *Synthesis of Co-TiO2 Nanostructured Photo-Catalytic Coatings for MDF Substrates.* Green Materials, 2016. **4**(4): p. 1-31.